ABSTRACT

Title of Dissertation:	Defect Engineering of Supported Metal Catalysts for Selective Hydrogenation
	Yuan Zhang, Doctor of Philosophy, 2022
Dissertation directed by:	Professor, Dongxia Liu, chemical and biomolecular engineering

Supported metal catalysts have been used extensively in industry. To construct supported metal catalysts with low cost and high catalytic performance, high metal dispersion on the support material is greatly favored in recent years. With the downsizing of metal active phase, new challenges in catalyst synthesis and characterization have emerged. The highly dispersed metal active phase is prone to aggregate to decrease surface free energy, which requires innovative synthesis strategy to stabilize the metal species on support. High metal dispersion also created more interfacial sites and bonds between metal and support, therefore the metal-support interaction has more significant effects on the catalytic properties of high dispersion catalysts. Defect engineering has attracted much attention due to its ability to help stabilizing metal species and tune the metal-support interaction.

This dissertation focuses on utilizing defect engineering to develop catalysts with high activity and selectivity in hydrogenation reaction. Harsh pH condition was applied in wetness impregnation process to generate cavity sites on TiO_2 support surface, which resulted in stronger metal-support interaction between Pt and TiO_2. The catalyst synthesized under harsh condition showed higher hydrogenation activity towards -NO_2 group. Laser engraving was used as another defect engineering technique to create defects on TiO_2 support. The laser engraved support showed distinct electronic and redox properties, which enhanced the electronic metal-support interaction of Pt and TiO_2 support. The Pt/TiO_2-LE catalyst showed superior activity and selectivity in the hydrogenation of 3-nitrostyrene and furfural alcohol. In addition, an effective method to probe the metal dispersion of Pt by styrene hydrogenation reaction kinetics was developed. This method has the potential to be applied to other catalysts systems and could be used to study the metal-support interaction in catalysts.

DEFECT ENGINEERING OF SUPPORTED METAL CATALYSTS FOR SELECTIVE HYDROGENATION

by

Yuan Zhang

Dissertation submitted to the Faculty of the Graduate School of the
University of Maryland, College Park, in partial fulfillment
of the requirements for the degree of
Doctor of Philosophy
2022

Advisory Committee:
Professor Dongxia Liu, Chair
Professor Yifei Mo, Dean's representative
Professor Andrei Vedernikov
Professor Chunsheng Wang
Dr. Dat T. Tran
Professor Jeffery Davis
Professor Yuhuang Wang

Acknowledgements

I would like to deeply thank my advisor Prof. Dongxia Liu for her patient guidance and support throughout my PhD. study. Prof. Liu's systematic problem solving approach and passion in research helped me keep advancing forward in my research project, which could not have been achieved without her advice. Her incredible work ethic and attention to detail were something that always inspired me during these years as graduate student and will keep guiding me in the future. I am also grateful to my PhD committee members, Professor Yifei Mo, Professor Chunsheng Wang, Professor Andrei Vedernikov, Professor Yuhuang Wang, Professor Jeffery Davis and Dr. Dat T. Tran for their commitment and time during my defense. I am very grateful to Dr. Liu's group members, especially Wei Wu, Emily Schulman, Sichao Cheng and Ali Kamali for their help and assistance with my experiments. I also would like to thank the collaborators from CCEI (Catalysis Center for Energy Innovation) community and ARL (Army research lab) for the constructive discussion and help in the material characterization. I would like to express my gratitude to my family, especially my mother, who has loved and encouraged me unconditionally. She may not understand my research area, but she has supported every decision that I made and have faith in me even when I did not. I also would like to thank my husband for being supportive during my graduate study, he made the bitter times sweet and memorable when I encounter difficulties. Without my family's support and encouragement, this journey would not have been achievable.

Table of Contents

Chapter 1: Introduction

1.1 Supported metal catalysts

Supported catalysts play a critical role in our modern chemical, petroleum, and petrochemical industry. Many important industrial processes such as chemicals manufacturing, oil refining, and environmental catalysis rely heavily on supported metal catalysts.[1] The supported catalysts usually contain two phases: the active phase that consists of nm-scale metal or metal oxide clusters/nanoparticles; and support phases where the active phase is deposited onto. The utilization of support can help reduce the amount of precious metal usage by increasing the metal dispersion.

As precious metals, especially platinum group metals (ruthenium, rhodium, palladium, and platinum) are commonly used as active phase due to their ability to catalyze reactions with higher activity and selectivity under milder conditions as compared to other metals, it is crucial to reduce the usage of precious metals to meet the sustainable requirement of catalyst development. The increase of the dispersion of precious metal could increase the atomic efficiency of the metal active phase, therefore the development of high dispersion catalysts has become one of the major focuses of heterogeneous catalyst study. Table 1.1 summarizes several of the most industrially important reactions and the high dispersion supported metal catalyst used for these reactions.[2-12] Compared to commercial supported catalysts that usually contains metal nanoparticles with size range between 2-10 nm, the metal active sites on high

dispersion catalysts are finely dispersed on support with size <2 nm. While the size of the metal structure reduced to nanometer or subnanometer clusters and further to atoms/ions, the highly dispersed sites exhibit different catalytic properties from bulk metal crystals due to size effect and metal support interaction etc.[13-15] Therefore another goal of heterogeneous catalyst research is to understand how the decrease of the size of metal active phase alters the intrinsic catalytic properties of supported catalysts.

Table 1.1 Summary of industrially important catalytic reactions catalyzed by high dispersion catalysts

Type of reaction	**reactants**	**Catalysts used**	**Reference**
Ammonia oxidation	NH_3+O_2	Pt, Ru, Ir, Pt-Ru	2-4
Automobile exhaust NO_x, SO_2, CO oxidation	NO_x+O_2 SO_2+O_2 $CO+O_2$	Pt, Pd, Ru on Al_2O_3, CeO_2	5-6
Hydrogenation dehydrogenation	Acetylene+H_2, ethylbenzene, propane, ethane	Fe, Pt, Pt-Zn on zeolite and metal oxide	7-9
Biomass conversion	Ligin +H_2, cellulose etc.	Pt, Ni, Co, Mo on zeolite and metal oxide	10-12

1.2 Synthesis of high dispersion metal catalysts

1.2.1 Challenges for synthesizing high dispersion metal catalysts

As the size of metal particle decreases, the surface free energy increases drastically. The ultra-small metal species have great tendency to aggregate to form large nanoparticles during the synthesis process. Therefore, it is very challenging to synthesize high dispersion metal catalyst with high surface loadings. In addition, the ultra-small metal particles are often unstable because of sintering during catalytic reactions especially under high temperatures, resulting in the loss of activity or selectivity. Two mechanisms for sintering of nanoparticles have been proposed: particle migration and coalescence (PMC) and Ostwald ripening (OR). In particular, PMC involves the migration of particles in a Brownian-like motion on the support surface, with subsequent coalescence leading to nanoparticle growth, whereas OR is caused by the migration of adatoms or mobile molecular species, which is driven by the differences in free energy and local adatom concentrations on the support surface.[16] It is important to design the catalyst structure to prevent the migration of metal atoms to avoid sintering through either pathways. The anchoring of highly dispersed metal active sites densely and tightly onto support materials continues to be a main challenge in the development of novel high dispersion catalyst systems. Many strategies have been developed to address this challenge, including the utilization of coordinatively unsaturated sites on support surface,[17] support with surface defects and with excess

atoms to form hollow sites.[18] In the following sections, the attempts to synthesize thermally stable high dispersion catalysts were discussed.

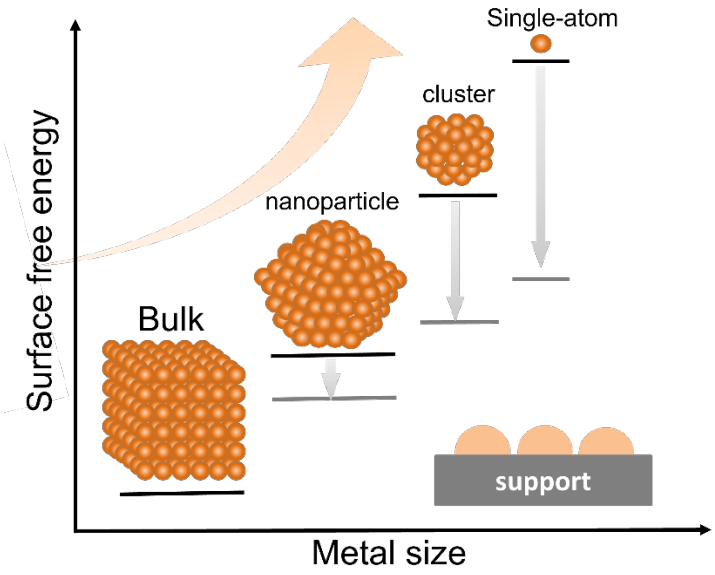

Figure 1.1 Scheme of the relationship between the metal sizes and the corresponding surface free energy on support. [19]

1.2.2 Approaches for synthesizing high dispersion metal catalysts

1.2.2.1 Wet-chemistry approaches

The synthesis of high dispersion catalyst by wet-chemistry method has a long history due to the low cost, easy accessibility, and feasibility for large scale manufacture. The wet-chemistry synthesis of high dispersion supported metal catalyst usually involves with the following steps: 1) the introduction of metal precursor to

support by ion-exchange or wetness impregnation, deposition–precipitation, or coprecipitation; 2) drying and calcination to form metal clusters or single atoms on support; 3) reduction or activation of the catalyst. In order to prevent aggregation or sintering during the synthesis process and reaction, the metal loading of wet chemistry method was typically controlled to be extremely low, therefore this approach is generally not suitable to synthesize high dispersion catalyst with high density of metal active sites. In the first paper that prepared single atom Pt on FeO_x support by coprecipitation reported by Zhang's group,[20] the Pt loading was only 0.17 wt. %. Besides low loadings, a portion of the metal sites prepared by this method could be buried inside the support matrix and not accessible during the reaction. To address this issue, the adjustment of the interaction between metal precursor and the anchoring sites of the support became important. Strong electrostatic adsorption has been adapted to increase the adsorption force between metal precursor and support in wetness impregnation synthesis.[21, 22] Zheng's group have recently developed a photochemical route for synthesizing stable singly dispersed Pd on TiO_2 catalyst with Pd loading over 1.5 wt.%.[23] The photochemical treatment stabilized the isolated Pd atoms by strengthening its interaction with support, accompanied by the stepwise removement of Cl^- ligands. With deeper understanding of the metal-support interactions, the wet-chemistry method remains as a promising approach to synthesis high dispersion catalysts for industrial applications.

1.2.2.2 Morphology engineering of catalyst support

In order to increase the amount of anchoring site and increase the interaction between metal active site and support, the morphology engineering of catalyst support was exploited to synthesize high dispersion catalysts. One of the strategies is using two-dimensional nanomaterial with high surface area and defect density as support. As the support surface area increase, the support could offer more possible sites (i.e. corner, terrace and defect sites) to form thermodynamically stable structure with metal atoms. As the work reported by Zhou et al., self-organized anodic TiO_2 nanotube was chosen as support for the effective iridium atom trapping due to the unique morphology and abundant density of Ti^{3+}-O_v defects.[24] Similar strategy was reported by Hejazi et al. that the thin sputtered TiO_2 anatase was used as support to increase the Pt atom dispersion for photocatalytic H_2 generation reaction.[25] Besides the ability to increase anchoring sites, morphology engineering of support can also induce spatial confinement of the metal species to prevent their mobility. This spatial confinement or caging effect utilizes the porous properties of the support material such as cavities of MOFs and tunnels of zeolites to separate and encapsulate metal precursors, and eventually achieve high dispersion of the metal species. For example, Corma's group demonstrated the synthesis of a zeolite-confined subnanometric Pt catalyst by entrapping Pt complex into the lamellar zeolitic precursor during the swelling process.[26] The molecular-scale cages of the MOFs could also be used to encapsulate metal atoms. Chen et al. reported Fe precusor confined within the pore and cavity of ZIF-8 to achieve a high dispersion of metal species. After pyrolysis, the ZIF-8 was fully

transformed into N-doped porous carbon, where the N-rich defects further provided a protective fence to avoid aggregation.[27]

1.2.2.3 Defect engineering of catalyst support

Defect of metal oxides can affect the fundamental properties of the material.[28] The electrical, optical, magnetic, thermal and mechanic properties of metal oxide materials could be determined by the intrinsic or externally introduced defect. Defect engineering introduces defect into the material through mainly two pathways: modification during crystal growth and post synthesis processing, which gives tunability and diversity of the engineered defects. Dopant could be added during the metal oxide synthesis step to improve absorption competence and enhance electron-hole pair isolation in photocatalysis.[29, 30] Surface modification techniques including high temperature treatment,[31] and laser irradiation[32] were also generally used to tune the optical and photocatalytic properties of metal oxide materials.

Benefited from the various methods to introduce defect on support materials, defect engineering became a versatile strategy to stabilize metal atoms for the synthesis of high dispersion catalyst. These defects in the support can serve as traps to capture metal atoms during the synthesis process, change the electronic and coordination environment of the atoms, which fundamentally induced stronger metal-support interactions to stabilize the metal atoms from aggregation. Many works have employed this strategy to synthesize high dispersion catalysts with high metal weight loading. He

et al. used the defect engineering of MOF framework to inhibit metal aggregation, and the strategy consequently resulted in an approximately 70% increase in single metal atom yield.[33] Zhang et al. exploited cation vacancy to synthesize high weight loading (up to 2.3 wt.%) of Pt single atoms on defect-rich $Ni(OH)_x$ nanoboards with abundant Ni^{2+} vacancies.[34] Compared to other synthesis strategy, defect engineering strategy can easily tune the metal dispersion by controlling the concentration of defects. Besides, the presence of defects on supports is helpful for the formation of unique atomic/electronic structure to enhance catalytic performance. It could be foreseen that defect engineering would continue to be an effective method to construct high dispersion catalyst with high metal loading and exceptional catalytic performance in the future.

1.3 Characterization of high dispersion metal catalysts

After the synthesis of high dispersion metal catalysts, it is important to characterize the catalyst to confirm the structure of catalytic active sites. The characterization of the catalytically relevant physicochemical properties (i.e. electronic structure, atomic configuration, charge state, bonding interactions with support) of catalysts can provide mechanism understanding of the structural-functional relationship of the synthesized novel catalysts, which could benefit the design and optimization of catalysts for desired reactions. However, the sub-angstrom characterization of highly dispersed active site is challenging and requires advanced

techniques to distinguish highly dispersed metal clusters and single atoms. In the following sections, characterization techniques for high dispersion metal catalysts, especially the techniques for single atom catalysts, were compared and the challenges of characterizing these group of catalysts were discussed.

1.3.1 Technics for the characterization of high dispersion catalysts

The characterization of high dispersion catalysts could be categorized into two types: 1) the direct characterization methods such as scanning tunneling microscopy (STM), high-angle annular dark-field imaging (HAADF STEM), and extended X-ray absorption fine structure (EXAFS) that could provide direct information of the dispersion and coordination structure of the active sites; 2) the indirect characterization methods that were able to reveal the important catalytically related physicochemical properties of the catalysts, for example X-ray photoelectron spectroscopy (XPS), X-ray absorption near edge structure (XANES), diffuse reflectance infrared Fourier transform spectroscopy (DRIFTS) and temperature programed reduction (H_2-TPR).

The development of imaging technique enables electron microscopy to resolve structures in atomic scale and profoundly benefits the studies of high dispersion metal catalysts especially single atom catalysts. STM, HAADF imaging and aberration-corrected-STEM have facilitated the direct observation of metal atoms on support.[35-37] EXAFS technique can be used to characterize the fine structures by studying the absorption at energies greater than the threshold for core electron release. This

absorption spectroscopy can provide information about the number of different coordinating atoms, the distances from the absorber atom, and the angles between chemical bonds. For example, Ren et al. used EXAFS to study the coordination environment of Pt single atoms on a Fe_2O_3 support that controlled by their synthesis method.[38] From the EXAFS spectra, the Pt-O coordination number decreases with increasing treatment temperature, and the catalytic activity of the catalyst were found to increase with the decrease of Pt coordination number.

X-ray based spectroscopy techniques are generally used to study the electronic property of supported metal catalysts. XPS is a surface sensitive technique often used for catalyst characterization. The electronic state of metal active sites within catalyst can be determined by this technique, which is helpful in understanding the electronic structure of the catalyst. X-ray absorption near edge structure (XANES) can be used for studying the oxidation state, coordination environment as well as local symmetry of elements, which could provide detailed information of the oxidation state and coordination of the element of interest.[39] CO probe molecule IR spectroscopy or DRIFTS is another site-specific technique in high dispersion catalyst characterization. The CO adsorption behavior on active sites can provide insights into the local geometry, homogeneity, and reactivity of the active species, therefore are widely used in the characterization of high dispersion catalysts and single atom catalysts.[21, 40, 41] In addition, advanced computational methods i.e. density functional theory (DFT)

calculations can be used to confirm the most stable configuration of active sites and provide important information on atomic structure of the catalyst.[42]

1.3.2 Challenges of characterization of high dispersion catalysts

Due to the confounding factors such as low weight loading, ultra-small size, the atomic scale of heterogeneity of bonding and the presence of metal-support interaction, the reliable characterization of high dispersion catalysts remains challenging in heterogeneous catalysis field. For high resolution imaging techniques, since small area of sample can be scanned at one time, electron microscopy suffers from statistical limitation. The inability of resolving single atom and relatively high detection yet limits XPS to completely fulfill the need of atomic scale characterization. As for XAS technique, though it has higher resolution and sensitivity than XPS, it requires advanced instrument and is not easily accessible for most researchers. Furthermore, the mixture of state also increases the complexity in data interpretation when sample contains inhomogeneous active site. As reported by Resasco group, the Pt/CeO_2 samples consisting of exclusively Pt single atoms and those with coexisting Pt single atoms and oxidized Pt clusters showed qualitatively similar XAS spectra because both samples lack of strong Pt-O-Pt scattering.[43] The difficulty in distinguishing the vibrational band of CO adsorb to different site by CO DRIFTS originated from metal-support interaction. The vibrational bands of CO adsorb on different type of sites are sometimes close to or even overlap with each other, therefore the interpretation of data

requires caution. Karim group reported that the CO band located at 2082 cm^{-1} is attributed to linear CO adsorption on Pt single atom.[44] However, as reported by DeRita et al., the CO band positioned at the same wavenumber region corresponded to CO adsorption on Pt clusters of the same catalyst system.[21] Limited by the shortcomings of these characterization techniques, combination of different characterizations are usually needed to get comprehensive understanding of the catalyst structure.

1.4 Strong metal-support interaction

Strong metal-support interaction (SMSI) in supported metal catalysts has drown great attention in recent years due to its potentiality in modulating the activity, selectivity, and stability of heterogeneous catalysts. SMSI typically originated from the interaction between group VIII noble metal nanoparticles and reducible supports, which was often accompanied by the formation of encapsulation overlayers on the metal nanoparticles. This phenomenon was first reported by Tauster et al. in 1978.[45] They discovered that the chemisorption abilities of small gas molecules (such as CO and H_2) of TiO_2-supported Group VIII noble metal catalysts suddenly disappeared after a reduction treatment at 500 °C, and this adsorption abilities could be entirely reversible by oxidation treatment of the sample at 400 °C. It was not until 2016, with the development of in-situ HRTEM technology, the dynamic process of the formation of the SMSI overlayer of TiO_x on Pd nanoparticle at different temperatures was firstly visualized by Pan's group.[46] The word strong was meant to emphasize that in this

metal-support interaction strong interfacial metal-metal bonds were formed.[47] The first direct evidence of the formation of this metal-metal bond was reported in 1986 by Haller's group with extended X-ray absorption fine structure spectroscopy (EXAFS).[48] However due to the difficulty in detecting the small amount of interfacial bonds in supported metal catalysts, SMSI is usually identified by the apparent physicochemical property change of the catalyst such as encapsulation of metal active site and loss of chemisorption ability.

In recent years, several novel catalyst systems that were beyond the category of noble metal and reducible support were discovered. For example, the SMSI effect between Au and irreducible metal oxide support ZnO,[49] and Pt with SiO_2.[50] Even non-oxide support can also exhibit this interaction with metal nanoparticle. It has been reported that hydroxyapatite,[51] boron nitride,[52] and molybdenum carbide[53] showed the ability to have SMSI effect. The study of SMSI provides fundamental understanding of the interaction between metal and support material, which gives possibility to the rational design and modulation of advanced catalysts for heterogeneous reactions.

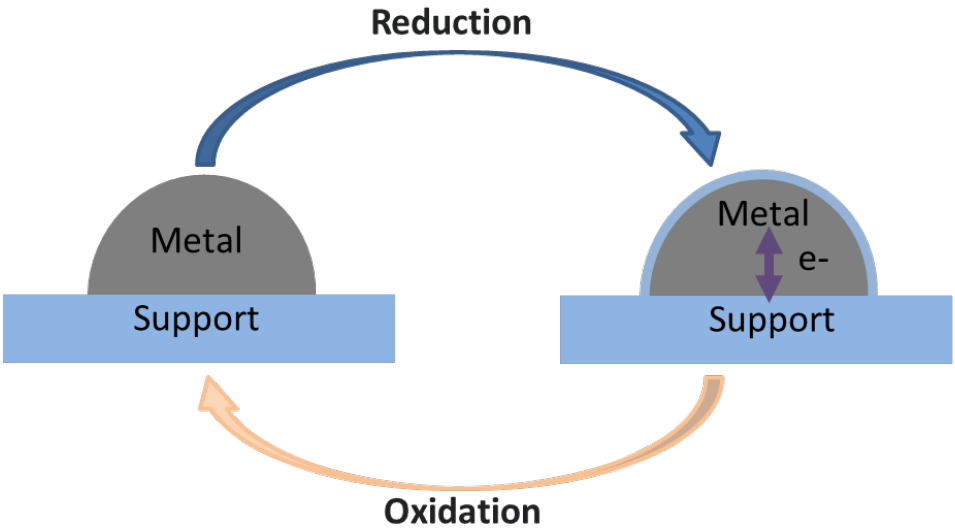

Figure 1.2 Scheme of strong metal-support interaction.

1.4.1 Effects of strong metal-support interaction

The properties of metal and support are greatly affected by strong metal-support interaction. The formation of interfacial bonds and charge redistribution between metal and support give rises to unique effects of SMSI. Two major effects of SMSI were extensively studied: 1) geometric effect, the interfacial atom transport, and 2) electronic effect, the interfacial charge redistribution.[54]

It has been agreed that SMSI between metal and reducible oxide support involves with the formation of oxide overlayer on metal surface by partial or complete encapsulation of the metal nanoparticle. This encapsulation phenomenon demonstrates the first effect of SMSI, which is the geometric change of the catalyst surface. Much

research has been conducted to understand the mechanisms of the encapsulation. The most popular explanation is that the encapsulation of metal nanoparticle of high surface energy (such as Pt or Pd) could minimize the surface energy of the system.[55] Fu et al. proposed the mechanism of encapsulation of Pd by TiO_2 contained two steps.[56] Firstly, due to the high diffusivity of titanium in TiO_2 at high temperatures, interstitial Ti cations would transport to near surface region. Secondly, it was the mass transfer of TiO_x to supported metal nanoparticles that formed the encapsulation overlayer. During which process, the low surface energy oxides overed the metal particles with high surface energy. The behavior was caused by the requirement to minimize total energy. Other geometric effect such as flattening of the metal particle on the reducible support that reported by Caballero's group[57] could also be viewed as the effect of SMSI. These geometric effect of SMSI helped anchoring the metal nanoparticle on the support, preventing the migration of nanoparticle which enhanced the stability of the catalyst under harsh reaction conditions.

The second effect induced by strong metal-support interaction is electronic effect, which is often referred as electronic metal-support interaction (EMSI).[58] The physical contact between metal nanoparticle and support induced a charge redistribution at the interface and resulted in the electronic effect. The electronic effect is often used to explain catalytic performance difference of the SMSI system. The electronic effect is governed by the fermi level of metal nanoparticle and the support, and ultimately the energy minimization of the electron chemical potentials.[59] The local electronic rearrangement could involve with a few atomic layers at the interface, and

sometimes could even change the oxidation state of the metal atoms from the supported metal nanoparticle. The property of metal nanoparticle and support could both affect the electronic effect originated from SMSI. As the size of metal nanoparticle decreases, the electronic state of the nanoparticle becomes more localized, which could affect the electron transfer. For the support material, many properties have impact on the electronic effect, such as morphology, conductivity, reducibility, exposed crystal planes, and surface defects. Modulating these properties of metal nanoparticle and support could provide insights into the control of charge transfer of the interface, and eventually the optimization of catalytic performance by changing the electronic structure of the active sites.

Besides geometric effect and electronic effect, other effects have been recently discovered that involves with SMSI. One of the effects is the redispersion or reconstruction of the metal nanoparticle. Zhang's group reported a method to redisperse Pt nanoparticle into Pt single atom on FeO_x support by strong metal-support interaction.[60] Dong et al. applied the carbonization treatment for Au NPs supported on MoO_3 to introduce SMSI effect.[61] During which process, large Au nanoparticles redispersed to form thin Au overlayers on Mo_2C support. Another effect that introduced by SMSI was bifunctional effect, which was introduced by the perimeter sites at the boundary of the metal and support. This effect often associates with the activated reactant spillover from the metal site to support. For example, in water gas shift reaction, the oxygen vacancies of TiO_2 near the metal-support perimeter can participate in the reaction path.[62]

1.4.2 Application of strong metal-support interaction

Owning to the unique geometric and electronic property change arise from the strong metal-support interaction. SMSI were widely used as effective strategy to enhance the stability, activity, and selectivity in various thermocatalytic and electrocatalytic reactions. As the encapsulation overlayer could limit the migration of metal nanoparticles, SMSI has been recognized as a practical method to enhance the stability of catalysts under harsh conditions. The encapsulation structure also increases the interface region of metal and support, providing more interfacial sites that exhibit different adsorption behavior of reactant molecules, which means the selectivity of the catalyst can be tuned by SMSI. Zhang et al. reported that the CO_2 hydrogenation selectivity from CH_4 to sole production of CO of Ir/TiO_2 catalyst could be tuned by modulating the strong metal-support interaction.[63] The SMSI was also used to modulate the electronic properties of the active sites of supported metal catalysts to improve the catalytic activity. Xu et al. reported that the electron density of interfacial Ni ($Ni^{\delta-}$) could be increase by introducing SMSI into the Ni/TiO_{2-x} catalyst, the optimized catalyst showed an extraordinary improvement of catalytic activity in water gas shift reaction.[64] With a deeper understanding of the metal support interaction mechanism, constructing SMSI systems can be used for designing unique structures of supported metal catalysts at atomic scale for applications in numerous of chemical reactions.

1.4.3 Effects of defects on strong metal-support interaction

Defect engineering strategy has been extensively used in the preparation of supported metal catalysts, as defect can serve as effective trap for stabilizing metal species via significantly enhanced metal–support interaction.[65, 66] Defects (i.e. cationic or anionic defects) that exist widely in metal oxides can function as anchoring sites for stabilizing metal atoms, and as promoter or active sites to facilitate catalytic reaction. As defects being introduced in support material, the coordination environment and electronic structure of metal oxides are changed, which leads to the enhancement of metal-support interaction by decreased bond distance. In one of the earliest studies of SMSI behavior of Pt/TiO_2 system, Horsley reported that Pt atoms were inserted in the surface oxygen vacancy of support.[67] The oxygen vacancy reduced the bonding distance between the metal atom and the surface cation and therefore enabled the formation of metal–metal bond, which provided possible mechanisms for the suppression of H_2 chemisorption of SMSI.

The introduction of defects also causes the redistribution of electrons that could help stabilize metal species by increasing the adsorption energy around oxygen defects. Han et al. used DFT calculations to study the adsorption of Pt atoms on defective TiO_2 surface.[68] The oxygen vacancy site was found to be the most active site for Pt adatom with an adsorption energy of 4.87 eV. Besides changing the adsorption behavior, the electronic metal-support interaction could also be altered by the introduction of defects. Dong et al. investigated the electronic states of the supported metal atoms with the influence of oxygen vacancy using DFT calculations.[69] It has been found that when the

oxygen defect was introduced in the yttrium-stabilized zirconia (YSZ) support, the d-band centers of the adsorbed metal atoms would shift closer to the Fermi level owing to the charge transfer to the adatoms. This result indicated that the oxygen vacancy served as an electron donator, which was beneficial for stabilizing the adatoms and changing the d-band centers of metal atoms and ultimately their catalytic activity. Similarly, the experimental studies on the electronic interaction between metal atoms and defective oxides also have shown that the charge transfer in supported in supported metal catalysts could lead to more positively charged metal atoms, which granted the catalysts with superior activity and selectivity.[70, 71]

1.5 Thesis overview

This dissertation with focus on the development of high dispersion supported metal catalysts for selective hydrogenation via defect engineering approach is divided into 5 chapters. The first chapter introduces the motivation behind our research on developing synthesis and characterization strategy of high dispersion metal catalyst, as well as the investigation of the origin and effect of strong metal-support interactions in supported catalysts. Chapter 1 also includes a comprehensive review of the current strategies for high dispersion catalyst synthesis and characterization, along with the introduction of the effects and application of metal support interaction in heterogeneous catalysis.

Chapter 2 introduces a new wet-chemistry method to tune the strong metal-support interaction of Pt/TiO_2 system. As series of physicochemical characterization

on the catalysts indicated, the geometric and electronic properties of Pt/TiO_2 catalysts changed with increasing the pH of impregnation solution. The hydrogenation activity of the catalysts showed significant difference in the hydrogenation of vinyl and nitro group, which suggested different extent of strong metal-support interaction. By controlling the pH of the impregnation solution, the SMSI effect of the synthesized catalyst could be adjusted.

Chapter 3 establishes the relationship between the Pt dispersion and styrene hydrogenation activity of Pt/TiO_2 catalysts with Pt size ranging from single atoms to nanoparticles. The nanometer-sized Pt clusters have shown significantly higher activity than Pt nanoparticles, sub-nanometer clusters or isolated single atoms. Detailed characterization of Pt/TiO_2 of different Pt size reveals that the geometric and electronic properties of the Pt sites affected the hydrogenation activity. With this established particle size versus hydrogenation activity relationship, the Pt dispersion of a newly synthesized supported catalyst could be estimated. This method has the potential to be used as a facile way to pre-screen supported metal catalysts with various particle sizes in other catalyst systems.

Chapter 4 describes a new defect engineering strategy to introduce structural defects (i.e., oxygen vacancy (O_v) and Ti^{3+}) into TiO_2 support material by laser engraving under ambient atmosphere. The defects created by laser engraving are more stable than those already existed in the pristine TiO_2 or those created by high temperature reduction treatment. The TiO_2 treated by laser engraving showed significantly higher redox properties because of the defective structure, which caused

changes in the metal-support interaction between Pt and TiO_2 support. Subsequently the enhanced redox capability of resulted Pt/TiO_2 catalyst enabled higher reactivity and selectivity in hydrogenation of 3-nitrostyrene and furfuryl alcohol.

Chapter 5 summarizes the work conducted on the high dispersion Pt/TiO_2 catalysts constructed via defect engineering strategy, along with the effect of metal-support interaction on the selective hydrogenation reaction performance. Future works on expending the current project to other metal oxide support materials with different reducibility was outlined.

Chapter 2: Tuning the strong metal support interaction of Pt/TiO2 system by impregnation pH control

2.1 Introduction

Strong metal support interaction (SMSI) in heterogeneous catalyst systems has played an important role in enhancing the catalytic activity, selectivity, and stability. Various studies have been dedicated to exploring the approaches to tune the strong metal support interaction in order to optimize the reaction performance of catalyst. For example, reduction-oxidation (RO) cycles are the most reported method to regulate the interaction between group 11 metal on reducible support. In which process, the SMSI effect is generated by reducing treatment, and the SMSI state can be reversed by applying a subsequent oxidative treatment. Mejía and coworkers applied this RO cycles on cobalt on TiO_2 or Nb_2O_5 catalysts, the catalytic activity of resulted catalyst in Fischer-Tropsch reaction has been greatly improved.[72] Other approaches such as doping of the support,[73] addition of reducing agent,[74] overlayer deposition,[75, 76] and adsorbate mediation[77] were explored to induce and control the SMSI effect. However there were few reports that utilize wet chemistry method to tune the SMSI between metal and support during the catalyst synthesis stage.[78]

Wetness impregnation has been a general method to load metal nanocrystal on support in heterogeneous catalysts synthesis.[79] Based on this method, by precisely

controlling the adsorption of metal on support, one can decrease the size of metal nanoparticle and achieve atomic dispersion. Strong electrostatic adsorption (SEA) method has been reported to be a simple approach to synthesize single-atom catalyst by utilizing the coulombic interaction between the metal precursor and support to increase metal dispersion.[26] The surface of metal oxide support is negatively charged when it is deprotonated above a characteristic pH (point of zero charge (PZC)). Positively charged metal precursor (e. g. $Pt(NH_3)_4^{2+}$) will then be deposited on the surface via strong electrostatic adsorption. It has been proved this method can achieve better dispersion than traditional wetness impregnation without pH control.[27] In 2017, Christopher group has reported the effects of SEA solution pH on the dispersion of Pt atoms on TiO_2 support and the optimal pH to impregnate Pt on TiO_2.[21] It has been found that with increasing synthesis pH from 8-12.5, the IR spectra of CO gradually showed a narrower and symmetric peak at 2112 cm^{-1}, which corresponds to single Pt atom dispersion. However, the study of impregnation at even higher pH was not covered by their study. Whether further increasing of the impregnation would increase the adsorption interaction between metal precursor and charged support, and eventually achieve high Pt dispersion in higher Pt loadings by strong metal support interaction, has not been studied yet. In this chapter, the effect of impregnation pH on the dispersion of Pt and the SMSI between Pt and TiO_2 was systematically studied. Three catalysts were synthesized under different pH from neutral to highly basic, series of characterizations were conducted to understand the geometric/electronic properties change of the catalysts caused by synthesis pH. The hydrogenation performance of

different functional groups (vinyl and nitro group) with different polarity was tested to study the SMSI effect on catalytic activity and selectivity. It has been found that changing the pH of impregnation solution can tune the SMSI of Pt/TiO_2 system, which provided a new pathway for synthesizing supported catalysts with different metal support interactions.

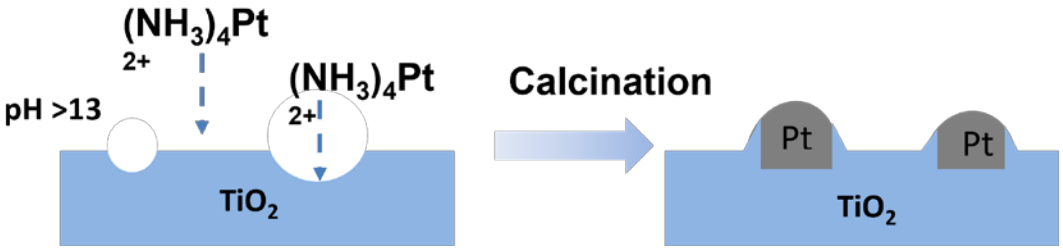

Figure 2.1 scheme of tuning pH during impregnation process to construct catalyst system with strong metal-support interaction.

2.2 Experiments

2.2.1 Materials

The TiO_2 support (anatase, 99.5% purity) was purchased from U.S. Research Nanomaterial. Tetraammineplatinum(II) nitrite (TAPN, >99.99% metal basis), was purchased from Alfa Aesar. The ammonia (NH_4OH) solution (28-30 wt.%) were bought from VWR. Styrene (>99.5% purity) and 3-Nitrostyrene (>97% purity) was purchased from Acros Organics. Deionized (DI) water was used herein was lab made.

2.2.2 Catalyst preparation

The Pt/TiO_2 catalysts with 0.50 wt.% Pt loading were prepared using modified SEA method[18]. Three Pt/TiO_2 catalysts were synthesized under different solution pH. 0.500 g of TiO_2 powder was dispersed in 50.00 mL of DI water, 1:3 and 3:1 diluted NH_4OH solution (volume ratio of 28-30 wt.% NH_4OH and DI water 1:3 and 3:1) respectively, which result the final Pt/TiO_2 catalysts denote as $Pt/TiO_{2\ WI}$, $Pt/TiO_{2\ LPH}$, $Pt/TiO_{2\ HPH}$. $Pt/TiO_{2\ WI}$ was prepared under neutral condition without the SEA effect, $Pt/TiO_{2\ LPH}$ was impregnated under pH = 12.85, and $Pt/TiO_{2\ HPH}$ was prepared under harsh basic condition with pH = 13.70. 0.085 g of TAPN was dissolved in 5.00 mL of DI water in a glass vial to form the stock solution. 0.090g of TAPN stock solution was added into a 25 mL of solvent that was same as the TiO_2 suspension respectively. The diluted TAPN solution was then transferred into a syringe and was added into the TiO_2 suspension using a syringe pump (Pump 11, Harvard Apparatus) at a rate of 2 mL/hr. Afterwards, the mixture was placed in a convection oven (VWR Sheldon Manufacturing Model, 1350GM Gravity Convection Oven) that was preheated to 343 K. After the sample had fully dried in the oven, it was calcined at 553 K (ramp rate of 5 K/min) for 4 h in a furnace (Thermo Scientific Lindberg/Blue M™ Multipurpose Box Furnaces). The air (Airgas, research grade) flow rate was kept at 50 mL/min during this calcination step. After the sample cooled down to room temperature, it was transferred into a tubular furnace for reduction at 423 K (ramp rate of 5 K/min) for 2 h. The gas atmosphere consisted of diluted H_2 ($5\%H_2/N_2$ mixture) at a flow rate 100 mL/min. The

reduced sample was then stored in a desiccator prior to characterization and reaction tests.

2.2.3 Catalyst characterization

Powder X-Ray diffraction (XRD) patterns of samples were recorded using a Bruker D8 Advance Lynx Powder Diffractometer (LynxEye PSD detector, sealed tube, Cu Kα radiation with Ni β-filter). N_2 adsorption-desorption isotherms of the samples were measured using an Autosorb-iQ equipment (Quantachrome Instruments) at 77 K. The samples were outgassed at 573 K for 10 h at 1 mmHg pressure prior to the measurements. Brunauer, Emmett and Teller (BET) method was used to determine the specific surface areas of the samples. The electronic property of Pt was characterized by X-ray photoelectron spectroscopy (XPS) by Versaprobe III by Physical Electronics Inc. (PHI) X-ray photoelectron spectrometer. Powders were deposited on carbon tape for sample immobilization in the chamber. X-rays were generated with a monochromated Al Kα anode at 25 W and a beam size of 100 μm. The chamber pressure during analysis was 5 x 10^{-6} Pa or less. Surveys were performed with a pass energy of 224 eV for each sample, and higher resolution elemental scans were collected with pass energies of 55 eV, both had take-off angles of 45 degrees. The morphology of TiO_2 samples were observed by transmission electron microscopy (TEM) using a JEM 2100 LaB6 electron microscope. The morphologies of Pt loaded samples were observed by scanning transmission electron microscopy (STEM) with Thermo

Scientific (FEI) Titan Themis S/TEM operating in probe mode at 200 kV with HAADF detector using gun lens 7 and spot size 7.

2.2.4 H_2-TPR and CO chemisorption measurements

Temperature programed reduction of the Pt/TiO_2 catalyst with H_2 (H_2-TPR) was carried out with same procedure as described in chapter 2 on a Quantachrome Autosorb iQ instrument. Prior to the measurement, each sample was subjected to a pre-treatment with 40 mL/min N_2 flow (Airgas, Research grade) at 553 K for 2 h. After cooled to 323 K, the gas was switched to 40 mL/min $5\%H_2/N_2$ and the sample was heated to 1173 K at 10 K/min ramp rate and kept at the final temperature for 10 min. A cold trap was used to remove water produced throughout each experiment from the outlet stream to avoid interference with the TCD signal.

The chemisorption of CO molecules on the catalyst was measured by pulse titration in the same equipment as the one used in H_2-TPR. 0.1g of catalyst was first treated in an Ar flow (50 mL/min) at 553 K for 4 h and then cooled down to 323 K. $5\%H_2/N_2$ at a flow rate of 50 mL min^{-1} was then introduced to in-situ reduce the catalyst for 1 h followed by Ar gas purge for 2 h. Afterwards, the sample was cooled down to 303 K in the Ar flowing gas. A series of CO pulses (50 uL in each pulse) were injected with an interval of 5 min until the amount of exit CO pulses reached a steady state value. The CO signal was recorded using a Prima BT Bench Top Process Mass Spectrometers (Thermo Fisher Scientific, winsford U.K. CW7 3GA).

2.2.5 Styrene hydrogenation reaction test

The catalytic activity of synthesized Pt/TiO_2 catalysts was tested by styrene hydrogenation with same procedure as described in chapter 2. 9.00 mL ethanol and 0.050 g catalyst were used in each reaction. After purging the reactor with H_2 for 30 min, the styrene solution (0.053 g styrene in 1.00 mL ethanol) was injected into the reactor, which moment was recorded as the starting time of the reaction. Reaction mixture was sampled by a syringe equipped with a needle from the left neck of the reactor. After filtering out the solid catalyst particles by syringe filter, the sampled solution was analyzed using a gas chromatography (Agilent 7890A) equipped with a methylsiloxane capillary column (HP-1, $50.0\,m \times 320\,\mu m \times 0.52\,\mu m$) and a flame ionization detector (FID).

2.2.6 3-nitrostyrene selective hydrogenation reaction test

The 3-nitrostyrene hydrogenation was conducted with similar procedure as styrene hydrogenation. 9.00 mL ethanol and 0.020 g catalyst were added into a 50 mL three-neck flask. After sonication of the catalyst mixture, the flask was placed in a water bath that was preheated to 313 K. A magnetic stirring bar (stirred at 900 rpm) was used to mix the suspension. After purging for 30 min, the 3-nitrostyrene solution (0.076 g styrene in 1.00 mL ethanol) was injected into the reactor. Reaction mixture was sampled by a syringe equipped with a needle from the left neck of the reactor.

After filtering out the solid catalyst particles by syringe filter, the sampled solution was analyzed using same gas chromatography equipment as styrene hydrogenation reaction described above.

2.3 Results and discussion

2.3.1 Geometric properties of TiO_2 support treated under different pH

In order to test the effects of SEA synthesis process on the structural properties of TiO2 support, the as-received TiO_2 support particles were exposed to the NH_4OH solution (NH_4OH: water volume ratio=1:3) for 6.25 h, then the solvent was evaporated at 343 K same as the SEA synthesis process. The as-prepared TiO_2 were firstly characterized by XRD to understand their crystalline structures changes. Figure 2.2 shows that the XRD peaks of the TiO_2 support without NH_4OH treatment are characteristic of anatase phase (JCPDS #75-1537). The average crystalline size is 7.87 nm, calculated from the Scherrer equation using the peak width at half the maximum intensity of the TiO_2 (004) diffraction peak. After the NH4OH treatment process, the anatase phase of TiO_2 support was maintained, as confirmed by the identical XRD patterns. The broadening in peak width at each diffraction peak indicates that the crystalline size of TiO_2 support was reduced, which could be caused by the corrosive NH_4OH media in the SEA process. The same calculation from the Scherrer equation showed that the average particle size is 4.13 nm and 3.68 nm, which resulted 42.3% and 48.6% decrease respectively compared to the TiO_2 support prior to exposure to the

basic solution. The decrease is more significant as the pH of the NH_4OH solution increases. The particle sizes evaluated from the XRD data are comparable to those measured by TEM images and BET surface area.

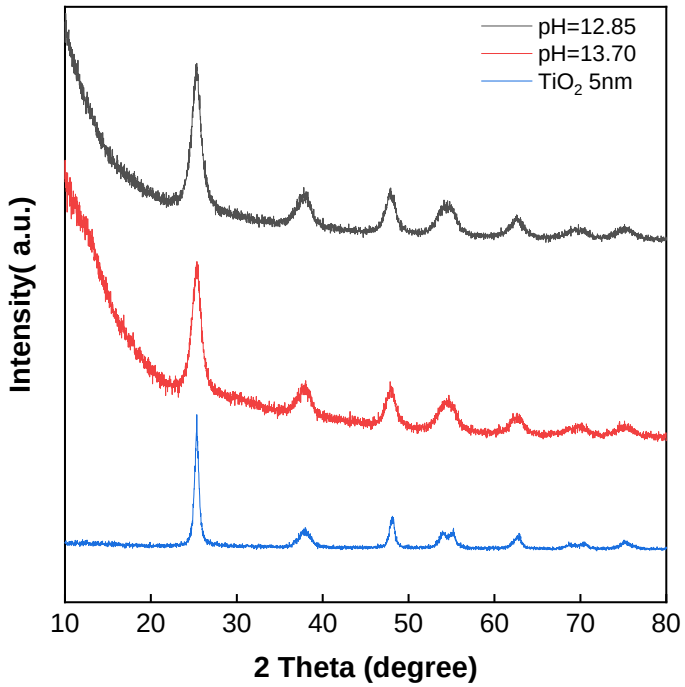

Figure 2.2 XRD patterns of TiO_2 treated by NH_4OH solution of different pH.

Figure 2.3 shows the TEM images of the as-received TiO_2 support particles and the ones after exposing to the SEA synthesis process at pH=12.85 and 13.70. As shown in Figure 2.3, before and after the SEA process, the TiO_2 support contains a number of aggregated particles. Individual particles were circled. The inset plot in each image is the particle size distribution data. The average particle sizes of TiO_2 support before SEA process are 6.72 nm. After SEA process the average particle size gradually

decreased to 6.60 nm and 6.21 nm, respectively. The decrease of average particle size of TiO_2 after NH_4OH treatment process was a direct indication of the corrosion of TiO_2 surface by basic NH_4OH solution.

(a)

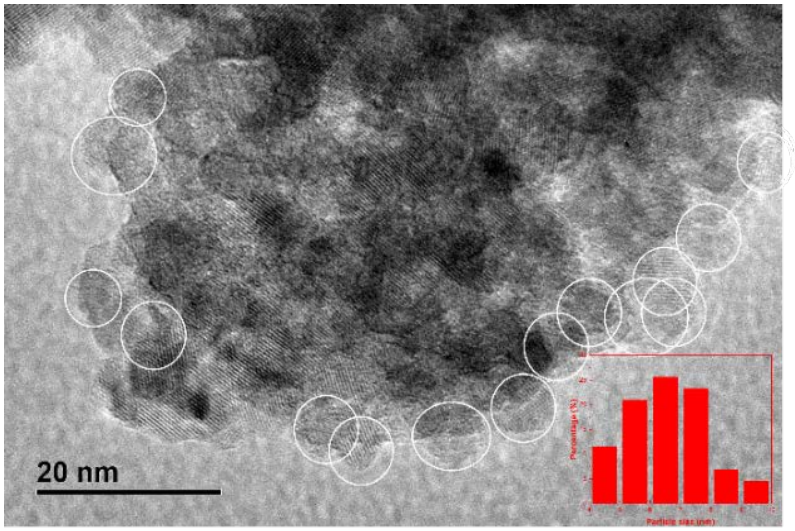

(b)

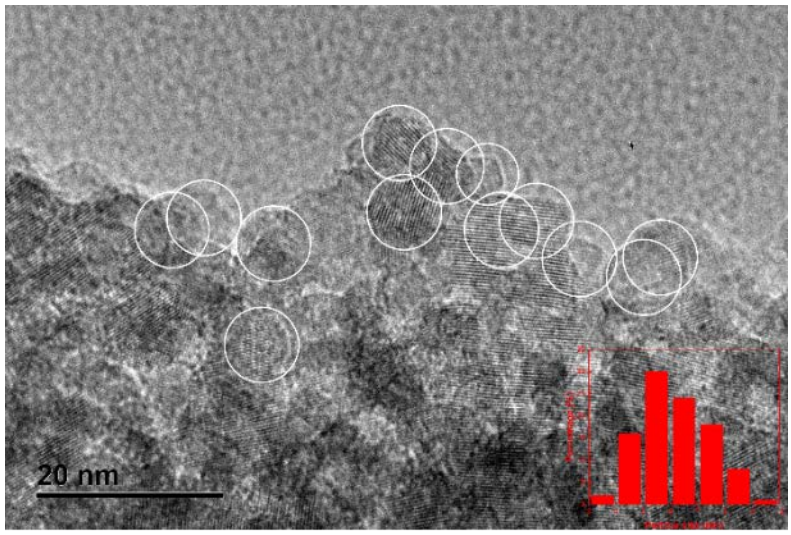

(c)

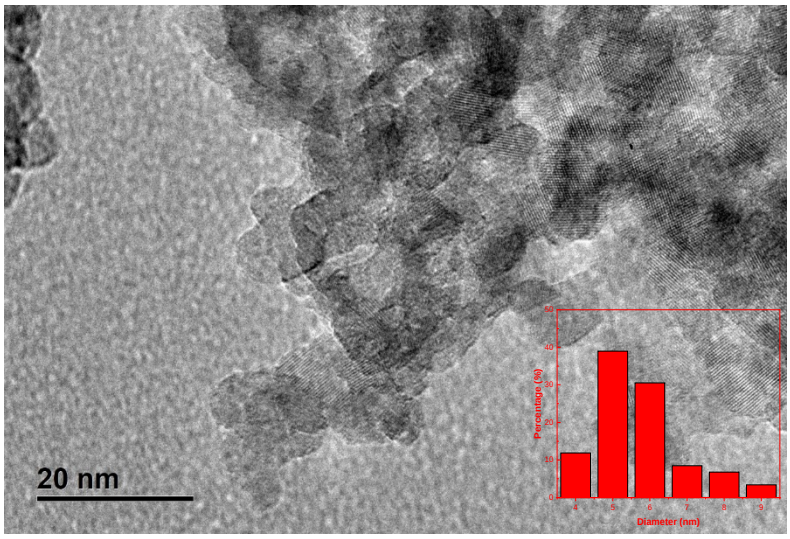

Figure 2.3 TEM images of as-received TiO_2 support (a), TiO_2 support after SEA synthesis procedure under pH =12.85 (b), TiO_2 support after SEA synthesis procedure under pH =13.70 (c).

Nitrogen (N_2) adsorption-desorption isotherms were used to determine the surface areas of TiO_2 particles. The measurements were conducted at 77 K on an Autosorb-iQ analyzer (Quantachrome Instruments). The samples were pretreated at 573 K and 1 mm Hg for 12 hours. The surface areas were determined using the Brunauer-Emmett-Teller (BET) method. Figure 2.4 show the N_2 isotherms of TiO_2 particles before and after the NH_4OH (pH=13.70) treatment in the SEA solution. The surface area of the TiO_2 particles increased from 185 to 228 m^2/g, accordingly, after the exposure to the basic NH_4OH solution. From these textural property characterization results, it could be concluded that the basic NH_4OH solution was able

to corrode the TiO_2 nanoparticle surface during the impregnation step. This corrosion decreases the particle size of TiO_2 and increases the BET surface area of the material. Due to the morphology change of the TiO_2 nanoparticle, it could also be inferred that the surface properties of the TiO_2 was also altered by the NH_4OH treatment, which could possibly change the dispersion and binding environment of the Pt loaded onto TiO_2 surface during the impregnation process.

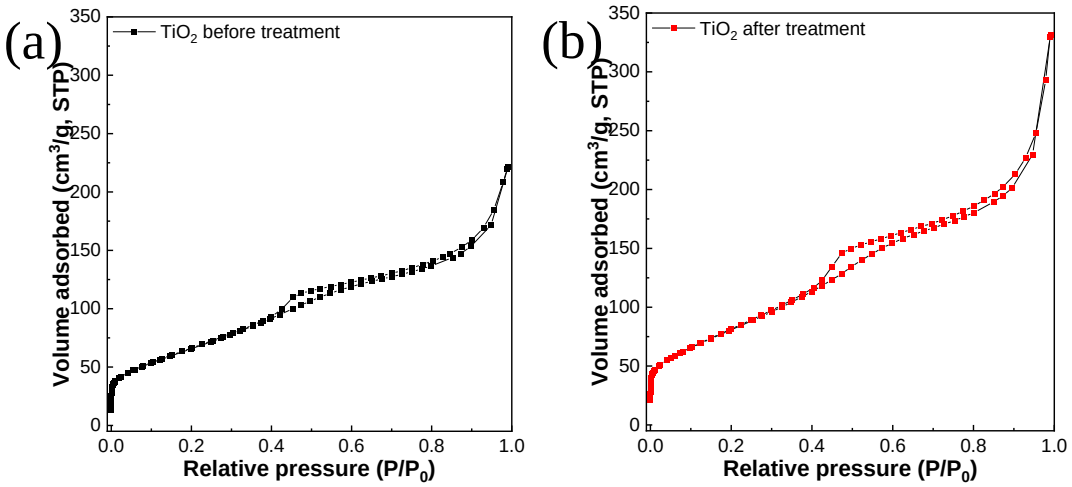

Figure 2.4 N_2 adsorption-desorption isotherms of TiO_2 particles before (a) and after (b) pH= 13.70 NH_4OH treatment.

2.3.2 Geometric properties of Pt nanoparticle in Pt/TiO_2 catalysts synthesized under different pH characterized by STEM

In order to study the effects of impregnation pH on the dispersion of Pt particles on TiO_2 support, the Pt/TiO_2 catalysts were examined by HAADF STEM imaging. As shown in Figure 2.5, the Pt dispersion on these three samples were uniform. Pt

nanoparticles with sizes around 1 nm were observed across the TiO_2 support. From detailed particle size analysis, it could be found that the $Pt/TiO_{2\ LPH}$ has the smallest average Pt particle size of 1.06 nm, which was smaller than $Pt/TiO_{2\ WI}$ that was prepared under neutral condition. This suggests that SEA synthesis method at appropriate pH could indeed increase the Pt dispersion on TiO_2 support. However, if the impregnation pH is further increased as in the $Pt/TiO_{2\ HPH}$ sample, the Pt average particle size increased as compared to the sample prepared at neutral condition ($Pt/TiO_{2\ WI}$) and lower SEA pH ($Pt/TiO_{2\ LPH}$), which meant that further increasing SEA solution pH did not create stronger adsorption force between Pt precursor and support. Instead, the Pt dispersion decreased slightly if the impregnation pH increased beyond the optimal pH region. It should be noted that STEM images are two-dimensional projection of the sample imaged, the contrast comes from the difference in atomic number and sample thickness. Therefore the relative position of Pt nanoparticle on support, for example whether the Pt locates on TiO_2 surface or encapsulated in TiO_2, could not be analyzed from the HAADF STEM images.

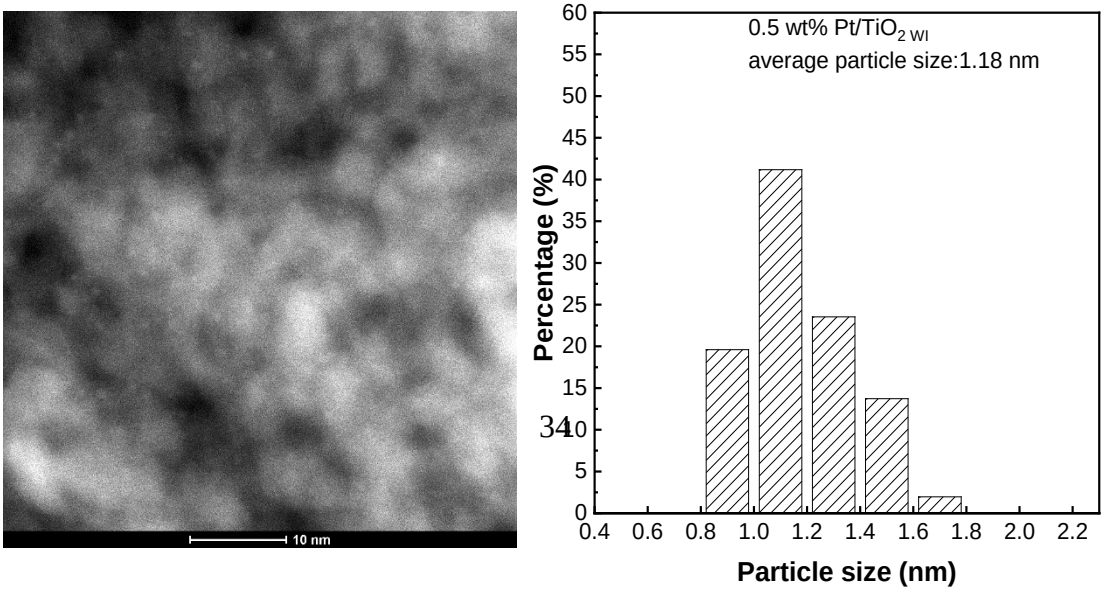

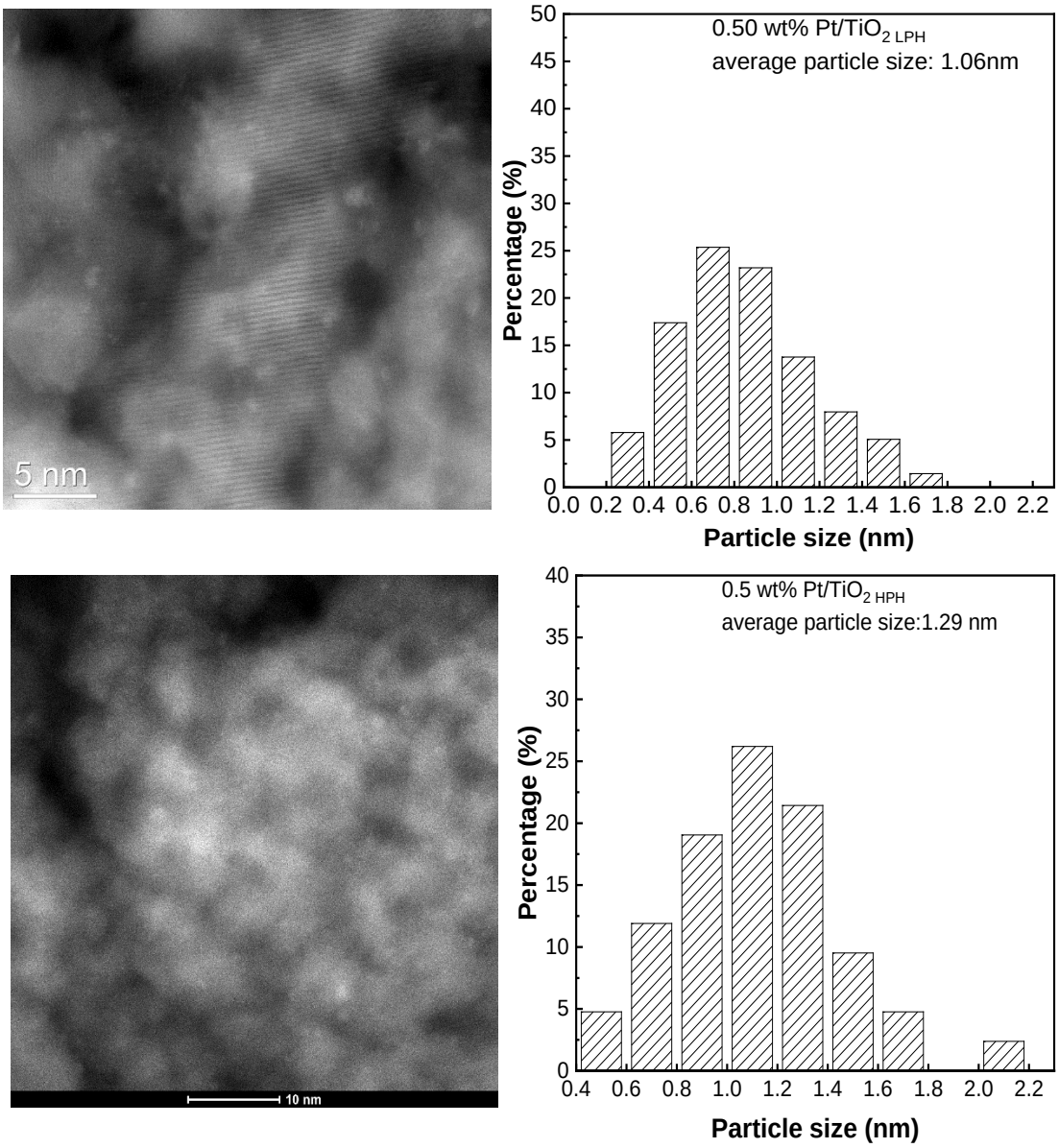

Figure 2.5 HAADF-STEM images and Pt particle size analysis of Pt/TiO_2 catalysts prepared under different pH condition (a) $Pt/TiO_{2\ WI}$, (b) $Pt/TiO_{2\ LPH}$, (c) $Pt/TiO_{2\ HPH}$.

2.3.3 Electronic properties of Pt/TiO_2 catalysts synthesized under different pH

The charge transfer from/to supported metal nanoparticle is a common phenomenon of strong metal-support interaction. The electronic structure of the metal nanoparticle could be changed by the charge transfer between the interface of metal and metal oxide support. To study the electronic properties of Pt nanoparticle loaded under different pH conditions, XPS spectra of Pt 4f region was obtained. Since the Pt $4f_{5/2}$ peak overlaps with the Ti 3s peak at 75.75 eV, only Pt $4f_{7/2}$ peak was selected for the electronic property analysis. As shown in figure 2.6, the Pt $4f_{7/2}$ peak of $Pt/TiO_{2\ WI}$ catalyst was located at 71.4 eV. This peak position blue shifted significantly when the impregnation pH was changed. The Pt $4f_{7/2}$ peak of $Pt/TiO_{2\ LPH}$ shifted to 72.0 eV. This 0.6 eV shift could be caused by the decrease of Pt nanoparticle size. As the size of Pt decreases, more Pt atoms stay at the interface of TiO_2. Therefore, due to the charge transfer from Pt to support the Pt nanoparticle became more cationic. Besides the formation of more interfacial Pt sites, as the Pt ultra-small nanoparticles were easily oxidized in air environment, more PtO_x could also be formed with the decrease of particle size. For $Pt/TiO_{2\ HPH}$ catalyst which the pH of impregnation solution was the most basic, the Pt $4f_{7/2}$ peak continued to shift to 72.2 eV. As indicated by the STEM image particle size analysis of Pt, the Pt particle size did not continue to decrease in $Pt/TiO_{2\ HPH}$ catalyst. The electronic property change of $Pt/TiO_{2\ HPH}$ was not caused by changes in particle size, instead it was possibly due to the change of Pt coordination environment. The Pt atoms in $Pt/TiO_{2\ HPH}$ were more coordinated to O instead of Pt,

which lead to the formation of cationic Pt nanoparticle. The cationic property of $Pt/TiO_{2\ HPH}$ suggested there was possible strong metal-support interaction between the Pt nanoparticle and TiO_2 support in this catalyst.

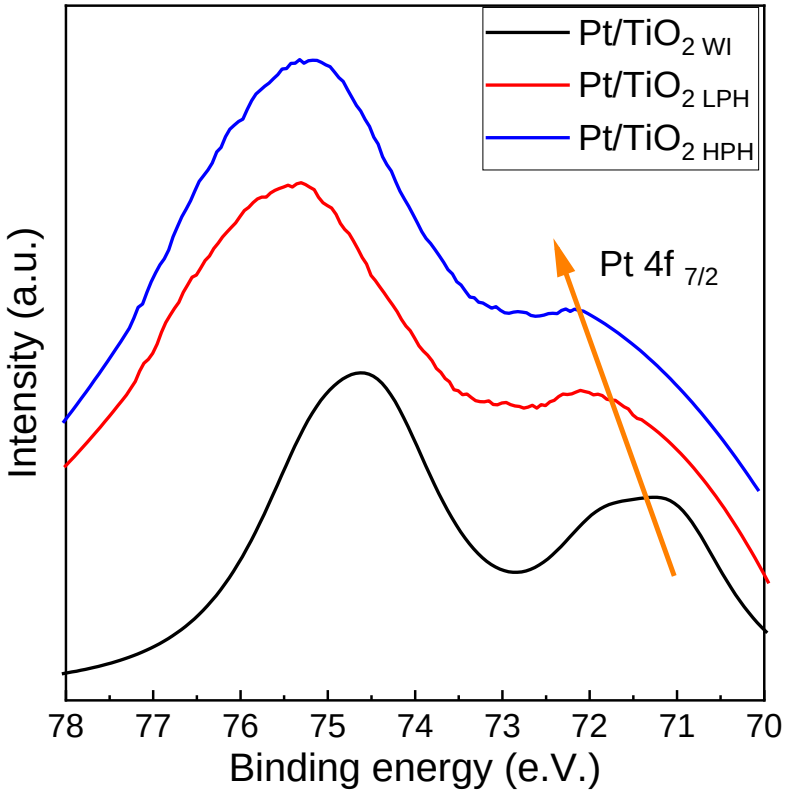

Figure 2.6 Pt 4f XPS spectra of Pt/TiO_2 synthesized under different pH conditions.

To further verify the Pt electronic property change, XANES was conducted on 1.0 wt% Pt/TiO_2 synthesized under different pH. It has been reported that the Pt edge position and intensity were affected by the geometry, alloying and absorbates of the Pt nanoparticle. The Pt loading was increased due to the instrument sensitivity here in this experiment. As shown in Figure 2.7, the Pt edge of $Pt/TiO_{2\ HPH}$ has shifted to higher

edge energy and the white line intensity has slightly increased as compared to the $Pt/TiO_{2\ LPH}$ sample. This change has indicated possible broadening of metal d band and an increase in the electron deficiency of Pt nanoparticle on of $TiO_{2\ HPH}$.[80] The enhanced cationic property of Pt nanoparticle on $TiO_{2\ HPH}$ was in agreement with the XPS spectra, the change in metal nanoparticle d band structure could lead to different absorption energy of absorbates such as CO and H.

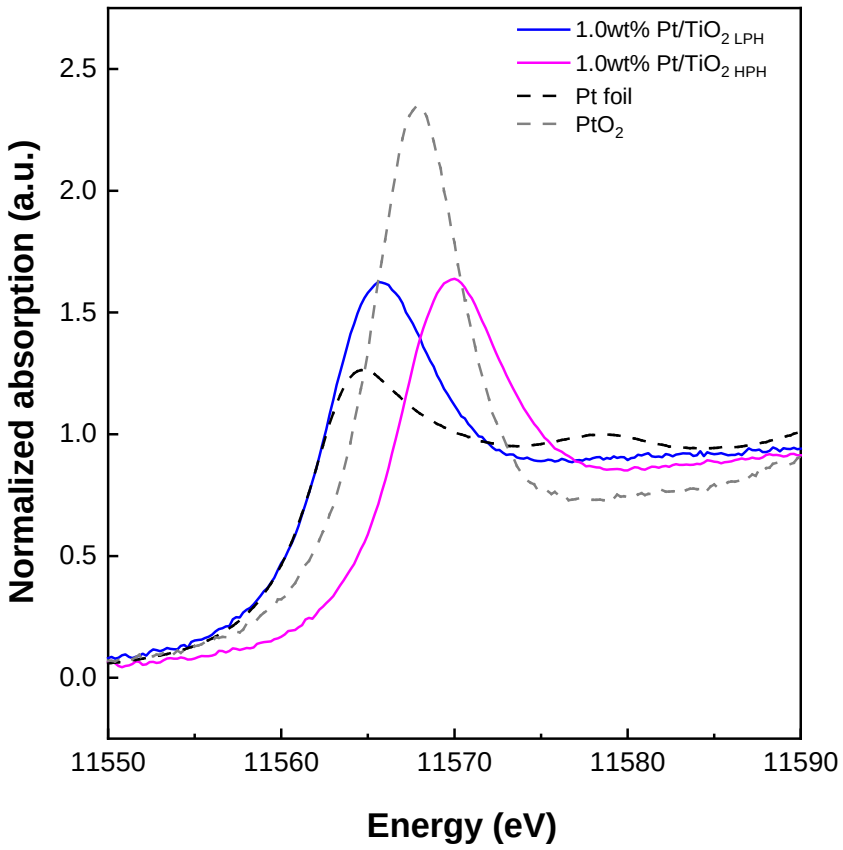

Figure 2.7 XANES of Pt edge of Pt/TiO_2 synthesized under different pH conditions.

2.3.3 Reduction and dispersion of Pt species in Pt/TiO_2 catalysts

H_2-TPR was conducted on Pt/TiO_2 catalysts to investigate the interaction between Pt and TiO_2 support. As Figure 2.8, there were 4 major reduction peaks. In $Pt/TiO_{2\ HPH}$ sample, the first reduction peak located at ~360 K was assigned to the reduction of the surface PtO_x complex to metallic Pt.[81] The second peak at around 604 K was caused by the TiO_2 surface oxygen reduction with the help Pt nanoparticle.[82] The last two peaks at ~790 K and 860 K were related to the reduction of bulk oxygen of TiO_2 lattice with and without the help of Pt respectively. When the pH of impregnation solution increases, the first reduction peak moved to higher temperature (370 K) and the peak intensity decreases. The peak intensity change was caused by lower Pt dispersion, that larger Pt nanoparticles have smaller proportion of surface PtO_x complex. However, it's been reported that larger Pt nanoparticles were easier to reduce,[83] which contradicted with the 10 K shift to higher temperature of PtO_x reduction. Therefore the particle size effect cannot merely explain the changes of this reduction peak. One possible explanation was that the interaction between PtO_x and $TiO_{2\ HPH}$ is stronger than that of $Pt/TiO_{2\ LPH}$. The second reduction peaks of these two samples were at approximately the same position, which suggested that once reduced to Pt metallic nanoparticle, the ability of Pt to dissociatively adsorb H_2 and facilitate the TiO_2 surface reduction are same. The third reduction peak of $Pt/TiO_{2\ HPH}$ has

relatedly higher intensity than the last reduction peak. This could be due to the higher efficiency of activated H migration to the bulk of TiO_2 crystal in $Pt/TiO_{2\ HPH}$ sample.

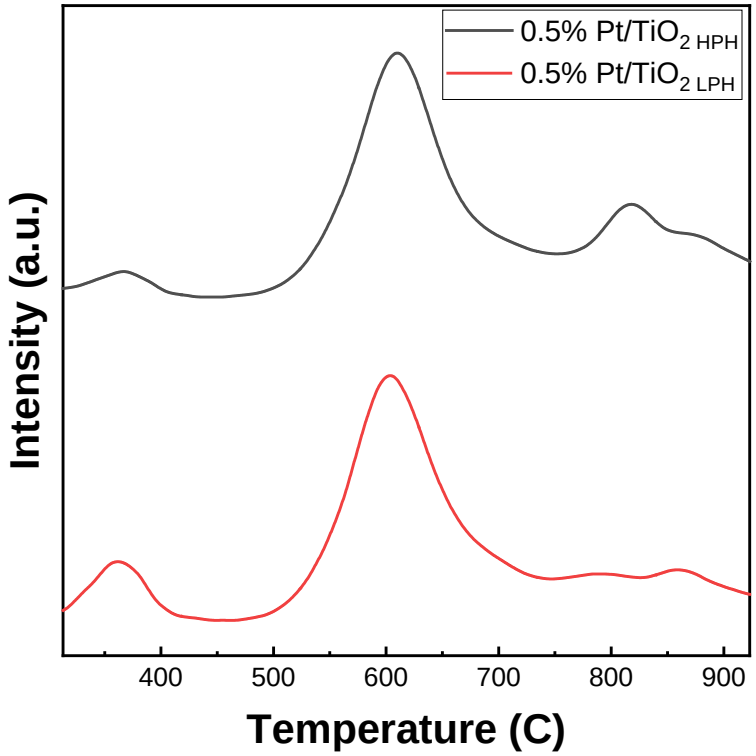

Figure 2.8 H_2-TPR of Pt/TiO_2 synthesized under different pH conditions.

It is typical that the adsorption of small molecules such as H_2 and CO became suppressed when strong metal support interaction occurred on the catalyst sample.[84] The CO chemisorption was used to quantify the Pt species accessible to CO molecules in the Pt/TiO_2 catalysts. The number of exposed Pt atoms and percentages of Pt dispersion (D) were be evaluated with the method discussed in chapter 3. As shown in Table 2.1, the Pt dispersion in $Pt/TiO_{2\ WI}$ was 40.6%, which was lower than that of the

$Pt/TiO_{2\ LPH}$ but higher than the $Pt/TiO_{2\ HPH}$, which was consistent with the trend from STEM particle size analysis of Pt nanoparticle. However, if the difference in calculated Pt dispersion was only cause by different Pt particle size, $Pt/TiO_{2\ LPH}$ should only have ~5% more surface Pt than $Pt/TiO_{2\ HPH}$. Comparing the Pt dispersion of the two samples synthesized by SEA method, the difference in Pt dispersion was ~20% instead of 5%, which indicated that there was other interaction between Pt nanoparticle and support that suppressed the adsorption of CO molecules. This discrepancy between the CO chemisorption and STEM image of Pt nanoparticle on $Pt/TiO_{2\ HPH}$ suggests possible strong metal support interaction between the Pt and TiO_2 support, or partial embedment/encapsulation of Pt by TiO_2.

Table 2.1. The dispersion of Pt in Pt/TiO_2 catalysts determined by CO chemisorption

Sample name	Pt dispersion (%)
$Pt/TiO_{2\ WI}$	40.6%
$Pt/TiO_{2\ LPH}$	55.4%
$Pt/TiO_{2\ HPH}$	35.3%

2.3.4 Styrene hydrogenation over Pt/TiO_2 catalysts synthesized under different pH

As styrene hydrogenation has been established as structure sensitive reaction to discriminate difference in Pt particle sizes on TiO_2 support, the catalytic performance of these three catalysts synthesized under different pH was firstly tested by styrene hydrogenation. The mild reduction pretreatment prior to the catalysis tests was purposely chosen in order to prevent SMSI induced by harsh reduction conditions.[85] The activity differences would be caused by the difference in Pt aggregation state or the strong metal support interaction formed during the synthesis process. As the reaction results shown in Figure 2.9, the TOF of $Pt/TiO_{2\ WI}$ and $Pt/TiO_{2\ LPH}$ were 0.25 and 0.21 mol s^{-1} [mol Pt]$^{-1}$, which were similar to each other. These TOF numbers were in good agreement with the relationship between Pt size and activity developed in chapter 3. However, $Pt/TiO_{2\ HPH}$ catalyst showed TOF of 0.025 mol s^{-1} [mol Pt]$^{-1}$, which was ~10 times lower than that of $Pt/TiO_{2\ LPH}$. This low activity of $Pt/TiO_{2\ HPH}$ sample could not be explained by solely the Pt size difference. As the electronic property characterization by XPS and XANES, the Pt nanoparticle in $Pt/TiO_{2\ HPH}$ was more electron deficient with broadened d band that shifted away from the fermi level. These electronic structure differences were the main reason for the change in adsorption of styrene molecules and subsequently the difference in catalytic activity.

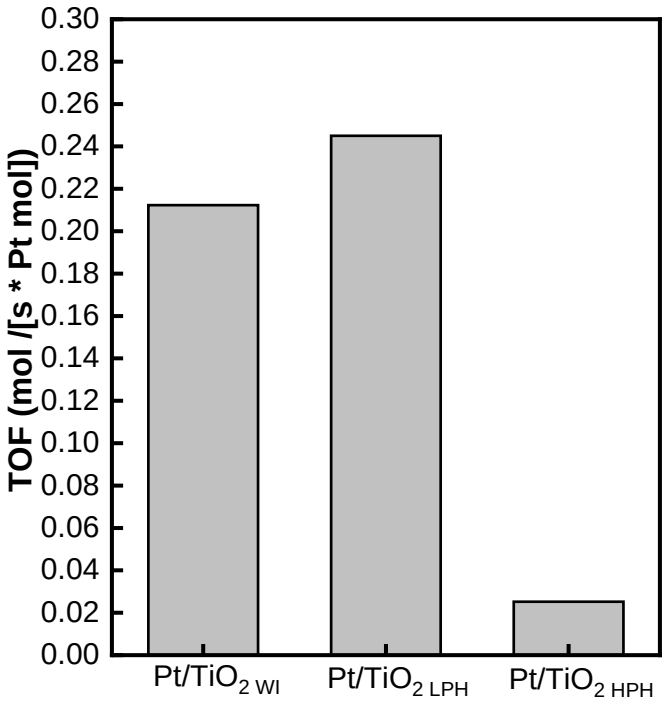

Figure 2.9 styrene hydrogenation performance of Pt/TiO_2 synthesized under different pH conditions.

2.3.5 3-nitrostyrene selective hydrogenation over Pt/TiO_2 catalysts synthesized under different pH

It has been reported by Zhang's group that the 3-nitrostyrene hydrogenation activity and selectivity of Pt/TiO_2 catalyst could be significantly enhanced by the SMSI between Pt single atom and TiO_2.[86] The change was attributed the different adsorption and activation models of substrate.[87] In order to selectively hydrogenation the $-NO_2$ group of the substrate, metal catalyst with engineered structure were needed as the -

C=C group was prone to be hydrogenated and produce 3-ethylnitrobenzene (3ENB) byproduct. If the hydrogenation activity of the active site became too high, the complete hydrogenation byproduct, 3-ethylanillin (3EA), would be produced. To verify the effect of electronic property change of Pt by SMSI, 3-nitrostyrene selective hydrogenation reaction was conducted with the Pt/TiO_2 catalysts prepared under different pH condition. As shown in Figure 2.10, after 90 min of reaction time, $Pt/TiO_{2\ LPH}$ had higher conversion and 3-vinylanillin product selectivity than $Pt/TiO_{2\ WI}$. For $Pt/TiO_{2\ HPH}$ catalyst, since the catalytic activity was too high, at 90 min the 3-nitrostyrene substrate was completely consumed. The reaction was sampled at 30 min instead of 90 min. The $Pt/TiO_{2\ HPH}$ catalyst showed comparable conversion and 3VA selectivity as $Pt/TiO_{2\ LPH}$ with 1/3 of reaction time. This enhancement in catalytic activity was a indication of SMSI between the Pt nanoparticle and TiO_2 support in this catalyst. The SMSI effect changed the electronic property of $Pt/TiO_{2\ HPH}$, causing the Pt species to become more cationic. The cationic Pt sites favored more of the adsorption of $-NO_2$ group and eventually yield a higher catalytic activity.

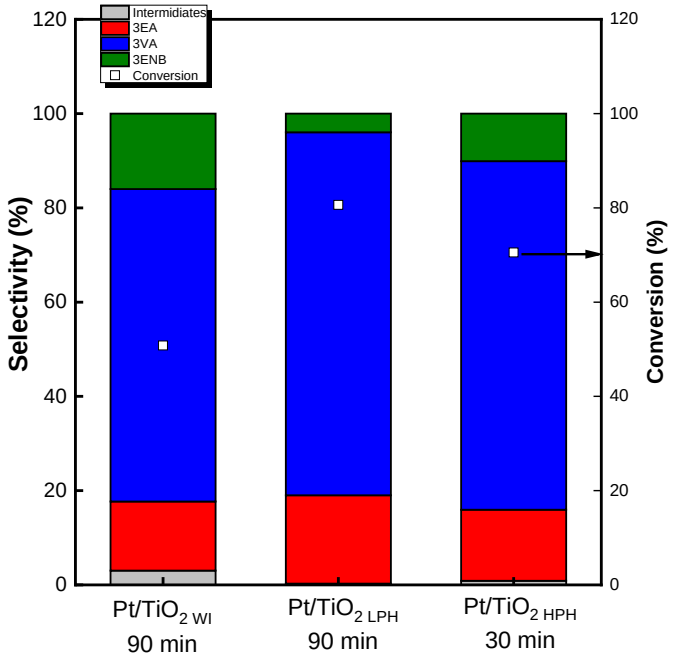

Figure 2.10 3-nitrostyrene hydrogenation performance of Pt/TiO_2 synthesized under different pH conditions.

2.4 Conclusion of Chapter 2

In summary, the Pt/TiO_2 catalysts were prepared by wetness impregnation with solutions of different pH. The effect of solution pH on the textural properties of TiO_2 support were studied firstly by XRD, TEM and N_2 physisorption. It has been found that the basic NH_4OH solution was able to corrode the TiO_2 surface, which effect was more significant as the pH of the NH_4OH solution increase. This surface property change of TiO_2 could cause Pt particle embedment or encapsulation during the SEA synthesis process. The dispersion of loaded Pt under different conditions were studied by STEM imaging and CO chemisorption, which results suggest that SEA synthesis needs to be

conducted under proper pH to increase the Pt dispersion. As the discrepancy between Pt size and CO quantity adsorbed indicated, further increasing the impregnation pH did not continue to decrease Pt particle size, instead it caused strong metal support interaction between Pt and TiO_2 support. The electronic property characterization of the Pt/TiO_2 catalysts showed more cationic Pt property on Pt/$TiO_{2\ HPH}$ catalyst, and changes in the Pt d band structure. This electronic structure change caused the catalytic performance difference of Pt/$TiO_{2\ HPH}$ in the hydrogenation of vinyl and nitro group. The activity of Pt/$TiO_{2\ HPH}$ catalyst in the hydrogenation of polar nitro group has been significantly enhanced. The Pt/$TiO_{2\ HPH}$ sample showed two characteristic phenomena of strong metal support interaction: the suppression of adsorption of CO and charge transfer from metal nanoparticle to support as the characterization results suggested. It could be concluded that the metal support interaction could be tuned by changing the pH of wetness impregnation solution. When the solution causes dissolution of the support material, the metal atoms from precursor solution would locate on the vacancy/cavity site created by corrosive solution, resulting in embedded or encapsulated in the support surface. This resulted metal nanoparticle on support structure would have stronger metal support interaction compared to catalysts impregnated at milder conditions. This study is the first one to propose that the SMSI between metal and support could be tuned without redox interactions. The wet chemistry approach offers an efficient way to enhance the SMSI effect in heterogeneous catalyst.

Chapter 3: Differentiating supported platinum single atoms, clusters and nanoparticles by styrene hydrogenation

3.1 Introduction

Supported noble metal catalysts are extensively used in the petrochemical and pharmaceutical industries to facilitate chemical reaction processes. Due to the natural scarcity and high cost of noble metals, decreasing metal loadings by reducing particle sizes is desired in the heterogeneous catalysis field.[88-90] As a new frontier of this study, single atom catalysts achieving maximized metal dispersion and the potential of atomically-precise active sites are being actively pursued.[19, 20, 91, 92] By transiting the metal active sites from nanoparticles to sub-nanometer clusters and then to single atoms, differences in the degree of metal atom aggregation and coordination structures in supported catalysts exist,[93-95] which can influence their behavior in catalytic reactions. Therefore, it remains a necessity to identify and differentiate these metal sites and their functionalities, as supported metal catalysts often consist of a mixture of nanoparticles, sub-nanometer clusters and/or single atoms.

Advanced characterization techniques have been used to study the geometric and electronic properties of supported metal single atom, cluster and nanoparticle catalysts. For example, high-angle annular dark-field scanning transmission electron microscopy

(HAADF-STEM) detects metal particles down to the limit of atomically dispersed species. The metal atoms with different aggregation behavior and particle sizes within the support can be analyzed from this imaging technique.[35, 96, 97] X-ray absorption spectroscopy (XAS) probes the electronic state as well as coordination environment of metal catalysts.[98] X-ray absorption near-edge structure (XANES) measures the chemical state of elements of interest by measuring changes in absorption characteristics.[99] First - or even second-shell coordination environments of atoms of interest can be obtained with extended X-ray absorption fine structure (EXAFS) spectroscopy.[100] Diffuse reflectance infrared Fourier transform spectroscopy of carbon monoxide (CO) adsorbate (CO-DRIFTS) is another commonly applied characterization technique for supported metal catalysts, which can provide information on local coordination environment, homogeneity, and reactivity of metal active species.[21, 101]

Catalytic reaction testing is a direct strategy used to examine the performances of supported metal catalysts in selected reaction conditions.[44, 102-104] For example, single atom catalysts have high reactivity in CO oxidation[105, 106] and high selectivity in the selective hydrogenation of acetylene groups,[107, 108] while nanoparticles showed opposite trends in both reactions. The metal clusters showed higher reactivity than the nanoparticles in ethylene hydrogenation.[109] However it has also been reported that the co-existence of single atoms and nanoparticles yields the best activity in the hydrogenation of ketones and aldehydes.[110] It should be noted that a systematic comparison of the supported catalysts with a wide range of metal sizes consisting of

nanoparticles, nanometer and sub-nanometer clusters, and single atoms has been rarely reported.

In this chapter, we employed styrene hydrogenation to identify and differentiate the metal sites and their activities in supported catalysts with different metal particle sizes. The exemplary catalysts are titania (TiO_2) supported platinum (Pt) made by a strong electrostatic adsorption (SEA) approach. The average Pt particle sizes were varied from nanoparticles to sub-nanometer clusters and single atoms by decreasing the Pt loadings during the synthesis. With decreasing particle sizes, the Pt atom reactivity in the styrene hydrogenation reaction shows an increasing then decreasing trend, indicating structure sensitivity of the reaction. Together with other characterization techniques including HAADF-STEM, X-ray photoelectron spectroscopy (XPS), XANES, temperature programmed reduction by hydrogen (i.e., H_2-TPR) and chemisorption, the geometric and electronic properties of Pt sites were analyzed. These properties were correlated to the catalytic activity of Pt/TiO_2 catalysts in the styrene hydrogenation reaction. We would like to note that the reaction was performed under ambient condition in a wet lab that is equipped with a fumehood and general glassware apparatus. The simplicity in experimental operation together with the correlations obtained among particle size, geometric/electronic properties and reaction behavior indicates that this process could be used as a general method to pre-screen supported metal catalysts with various particle sizes in other catalyst systems.

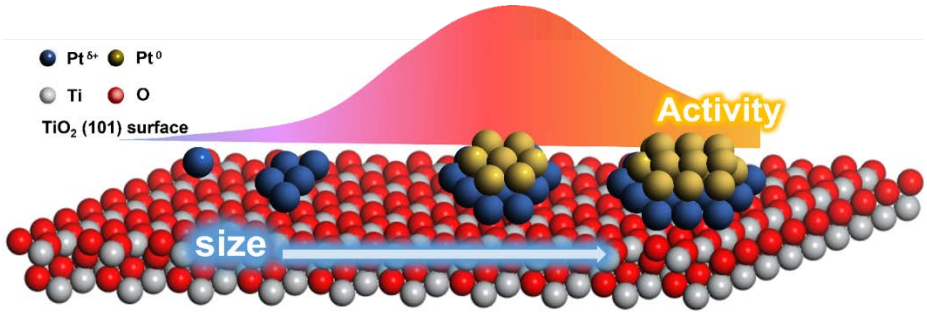

Figure 3.1 Hydrogenation activity of Pt with different aggregation state.

3.2 Experiments

3.2.1 Materials

The titania support (anatase, 99.5% purity) was purchased from U.S. Research Nanomaterial. The Pt precursor, tetraammineplatinum(II) nitrite (TAPN, >99.99% metal basis), was obtained from Alfa Aesar. The ammonia (NH_4OH) solution (28-30 wt.%) were bought from VWR. Styrene (>99.5% purity) stabilized with 10 to 20 ppm 4-tert-butylcatechol was purchased from Acros Organics. Deionized (DI) water was used in the work.

3.2.2 Catalyst preparation

The Pt/TiO_2 catalysts with Pt concentrations ranging from 0.04 wt.% to 5.00 wt.% were prepared using the SEA method[18]. In a typical synthesis, 0.500 g of as-received TiO_2 powder was dispersed in 50.00 mL of diluted NH_4OH solution that was

prepared by mixing 28-30 wt.% NH_4OH and DI water with volume ratio of 1:3. 0.085 g of TAPN was dissolved in 5.00 mL of DI water in a glass vial to form the stock solution. Based on the desired Pt loading in the Pt/TiO_2 catalyst, a certain amount of TAPN stock solution was added into a 25 mL of diluted NH_4OH solution (volume ratio between 28-30 wt.% NH_4OH and DI water = 1:3). The TAPN in NH_4OH solution was then transferred into a syringe and was added into the TiO_2 suspension using a syringe pump (Pump 11, Harvard Apparatus) at a rate of 2 mL/hr. Afterwards, the mixture was placed in a convection oven (VWR Sheldon Manufacturing Model, 1350GM Gravity Convection Oven) that was preheated to 343 K. After the sample had fully dried in the oven, it was calcined at 553 K (ramp rate of 5 K/min) for 4 h in a furnace (Thermo Scientific Lindberg/Blue M™ Multipurpose Box Furnaces). The air (Airgas, research grade) flow rate was kept at 50 mL/min during this calcination step. After the sample cooled down to room temperature, it was transferred into a tubular furnace for reduction at 423 K (ramp rate of 5 K/min) for 2 h. The gas atmosphere consisted of diluted H_2 ($5\%H_2/N_2$ mixture) at a flow rate 100 mL/min. The reduced sample was then stored in a desiccator prior to characterization and reaction tests.

3.2.3 Catalyst characterization

The Pt concentration in each Pt/TiO_2 sample was determined by inductively coupled plasma optical emission spectroscopy (ICP-OES, Galbraith Laboratories). The crystal phase was determined by powder X-Ray diffraction (XRD) patterns recorded using a Bruker D8 Advance Lynx Powder Diffractometer (LynxEye PSD detector,

sealed tube, Cu Kα radiation with Ni β-filter). The morphologies of Pt/TiO_2 catalysts with Pt concentrations of 2.00 wt.%, 4.00 wt.% and 5.00 wt.% were observed by STEM measurement with a Thermo Scientific (FEI) Titan Themis S/TEM operating in probe mode at 200 kV with HAADF detector using gun lens 7 and spot size 7. For all other samples, HAADF-STEM imaging was conducted by a Hitachi HD2700C STEM operated at 200 kV and equipped with a probe aberration corrector (spatial resolution ~1 Å). The coordination status of Pt and Ti atoms in the catalysts was probed using a Versaprobe III by Physical Electronics Inc. (PHI) X-ray photoelectron spectrometer. Powders were deposited on carbon tape for sample immobilization in the chamber. X-rays were generated with a monochromated Al Kα anode at 25 W and a beam size of 100 μm. The chamber pressure during analysis was 5×10^{-6} Pa or less. Surveys were performed with a pass energy of 224 eV for each sample, and higher resolution elemental scans were collected with pass energies of 55 eV; both had take-off angles of 45 degrees. A combination of an electron neutralizer and low energy Ar ion neutralizer was used to mitigate surface charging.

The X-ray absorption fine structure spectroscopy (XAFS) measurements at the Pt L3 edge (~11560 keV) were performed on the Quick X-ray Absorption and Scattering (QAS) beamline at the National Synchrotron Light Source (NSLS) II, Brookhaven National Laboratory. XAFS data were collected in the fluorescence mode under ambient condition using a passivated implanted planar silicon (PIPS) detector. The intensity of the incident beam and the absorption of the Pt reference foil were measured with ionization chambers. Athena (0.9.26) software was used for processing

XAS data. To obtain good signal to noise ratio all spectra was merged with 80 scans. Attenuated total reflection Fourier transform infrared (ATR-FTIR) spectrum of styrene adsorbate in the catalyst was recorded with a spectrophotometer (Thermo Nicolet NEXUS 670) in the range of 500-4000 cm^{-1}. Each sample was measured with 32 scans at an effective resolution of 2 cm^{-1}.

3.2.4 H_2-TPR measurements

Temperature programed reduction of the Pt/TiO_2 catalyst with H_2 reducing gas (H_2-TPR) was carried out on a Quantachrome Autosorb iQ instrument. A thermal conductivity detector (TCD) was used to record the H_2 consumption in the process. Prior to the measurement, each sample was subjected to a pre-treatment with 40 mL/min N_2 flow (Airgas, Research grade) at 553 K for 2 h. After cooled to 323 K, the gas was switched to 40 mL/min $5\%H_2/N_2$ and the sample was heated to 1173 K at 10 K/min ramp rate and kept at the final temperature for 10 min. A cold trap was used to remove water produced throughout each experiment from the outlet stream to avoid interference with the TCD signal.

3.2.5 Pt site quantification by CO chemisorption

The chemisorption of CO molecules on the catalyst was measured by pulse titration in the same equipment as the one used in H_2-TPR. The catalyst was first treated in an Ar flow (50 mL/min) at 553 K for 4 h and then cooled down to 323 K. $5\%H_2/N_2$ at a flow rate of 50 mL min^{-1} was then introduced to reduce the catalyst for 1 h followed

by Ar gas purge for 2 h. Afterwards, the sample was cooled down to 303 K in the Ar flowing gas. A series of CO pulses (50 uL in each pulse) were injected with an interval of 5 min until the amount of exit CO pulses reached a steady state value. The CO signal was recorded using a Prima BT Bench Top Process Mass Spectrometers (Thermo Fisher Scientific, winsford U.K. CW7 3GA).

3.2.6 Styrene hydrogenation reaction test

Styrene hydrogenation was used to test the catalytic activity of synthesized Pt/TiO_2 catalysts. Figure 3.2 shows the experimental setup. In the reaction, 9.00 mL ethanol and 0.050 g catalyst were added into a 50 mL three-neck flask in sequence. The resultant catalyst suspension was sealed in the flask by septa and sonicated for 20 s using an ultrasonic bath (Fisher Scientific FS60). The flask was then placed in a water bath that was preheated to 303 K. A magnetic stirring bar (stirred at 500 rpm) was used to mix the suspension. The center neck of the flask was connected to a condenser. The septum in the right neck was pushed through with a syringe needle to deliver the H_2 gas (50 mL/min, Airgas Ultra High Purity 99.9%) to purge the flask and supply H_2 for the reaction. After purging for 30 min, the styrene solution (0.053 g styrene in 1.00 mL ethanol) was injected into the reactor from the left neck. This moment was recorded as the starting time of the reaction. Reaction mixture was sampled by a syringe equipped with a needle from the left neck of the reactor. After filtering out the solid catalyst particles by syringe filter, the sampled solution was analyzed using a gas

chromatography (Agilent 7890A) equipped with a methylsiloxane capillary column (HP-1, 50.0 m × 320 μm × 0.52 μm) and a flame ionization detector (FID).

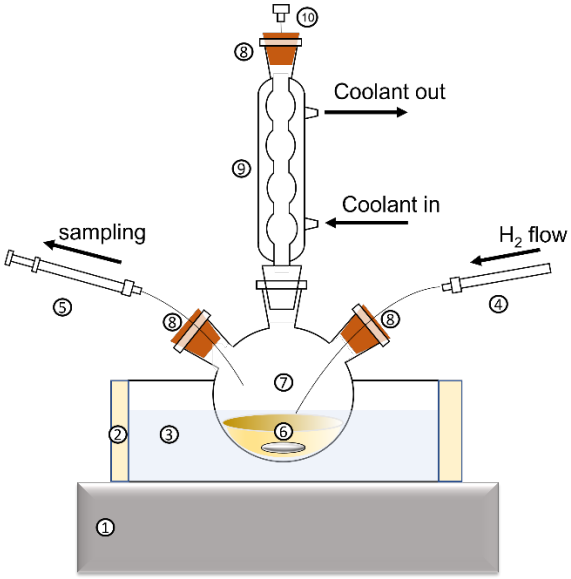

Figure 3.2 Experimental setup for styrene hydrogenation.

(1)Stirring hotplate, (2)Fiberglass insulation, (3)water bath, (4)H_2 inlet port, (5)syringe for sampling, (6)magnetic stir bar, (7)3-neck flask, (8)septum for sealing, (9)condenser, (10)gas outlet.

Under the tested conditions, styrene did not have any conversion in the reactor either in the absence of any catalyst or in the presence of TiO_2 support. The influence of mass transfer limitations on the measured reaction rate data were purposely excluded. Since the catalyst support is nonporous, internal mass transfer limitation is not expected to exist. For the external mass transfer limitation, we eliminated it by running the reaction at high stirring speed. As shown in Figure 3.3a, the conversion increased with increasing the stirring speed when the stirring speed was low. After the

stirring speed was higher than 300 rpm, the conversion was kept constant. All the reaction data presented in the manuscript were collected at 350 rpm, so the external mass transfer limitation was absent. To test the catalyst deactivation, we recycled the catalyst from reaction mixture by centrifugation. Afterwards, the catalyst was dried in a vacuum oven overnight, and then used for the next cycle of reaction test. As shown in Figure 3.3b, the recycled catalyst showed comparable conversions to that of the fresh catalyst, indicating the absence of deactivation in our studied reaction conditions.

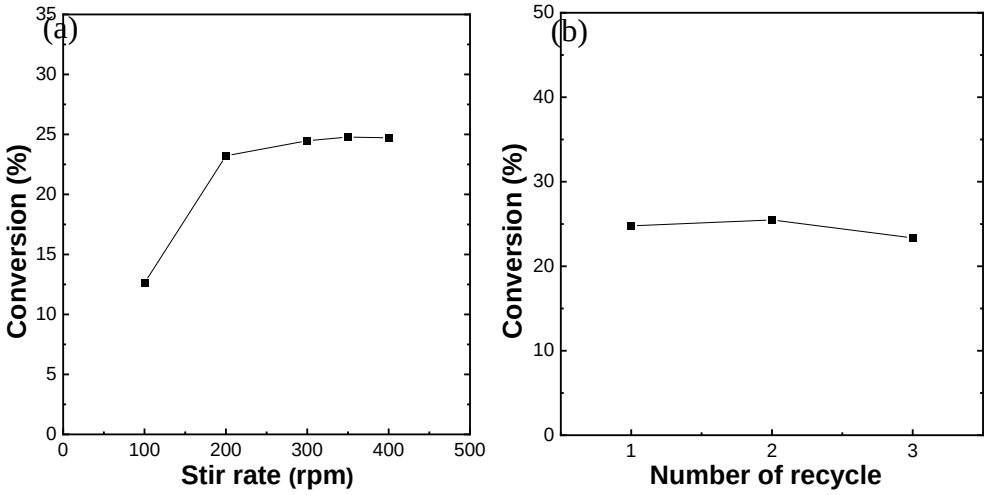

Figure 3.3 (a) conversion versus stir rate; (b) conversion of recycled catalysts at 5 min of reaction time. (1.00 wt.% Pt/TiO_2, 303K, 1 atm pressure, 50 mg catalyst and 0.5 mmol styrene in 10 mL ethanol.)

Eq. 1 was used to calculate the turnover frequency of Pt sites ($TOF_{(Pt)}$, mol s^{-1} [mol Pt]$^{-1}$), where r is the measured reaction rate (mol s^{-1}), N_{Pt} is the quantity of Pt atoms [mol

Pt] in each catalyst, and D is the Pt dispersion determined by the CO chemisorption method.

$$TOF_{(Pt)} = r/(N_{Pt} * D) \quad (3.1)$$

3.3 Results and discussion

3.3.1 Geometric properties of Pt/TiO_2 catalysts with different Pt loadings

The as-prepared Pt on anatase TiO_2 catalysts with Pt concentrations in the range of 0.04 wt.% - 5.00 wt.% were firstly characterized by XRD to understand their crystalline structures. Figure 3.4 shows that the XRD peaks of the TiO_2 support are characteristic of anatase phase (JCPDS #75-1537). After the SEA synthesis process, the TiO_2 support maintained the anatase phase, as confirmed by the identical XRD patterns of Pt/TiO_2 samples as that of the TiO_2 support. The XRD patterns of Pt/TiO_2 with Pt concentrations lower than 2% were not shown, since they are identical to those of the 2.00 wt.% Pt/TiO_2 sample. The diffraction peak associated with Pt species was not observed until the Pt concentration was increased to 4.00 wt.%. As shown in the XRD patterns of 4.00 wt.% and 5.00 wt.% Pt/TiO_2 samples, the peak at $2\theta = 40°$ is assigned to Pt (111) diffraction, suggesting Pt nanoparticles are formed in these two samples. 2θ =39-41° region was zoomed in 5 times to clearly show Pt (111) peak. For all other Pt/TiO_2 samples, the Pt structures are too small to detect in the XRD measurement due to low Pt loading. It should be noted that the elemental composition

analysis from ICP-OES shows that no Pt was lost during the SEA process; the Pt concentration in each sample remains nearly the same as the nominal loading used in the catalyst synthesis process.

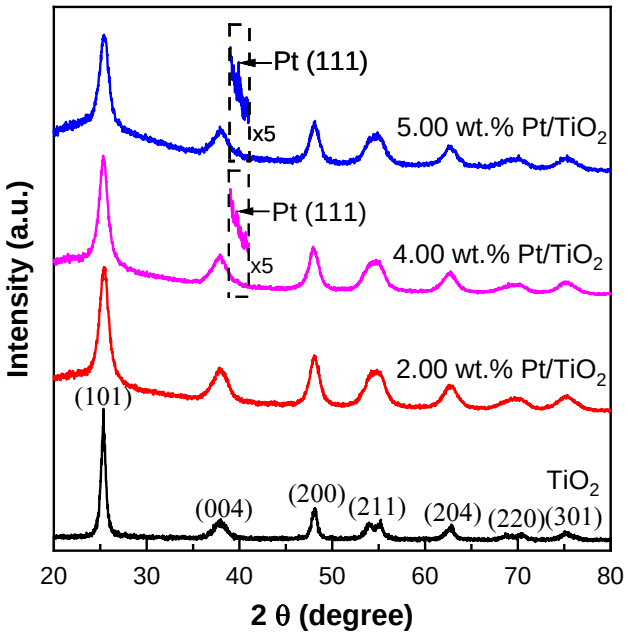

Figure 3.4 XRD patterns of TiO_2 supported Pt metal catalysts with Pt concentrations varied from 2.00-5.00 wt.%. The XRD data of TiO2 support is included for comparison purpose.

To understand geometric properties of the Pt atoms in the TiO_2 support, HAADF-STEM images were collected, with representative images shown in Figure 3.5. For the 0.04 wt.% Pt/TiO_2 sample, Pt stays as single atoms, as reported previously.[21, 111] When the Pt concentration was increased to 0.12 wt.% (Figure 3.5a), single atoms and nanoclusters coexist on the TiO_2 support, but the density of Pt nanoclusters was very low. The continual increase in Pt concentrations to 0.25 wt.% (Figure 3.5b) increased

the density of nanoclusters, but the cluster size did not show any obvious change. In the 0.50 wt.% and 1.00 wt.% Pt/TiO_2 samples (Figures 2.5c-d), more Pt clusters are observed, some with slightly larger sizes, as indicated by the circled regions in the images. The further increase in Pt concentration to 2.00 wt.% (Figure 3.5e) leads to an increase in density of larger Pt clusters, and the sizes of these clusters also increased. We further increased the Pt concentrations to 4.00 wt.% (Figure 3.5f) and 5.00 wt.% (Figure 3.5g), and both samples showed a high density of large Pt clusters, where some are connected to form even larger particles, as indicated by the red arrows in both images.

The Pt particle size distribution histogram of each Pt/TiO_2 sample was analyzed using statistical analysis of the STEM images. Figures 2.6a-g show the particle size data obtained for the samples with Pt concentrations from 0.12 wt.% to 5.00 wt.% in sequence. Due to the resolution cutoff (~0.4 nm) of the STEM instrument, the single atoms and dimers were not included in the size distribution analysis. From direct morphology visualization of the STEM images in Figure 3.5, samples with Pt loadings of 0.12 wt.% and 0.25 wt.% have average sizes of 0.72 and 0.75 nm (Figures 2.6a-b), respectively. The majority of Pt particles are less than 1 nm, which are denoted as sub-nanometer clusters. The increase in Pt loadings to 0.50 and 1.00 wt.% increased the average particle sizes to 1.06 nm and 1.08 nm, respectively, in Figures 2.6c-d. The predominant particle sizes in these two samples are close to one nanometer. We defined them as nanometer clusters. For the samples with even higher Pt loadings (i.e., 2.00 wt.%, 4.00 wt.% and 5.00 wt.% in Figures 2.6e-g), the average particle size increased

monotonically with Pt loadings to 1.28, 1.32 and 1.46 nm in sequence. Most of the Pt atoms in these three samples aggregate into nanoparticles, as the dominant particle sizes are above 1 nanometer.

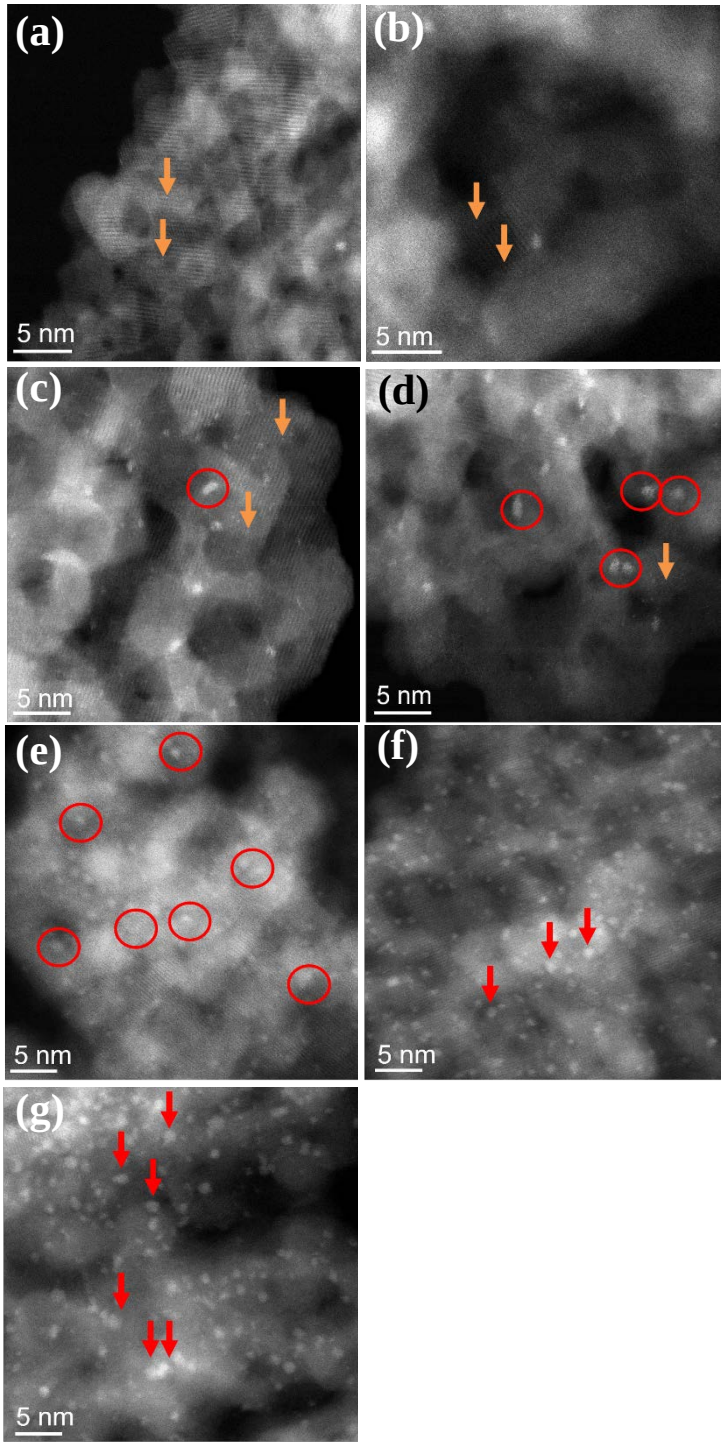
(a)
5 nm
(b)
5 nm
(c)
5 nm
(d)
5 nm
(e)
5 nm
(f)
5 nm
(g)
5 nm

Figure 3.5 HAADF-STEM images of Pt/TiO2 catalysts with Pt concentration of (a) 0.12 wt.%, (b) 0.25 wt.%, (c) 0.50 wt.%, (d) 1.00 wt.%, (e) 2.00 wt.%, (f) 4.00 wt.% and (g) 5.00wt.%, respectively.

Pt single atoms, clusters and nanoparticles are indicated by orange arrow, red circle and red arrow, respectively.

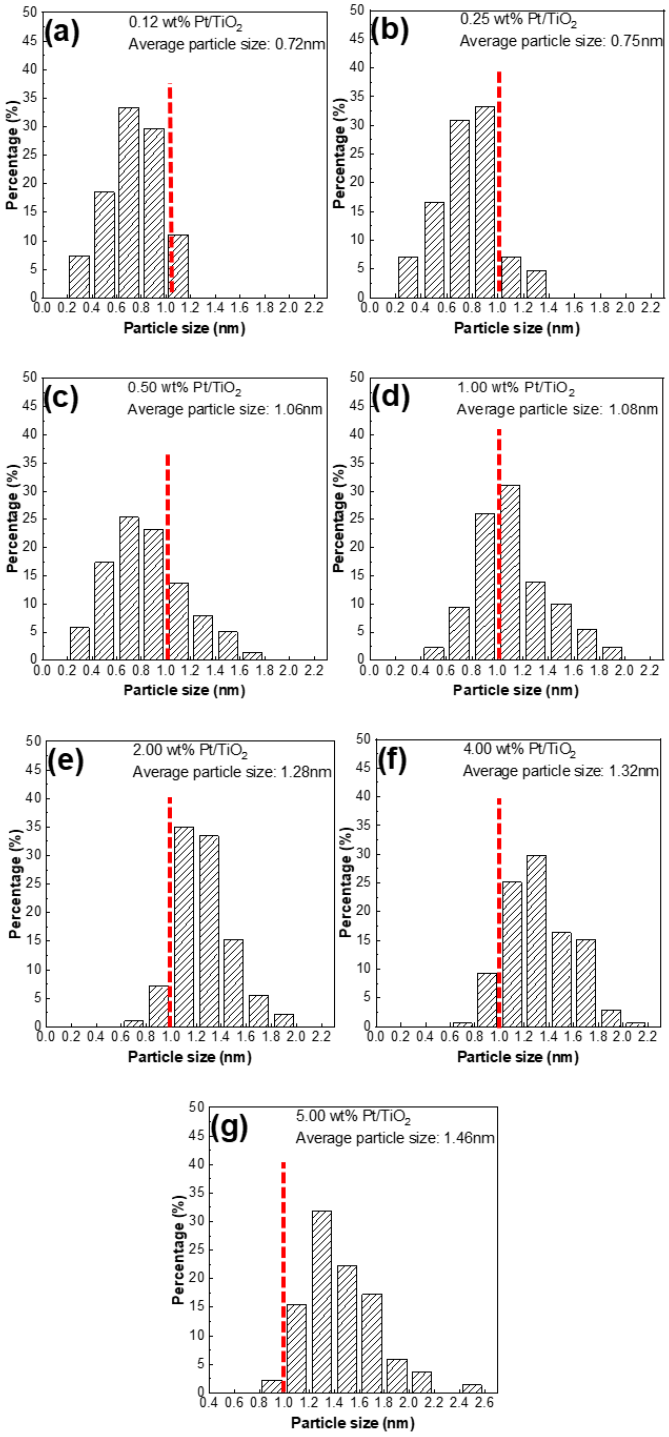

Figure 3.6 Particle size distribution of Pt/TiO_2 catalysts with various Pt concentration of (a) 0.12 wt.%, (b) 0.25 wt.%, (c) 0.50 wt.%, (d) 1.00 wt.%, (e) 2.00 wt.%, (f) 4.00

wt.%, and (g) 5.00 wt.%, respectively. ~50 and ~150 particles were counted in (a)-(b) and (c)-(g) respectively. (The vertical red dash line in each figure is used to guide the particle population centered around 1 nm.)

Table 3.1. Activity analysis of Pt sites in isolate single atoms or aggregated nanoclusters and nanoparticles in Pt/TiO_2 catalysts in styrene hydrogenation reaction.

Catalyst (denoted by Pt loading, wt.%)	**Pt aggregation state** [a]	**Pt concentration ([μmol Pt] g^{-1})** [b]	$f_{Pt\text{-}SA}$ **(%)** [c]	**TOF$_{(Pt)}$ (mol s^{-1} [mol Pt]$^{-1}$)** [d]	**TOF$_{(Pt\text{-}SA)}$ (mol s^{-1} [mol Pt]$^{-1}$)** [e]	**TOF$_{Pt\text{-}x)}$ (mol s^{-1} [mol Pt]$^{-1}$)** [f]
0.04	single atom	2.05	100.0	0.0056	0.0056	-
0.12	subnanometer cluster	6.15	70.5	0.023	0.0056	0.0636
0.25		12.8	65.7	0.020	0.0056	0.0480
0.50	nanometer cluster	25.6	11.7	0.267	0.0056	0.302
1.00		51.3	2.9	0.460	0.0056	0.474
2.00	nanoparticle	103	0.0	0.446	-	0.446
4.00		205	0.0	0.364	-	0.364
5.00		256	0.0	0.290	-	0.290

[a] *Defined from particle histogram data in Figure 3;* [b] *Calculated from Pt loading in each sample;* [c] *Calculated by ratio of single atom quantity to Pt loading quantity;* [d] *Calculated from Eq. (2.1);* [e] *Evaluated from 0.04 wt.% Pt/TiO_2 and applied to other catalysts that contain both Pt single atoms and aggregates;* [f] *Calculated from Eq. (2) by assuming the catalyst contains a mixture of Pt single atoms and Pt single-form aggregates.*

The quantity of Pt atoms in the states of single atoms, sub-nanometer clusters, nanometer clusters and nanoparticles in the Pt/TiO_2 samples were further evaluated from the particle size histograms and total Pt loadings (refer to Section 2.3.2 for details). Table 3.1 summarizes the calculated results. Due to strong metal-support interaction (SMSI) between Pt and TiO_2 support,[86] Pt clusters adapt different geometry than the typical hexagonal close-packed cluster on the TiO_2 surface.[43, 112] In fact, the structure of sub-nanometer and nanometer Pt clusters was assumed to be planar, as reported previously.[111, 113] In this work, the geometry of Pt clusters is calculated based on the work from Zhou et al,[114] in which Pt atoms stay as raft-like, 2-dimensional islands instead of 3-dimensional clusters. For Pt nanoparticles (i.e., larger than 1 nm), Pt reveals a more metallic property, therefore the prediction of Pt nanoparticles with half-octahedrons from Teo at al[115] was adapted. The deduction of Pt atom quantities in the Pt clusters and nanoparticles from the total Pt loading provided the quantity of Pt single atoms. The percentage of Pt single atoms decreases with increasing Pt loading in the Pt/TiO_2 samples. When Pt content is lower than 0.50 wt.%, majority of Pt atoms stay as isolated single atoms. In 0.50 wt.% and 1.00 wt.% Pt/TiO_2 samples, a small percentage of Pt single atoms co-exist with nanometer clusters. In the samples with Pt content above 1.00 wt.%, nearly all Pt atoms agglomerate into clusters and nanoparticles.

3.3.2. Calculation for Pt quantity in isolated single atom state or aggregate state by STEM image analysis

The Pt atom quantities in single atom and aggregate states in each Pt/TiO_2 sample were analyzed on the basis of the composition and geometry of Pt and TiO_2 components. Three steps were used to obtain the results in Table 3.2 below.

(1) Overall Pt density on TiO_2 particle:

From TEM images of TiO_2 support, TiO_2 particles can be assumed to have the spherical geometry with an approximate diameter (d) of 6.60 nm. The cross-sectional area (S_{TiO2}) of TiO_2 particle is calculated to be 34.19 nm2 from Eq. (3.2) below. The volume of each TiO2 particle is 150 nm3 by assuming the density of TiO_2 is 3.9 g cm-3 from Eq. (3.3) If we use 1g sample basis, the number of TiO2 particle (N_{TiO2}) is evaluated by Eq. (3.4). From the loading in each sample, the number of Pt atoms (N_{Pt}) is calculated by Eq. (3.5). The density of Pt atoms (D_{Pt}) on each TiO_2 particle is calculated by Eq. (3.6). Table 3.2 shows the calculation results for each catalyst.

$$S_{TiO_2} = \pi\left(\frac{d}{2}\right)^2 = \pi\left(\frac{6.60\ nm}{2}\right)^2 = 34.19\ nm^2 \qquad (3.2)$$

$$V_{TiO_2} = \frac{4}{3}\pi\left(\frac{d}{2}\right)^3 = \frac{4}{3}\pi\left(\frac{6.60\ nm}{2}\right)^3 = 150\ nm^3 \qquad (3.3)$$

$$N_{TiO2} = \frac{1g*(1-wt.\%Pt)}{V_{TiO2}*3.90\ (\frac{g}{cm^3})} \qquad (3.4)$$

$$N_{Pt} = \frac{1g*\ wt.\%Pt}{195.08\left(\frac{g}{mol}\right)} * N_A \qquad (3.5)$$

$$D_{Pt} = \frac{N_{Pt}}{N_{TiO2}} \qquad (3.6)$$

Table 3.2. Analysis for overall Pt and TiO_2 in 1g catalyst basis.

Catalyst (denoted by Pt loadings, wt.%)	N_{TiO2}	N_{Pt}	D_{Pt}
0.12	$1.71*10^{18}$	$3.70*10^{18}$	2.17
0.25	$1.71*10^{18}$	$7.71*10^{18}$	6.33
0.50	$1.71*10^{18}$	$1.54*10^{19}$	9.04
1.00	$1.71*10^{18}$	$3.08*10^{19}$	18.08
2.00	$1.71*10^{18}$	$6.17*10^{19}$	36.16
4.00	$1.71*10^{18}$	$1.23*10^{20}$	72.32
5.00	$1.71*10^{18}$	$1.54*10^{20}$	90.40

(2) Visible Pt density on TiO_2 particle:

The visible Pt density on the TiO_2 particle was evaluated from the STEM image. The image shows the morphology of both Pt and TiO_2 particles. We select the area that is representative of all STEM images to do Pt and TiO_2 particle density analysis. The size of Pt particles was measured first, and this gave the particle size distribution data in Figure 3.6. From reports in literature,1-2 the number of aggregated Pt atoms of each size is found and included in Table 3.3 below. The Pt atoms in the aggregated states (i.e., sub-nanometer cluster, nanometer cluster and nanoparticle) are obtained by Eq. (3.7).

$$N_{Pt\ atom\ aggr}=\sum_{0.2nm}^{2.6nm}(2^{nd}\,column\ entry\ in\ Table\ S4)*\%\ of\ aggregated\ Pt\ particles\ in\ each\ size \quad (3.7)$$

In the same selected area in the STEM image, the number of TiO_2 particles were estimated by Eq. (3.8).

$$N_{TiO2\text{-}vis}=\frac{Selected\ area\ in\ STEM\ area}{S_{TiO2}}*3 \quad (3.8)$$

where $N_{TiO2\text{-}vis}$ is the TiO_2 particle in the visualized region, S_{TiO2} is the cross-section area of each TiO_2 particle, "3" denotes for the assumption that Pt species on 3 layers of TiO_2 particles close to the imaging plane could be visualized.

Number of Pt clusters ($N_{Pt\ cluster}$) in specific area were counted, and then the number of Pt in cluster in that area was calculated by Eq. (3.9).

$$N_{Pt\text{-}vis}=N_{Pt\ cluster}*N_{Pt\ atom\ aggr} \quad (3.9)$$

Then the number of Pt atoms in that visualized area could be calculated by Eq. (2.10).

$$N_{total\ Pt}=D_{Pt}*N_{TiO_2} \quad (3.10)$$

Table 3.3. Pt atom distribution in Pt/TiO_2 catalysts with different Pt loadings.

Property of Pt/TiO_2 catalyst			Pt quantity in each aggregate category ([mol Pt] g^{-1} catalyst)							
Particle size range (nm)	Atom # in each range	Surface atom # in each range	Pt/TiO_2 samples (denoted by Pt loading, wt.%)							
			0.04	0.12	0.25	0.50	1.00	2.00	4.00	5.00
0-0.2	1	1	2.05	4.33	8.43	2.99	1.47 [a]	-	-	-
0.2-0.4	3 [b]	3 [b]	-	0.0169	0.0342	0.0952	0.0195	-	-	-
0.4-0.6	7	7	-	0.0983	0.186	0.629	0.228	-	-	-
0.6-0.8	10	9	-	0.253	0.495	1.32	0.521	0.0871	0.152	-
0.8-1.0	37	33	-	0.831	1.97	4.50	6.02	2.26	5.07	1.10
1.0-1.2	73 [c]	51 [c]	-	0.615	0.833	5.40	12.83	22.2	27.8	16.2
1.2-1.4	115	73	-	-	0.875	4.86	16.47	33.0	52.5	54.6
1.4-1.6	172	99	-	-	-	4.55	8.958	22.5	41.9	56.1
1.6-1.8	244	129	-	-	-	1.29	4.765	12.7	55.7	61.5
1.8-2.0	335	163	-	-	-	-	-	5.83	15.3	29.8
2.0-2.2	445	201	-	-	-	-	-	3.88	6.77	26.4
2.2-2.4	578	243	-	-	-	-	-	-	-	-
2.4-2.6	725	289	-	-	-	-	-	-	-	10.7
Pt aggregate state			Single atom	sub-nanometer cluster		Nanometer cluster		nanoparticle		

[a] Obtained by deduction of Pt atoms in categories of sub-nanometer Pt cluster, nanometer Pt cluster and Pt nanoparticle from total Pt atoms in each sample; [b] Based on DFT calculation of Pt cluster on anatase TiO_2; [c] Based on the number of atoms in half-octahedron configuration.

(3) Invisible Pt on TiO_2 particle:

From steps (1) and (2), the invisible Pt atoms in TiO_2 particle can be calculated, which is the difference between overall (Ntotal Pt) and visible (NPt-vis) densities. Invisible Pt atoms are assumed to stay in the isolated single atom state. The percentage of Pt single atom in that samples is then obtained, as shown in Table 3.1. The rest of Pt

particles were categorized as sub-nanometer clusters, nanometer clusters, or nanoparticles, depending on the size histogram in Figure 3.6.

3.3.3 Electronic properties of Pt/TiO_2 catalysts with different Pt loadings

XPS measurements were performed to study the electronic properties of TiO_2 supported Pt catalysts. In the XPS spectra, the Ti3s line has a satellite peak present in the 70-80 eV binding energy range, overlapping with the Pt 4f XPS spectra, which should be subtracted to obtain precise Pt4f peaks.[116] For this purpose, the XPS spectrum of pure TiO_2 support was recorded under the same measurement conditions. After the intensity of the background line is normalized by the Ti3s line recorded for the Pt/TiO_2 catalysts and pure TiO_2 support, we subtracted the contribution of the lines from the TiO_2 support within the Pt4f XPS peak region in our analysis. Figure 3.7 shows the XPS spectra of Pt 4f regions scanned for Pt loading from 0.12 wt.% to 5.00 wt.%. The Pt $4f_{7/2}$ peak shifts from 72.53 eV of 0.12 wt.% Pt/TiO_2 sample to 71.07 eV for the 5.00 wt.% sample, which predominately contains Pt nanoparticles. The peak shift to lower binding energy is attributed to the size and bond geometry change of Pt aggregates on the TiO_2 support. Due to the charge transfer to the support, isolated Pt single atoms on metal oxide have been reported to be cationic.[20] Similarly, small Pt clusters appear to be electron deficient because of the intimate interaction between their two-dimensional flat structure and the support.[113, 117]With increasing Pt concentrations, Pt atoms start to form three-dimensional structures[118] where the top layer does not have direct

interaction with support. Therefore, the sample shows metallic Pt properties. With increasing Pt loadings in Pt/TiO_2 samples, the Pt aggregate sizes increase as confirmed by geometric properties in Figures 2.5 and 2.6 above, and thus the Pt species transitions from cationic into metallic species.

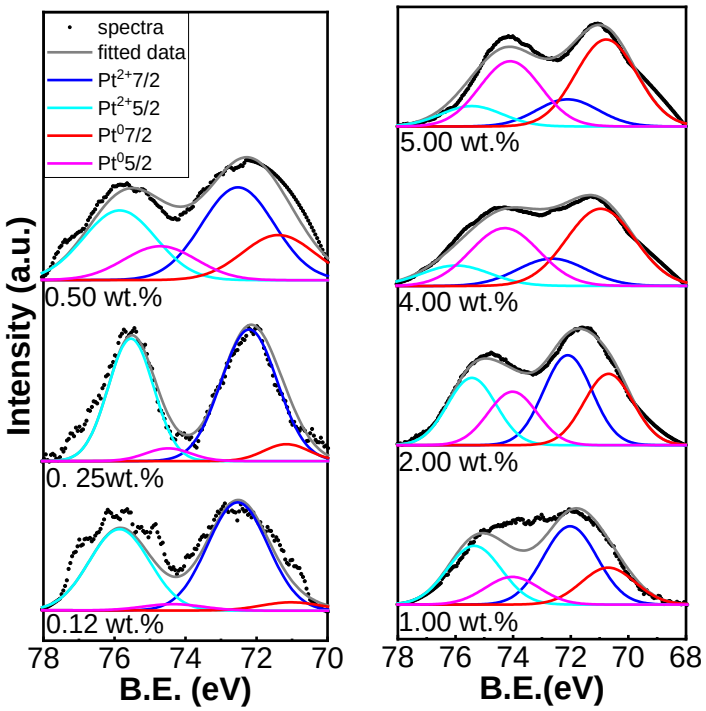

Figure 3.7 XPS spectra of Pt 4f of Pt/TiO_2 samples with Pt concentration in the range of 0.04 wt.%-5.00 wt.%.

The spectra were calibrated with O1s of anatase TiO_2 at 530.0 eV.

A quantitative analysis of cationic and metallic Pt sites in each Pt/TiO_2 sample was attempted by deconvoluting the Pt $4f_{7/2}$ spectrum into Pt^{2+} and Pt^0 peaks (details enclosed in Section S2.3). The peak area ratio of each deconvoluted peak based on the

total area of both peaks is used to indicate the relative quantity of cationic Pt species. As summarized in Table 3.4, the Pt^{2+} percentage decreases from 100% in the 0.04 wt.% Pt/TiO_2 sample that contains solely isolated Pt single atoms to 23.78% in the 5.00 wt.% Pt/TiO_2 sample.

Table 3.4. Peak areas of deconvoluted Pt 4f region.

Catalyst (denoted by Pt loadings, wt.%)	Peak area of Pt 4f region								Pt^{2+} (%)[b]
	$4f_{7/2}$ Pt^{2+}		$4f_{7/2}$ Pt^0		$4f_{5/2}$ Pt^{2+}		$4f_{5/2}$ Pt^0		
	position (eV)	area	position (eV)	area	position (eV)	area	position (eV)	area	
0.12	72.53	38.52	71.02	3.00	75.86	28.89	74.35	2.25	92.77
0.25	72.21	43.57	71.16	4.51	75.54	32.67	74.49	3.38	90.62
0.50	72.52	65.98	71.38	32.10	75.85	49.49	74.71	24.07	67.27
1.00	72.02	68.04	70.70	33.55	75.35	51.03	74.03	25.16	66.97
2.00	72.10	178.14	70.69	142.94	75.43	133.61	74.02	107.20	55.48
4.00	72.65	102.03	70.96	288.34	75.98	76.52	74.29	216.25	26.14
5.00	72.11	45.30	70.77	145.17	75.44	33.97	74.10	108.87	23.78

[a] Spectra was fitted with gaussian peaks, the peak areas shown were integrated by XPSPEAK 41 software; [b] calculated by the ratio of peak area of $4f_{7/2}$ Pt^{2+} to the sum of $4f_{7/2}$ Pt^{2+} and $4f_{7/2}$ Pt^{0}.

Deconvolution of Pt 4f XPS spectra of Pt/TiO_2 catalysts were done by using XPSPEAK 41. The Pt 4f region was deconvoluted into $4f_{7/2}$ Pt^{2+} (72.2 eV) and $4f_{7/2}$ Pt^{0} (71.1 eV), $4f_{5/2}$ Pt^{2+} (75.5 eV) and $4f_{5/2}$ Pt^{0} (74.4 eV), and Ti 3s (75.75 eV) peaks. The full width half maximum (FWHM) of all deconvoluted peaks were kept the same. The relative peak intensity is shown in Table S2. The quantity of cationic Pt in each sample is indicated by the percentage of $4f_{7/2}$ Pt^{2+} among all $4f_{7/2}$ Pt peaks.

Ex-situ XANES characterization on pre-reduced sample in Figure 3.8 also confirmed this conclusion. The oxidation state of Pt metal can be quantitively represented by white line intensity.[37] The overall oxidation state of TiO_2 supported Pt samples lies in between the Pt foil ($Pt_{(0)}$) and PtO_2 ($Pt_{(IV)}$) references. The white line intensity drops with increasing Pt loading from 0.25 wt.% to 1.00 wt.%, which indicates the overall oxidation state of Pt species decreases with increasing particle size.

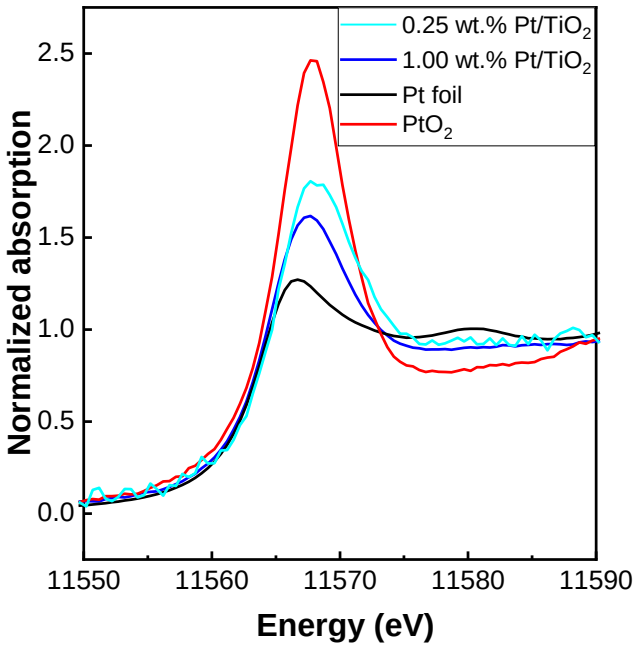

Figure 3.8 XANES spectra of 0.25 wt.% and 1.00 wt.% Pt/TiO_2 samples. The XANES spectra of Pt foil and PtO2 are included as reference.

3.3.4 Reduction and dispersion of Pt species in Pt/TiO_2 catalysts

To study the reducibility of Pt at different aggregate sizes on TiO_2 support, H_2-TPR was carried out on the Pt/TiO_2 samples with Pt concentration was varied from 0.04 to 5.00 wt.%. As shown in Figure 3.9a, three major H_2-TPR peaks centered at different temperatures were observed in each sample. The first peak located at ~400 K is associated with the reduction of the PtO_x complex to metallic Pt.[81, 119] The second H_2 consumption peak at ~640 K appears as the largest one among these three peaks, which can be ascribed to the reduction of TiO_2 surface oxygen facilitated by activated

hydrogen spillover from Pt,[82, 120] while the last one at ~940 K is due to the reduction of bulk oxygen of the TiO_2 support.[121] The position of the first reduction peak shifts to lower temperatures with increased Pt loadings in the catalysts, which should be caused by the different Pt aggregation state. For example, the reduction of Pt single atoms in the 0.04 wt.% Pt/TiO_2 sample happened at ~435 K. This reduction peak shifted to ~410 K for Pt sub-nanometer clusters in 0.12 and 0.25 wt.% Pt/TiO_2, ~400 K for Pt nanometer clusters in 0.50 and 1.00 wt.% Pt/TiO_2, and then ~360 K for Pt nanoparticles in Pt/TiO_2 catalysts with loadings above 1.00 wt.%. The stronger interaction between Pt single atoms and the support adds difficulty on H_2 activation on single atoms, and thus shifts the peak to slightly higher reduction temperature. The intensity of this low temperature H_2-TPR peak increases with increasing Pt content in these Pt/TiO_2 samples.

The chemisorption of CO molecules was used to measure the Pt species accessible to reactants in the Pt/TiO_2 catalysts. By assuming one CO molecule adsorbs onto one Pt site[122], the number of exposed Pt atoms on the catalyst samples and percentages of Pt dispersion (D) can be evaluated. As shown in Figure 3.9b, the Pt dispersion in 0.04 wt.% Pt/TiO_2 is nearly 100%, consistent with the atomically dispersed nature of single atoms. The Pt dispersion on 0.12 wt.% and 0.25 wt.% Pt/TiO_2 samples are 72% and 74%, respectively. When Pt loading was increased to 0.50 wt.%, the dispersion dropped to 58%. As a further increase in Pt loading from 1.00 wt.%, 2.00 wt.%, 4.00 wt.% to 5.00 wt.%, the dispersion decreased to 38%, 30%, 28% and 22%

in sequence. The CO-chemisorption data indicates different degree of accessibility of Pt sites on Pt/TiO_2 catalysts with different Pt loadings.

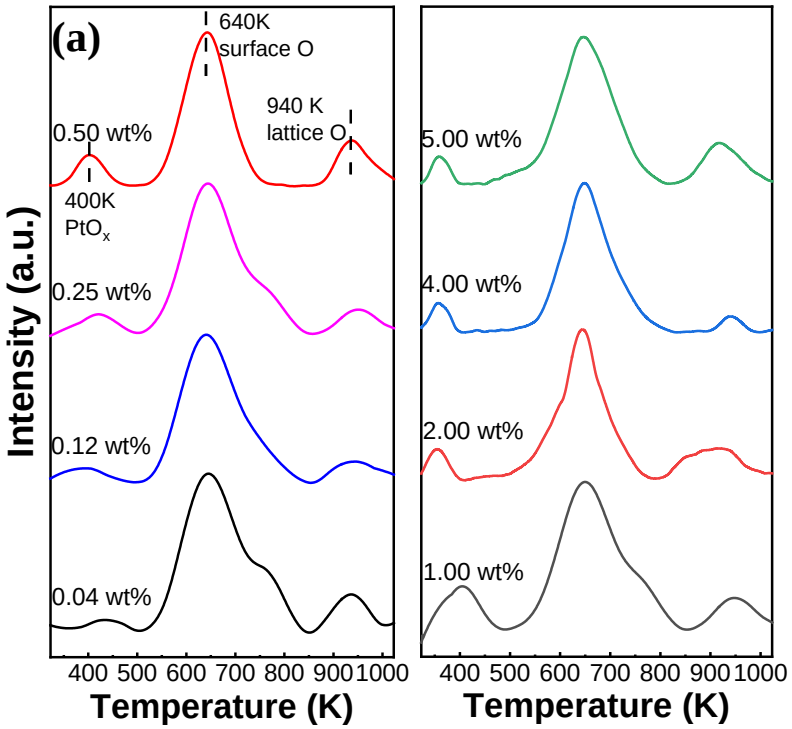

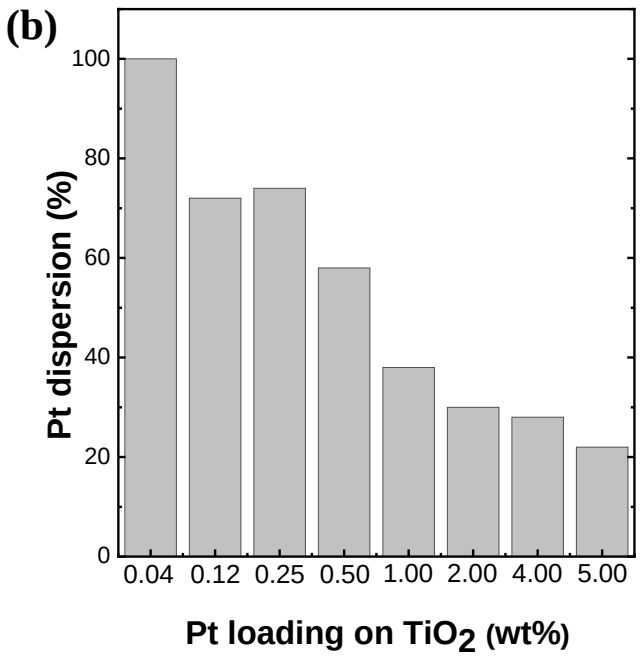

Figure 3.9 H_2-TPR profiles (a) and Pt dispersion (b) of Pt/TiO_2 catalysts with various Pt concentrations (0.04 wt.%-1.00 wt.%).

3.3.5 Styrene hydrogenation over Pt/TiO_2 catalysts with different Pt loadings

As a structure sensitive reaction, styrene hydrogenation has been used to discriminate carbon supported metal catalysts with sub-nanometer sizes.[123, 124] In this study, we used this reaction to study metal oxide (i.e., TiO_2) supported Pt species with sizes spanning from single atoms, clusters and nanoparticles. We would like to note that all the catalysts were calcined at 553 K in an air flow followed by reduction at 523 K in 5% H_2/N_2 flow prior to the catalysis tests. The effect of SMSI causing

encapsulation of Pt species was not expected to influence the catalytic measurements, because SMSI overlayer formation happens at harsher reduction conditions than those explored here, such as ~673 K for metal particles[85] and ~873 K for single atoms[86, 125]. All the activity differences measured in the reaction should be directly correlated to the Pt aggregation state that resulted from the SEA synthesis.

Figure 3.10a shows the styrene conversions over all the Pt/TiO_2 samples. The increase in Pt content in the catalysts led to a monotonic increase in styrene conversion. The Pt single atom catalyst (0.04 wt.% Pt/TiO_2) had a conversion of ~0.04%, while the Pt nanoparticles in 5.00 wt.% Pt/TiO_2 reached 42.0% conversion. The turnover frequencies (TOF) of these catalysts were extracted from reaction data that the styrene conversion was controlled below 20%. The TOF of these catalysts showed a volcano-shaped trend (Figure 3.10b). The 1.00 wt.% Pt/TiO2 showed the peak reactivity, in comparison to the samples that have lower or higher Pt concentrations. In particular, 0.04 wt.% Pt/TiO_2 sample has a TOF of 5.60 mmol s^{-1} [mol Pt]$^{-1}$, ~82-fold lower than that of 1.00 wt.% Pt/TiO_2. When Pt loadings were increased to 0.12 and 0.25 wt.%, the TOFs were, respectively, increased to 23.09 and 19.73 mmol s^{-1} [mol Pt]$^{-1}$. A significant increase in TOF was observed for the 0.50 wt.% Pt/TiO_2 sample, reaching 266.75 mmol s^{-1} [mol Pt]$^{-1}$. Above 1.00 wt.% Pt loadings, the TOF decreases slowly with increasing Pt content in the Pt/TiO_2 samples. The reactivity of Pt atoms in the catalysts follow the order of nanometer clusters > nanoparticle > sub-nanometer clusters > single atoms. We would like to note that ethylbenzene was the only observed product in the reaction. Therefore, the measured TOFs were solely attributed to the

hydrogenation activity of the Pt active sites in the catalysts. We would like to note that ethylbenzene was the only observed product in the reaction. Therefore, the measured TOFs were solely attributed to the hydrogenation activity of the Pt active sites in the catalysts.

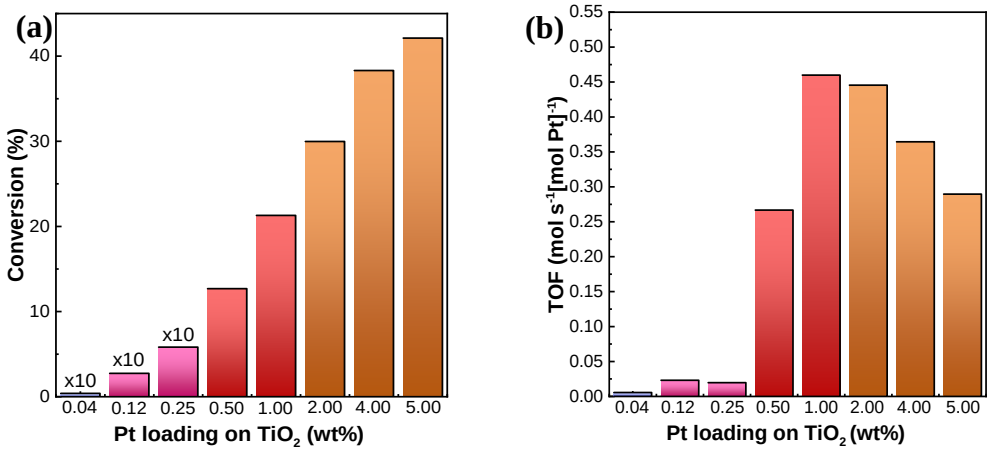

Figure 3.10 Styrene conversion (a), TOF of active Pt atoms (b), and TOF of Pt aggregates in styrene hydrogenation over Pt/TiO_2 catalysts with various Pt concentrations (0.04 wt.%-5.00 wt.%). (reaction condition: 303K, 1 atm pressure, 50 mg catalyst and 0.5 mmol styrene in 10 mL ethanol.)

The activity of each category of Pt aggregates (i.e., single atom, sub-nanometer cluster, nanometer cluster and nanoparticle) in the Pt/TiO_2 catalysts was further analyzed by referring to the quantity of isolated Pt atoms and aggregated atoms (Table 3.1), and the measured overall TOFs in the catalysts. Eq. (3.11) below was used for the calculation,

$$r = TOF_{(SA)} * N_{Pt-SA} + TOF_{(x)} * N_{(Pt-x)} \quad (3.11)$$

where r is the measured reaction rate (mol s^{-1}), $TOF_{(SA)}$ is the turnover frequency (mol s^{-1} [mol Pt]$^{-1}$) of Pt single atoms, $N_{Pt\text{-}SA}$ is the quantity of Pt single atoms ([mol Pt] g^{-1}) obtained from the product of percentage of single atoms ($f_{Pt\text{-}SA}$) and catalyst usage quantity (g), $TOF_{(x)}$ is the turnover frequency (mol s^{-1} [mol Pt]$^{-1}$) of Pt atoms in the aggregates (i.e., clusters or nanoparticles), and $N_{Pt\text{-}x}$ is the quantity of active Pt atoms (mol g^{-1}) in these aggregates and calculated by the multiplication of (1- $f_{Pt\text{-}SA}$), catalyst quantity (g) and Pt dispersion (D). For sub-nanometer clusters, nanometer clusters and nanoparticles, "x" is denoted by "sub-C", "nano-C" and "NP", respectively. The reactivity of Pt single atoms was obtained from 0.04 wt.% Pt/TiO_2 samples that were prepared by our group as well as in the Christopher[18] and Vlachos[29] groups. These samples have been characterized to exclusively contain Pt single atoms. In 0.12 wt.% and 0.25 wt.% Pt/TiO_2 samples, Pt single atoms and sub-nanometer clusters coexist. Under the assumption that Pt sites in each category of Pt atom aggregates independently contribute to the reaction, the sub-nanometer Pt clusters have the reactivity of 55.8 mmol s^{-1} [mol Pt]$^{-1}$, ~10 times higher than the Pt single atoms. Similar calculations by using Eq. (2) were conducted to solve for the reactivity of nanometer Pt clusters in 0.50 wt.% and 1.00 wt.% Pt/TiO_2 samples, which showed TOF of 302 and 474 mmol s^{-1} [mol Pt]$^{-1}$ respectively. The Pt nanoparticles in 2.00 wt.%, 4.00 wt.% and 5.00 wt.% Pt/TiO_2 catalysts had the TOFs of 446, 364, and 290 mmol s^{-1} [mol Pt]$^{-1}$ in sequence in the reaction. The TOF of Pt single atoms is ~87 fold lower than that of the nanometer clusters.

Hydrogenation of unsaturated bonds in olefins has been traditionally categorized as a structurally-insensitive reaction because the reactivity does not change with metal particle sizes in the typical range of 1.5 nm – 10 nm.[109, 126-128] The advent of new catalyst synthesis techniques that produce metal catalysts with sizes of < 1.0 nm recently challenged this conception. For example, the carbon nanotube supported Pt catalysts prepared by atomic layer deposition (ALD) showed that the metal reactivity in styrene hydrogenation changes with Pt particle sizes prepared from different ALD cycles.[44] Similarly, the Pt clusters prepared from the platinum thiolate complexes on Ketjenblack support showed the clusters containing 10 Pt atoms had the maximum reactivity in styrene hydrogenation.[43] A surface science experiment (i.e., under ultra-high vacuum (UHV) and 150K condition) studied ethylene hydrogenation on MgO supported Pt_n clusters (n = 8 to 15, size is smaller than 1 nm). The results showed that the onset for the hydrogenation reaction happened at Pt_{10} clusters and a maximum rate yielded at Pt_{13} clusters.[109] The significant reactivity differences among Pt single atoms, clusters and nanoparticles, and appearance of the maximum reactivity in the 1.00 wt.% Pt/TiO_2 catalyst that was prepared by the SEA synthesis approach in this study seems to be consistent with these previous studies. It should be noted that the predominant Pt cluster sizes in 1.00 wt.% Pt/TiO_2 is ~1.1 nm, about 0.3 nm larger than the Pt/carbon catalysts[43,44] showing the maximum reactivity. This difference could be caused by different supports, as TiO_2 is traditionally viewed as a material capable of providing stronger interaction with the supported metal species.[45, 129] In comparison to the ethylene hydrogenation over Pt/MgO catalyst conducted at UHV and low temperature

condition,[109] we worked with metal oxide supported Pt catalysts at more realistic catalysis conditions. The earlier studies only examined reactivity of Pt clusters,[109, 123] while we compared the reactivity of Pt sites ranging from single atoms to clusters and to nanoparticles systematically.

3.3.6 Correlations between activity and geometric/electronic properties of Pt/TiO_2 catalysts

The mechanism of structure sensitivity of supported Pt clusters in styrene hydrogenation has not been resolved. Hypothetically, it can be attributed to the electronic and geometrical properties of supported Pt clusters that have metastable fluxional structures.[43,44] For supported metal catalysts, the geometric and electronic properties, and the correlation between these two properties (or one of them) and the catalyst activity have been discussed in several reports.[130-132] The electronic property often refers to: (i) the quantum size effect of metal nanoclusters compared to the bulk metal and (ii) charge transfer between the support and metal. The geometric property is often linked to the topology of the active sites (e.g., local shot-range structure containing several atoms or a long-range structure that forms the crystal planes). In our study, given the small sizes of Pt aggregates (i.e., average size less than 1.5 nm, which does not form crystalline plane yet), we considered the electronic property as the charge transfer between the support and metal site and the geometric property as the atom topology in the Pt aggregates. The electronic property is thus linked to the Pt atom

coordination environment that is reflected by Pt oxidation state and binding energy position. The theoretical studies showed that a structural transition happens from (quasi-) two-dimensional small clusters to rigid pyramidal clusters with an increasing number of Pt atoms in the catalyst, in which the Pt atoms at the vertices of the pyramidal clusters are electron-rich and can activate carbon double bonds effectively.[43] The experimental evidence for such structural transition is still lacking due to the current instrumentation limitation. This geometric structure change is related to the Pt aggregate size. Therefore, we used the fraction of Pt^{2+} and particle size to represents these two properties in our discussion below. Given the distinct geometric and electronic properties of Pt/TiO_2 catalysts with different Pt loadings, as discussed in Sections 2.3.1-2.3.3 above, some correlations between these properties and the catalytic reactivity should exist. Here we aim to develop these correlations, which could be potentially used to prescreen the properties of as-synthesized supported metal catalysts.

To verify the geometric effects on styrene adsorption in the reaction, ATR-FTIR was conducted on the Pt/TiO_2 catalysts before and after styrene chemisorption. As shown in Figure 3.11a, adsorption on Pt single atoms in 0.04 wt.% Pt/TiO_2 and Pt sub-nanometer clusters in 0.12 wt.% Pt/TiO_2 showed similar spectra as pure TiO_2 support, in which the absorption of styrene was barely noticeable. In samples containing Pt nanometer clusters and nanoparticles e.g., (0.50 wt.% and 5.00 wt.% Pt/TiO_2), two peaks (1545, 1420 cm^{-1}) associated with aromatic C=C bending were observed, indicating the chemisorption of styrene on the samples.

Styrene hydrogenation has been recognized to involve the surface reaction of co-adsorbed π-bonded ethenyl groups in styrene and dissociated hydrogen.[133] The dissociative adsorption of hydrogen can take place on Pt single atoms, but adsorption of ethenyl group in styrene, however, is unlikely due to spatial restriction. To study the metallic property of the Pt/TiO_2 catalysts,[134] H_2-TPR of Fe_2O_3 in the presence of Pt/TiO_2 catalyst was studied. As shown in Figure 3.11b, two major peaks at ~643 K and ~893 K were observed in the H_2-TPR profiles, which can be assigned to the reduction of Fe_2O_3 to FeO and then to Fe, respectively.[135] The H_2-TPR peaks from the reduction of Pt/TiO_2 catalyst are negligible. The reduction peaks in the physical mixture of Fe_2O_3 and 0.04 wt.% Pt/TiO_2 or Fe_2O_3 and 0.12 wt.% Pt/TiO_2 stayed at the similar positions, while both peaks moved slightly to lower temperatures when the nanometer Pt clusters in 0.50 wt.% Pt/TiO_2 and nanoparticles in 5.00 wt.% Pt/TiO_2 exist. These data suggest the Pt sites with larger aggregation sizes are more effective in enabling the hydrogenation. The synergism between noble metal single atoms and nanoparticle has been reported to have the ability to boost the hydrogenation activity of supported metal catalysts.[110, 136] This synergetic effect could also explain the high activity of nanometer cluster Pt/TiO_2 catalysts. On these catalysts (0.50 -1.00 wt.% Pt/TiO_2) Pt single atom and nanometer cluster coexist on the support; as the H_2-TPR results indicates, hydrogen dissociation preferably happens on metallic nanometer cluster and the activated H atom would spillover towards Pt single atom site to facilitate the hydrogenation of styrene. Whereas on Pt/TiO_2 catalysts with lower or higher loadings, due to the absence of Pt

nanocluster or single atom there was no synergetic effect, which resulted relatively lower hydrogenation activity as compared to nanometer cluster catalyst.

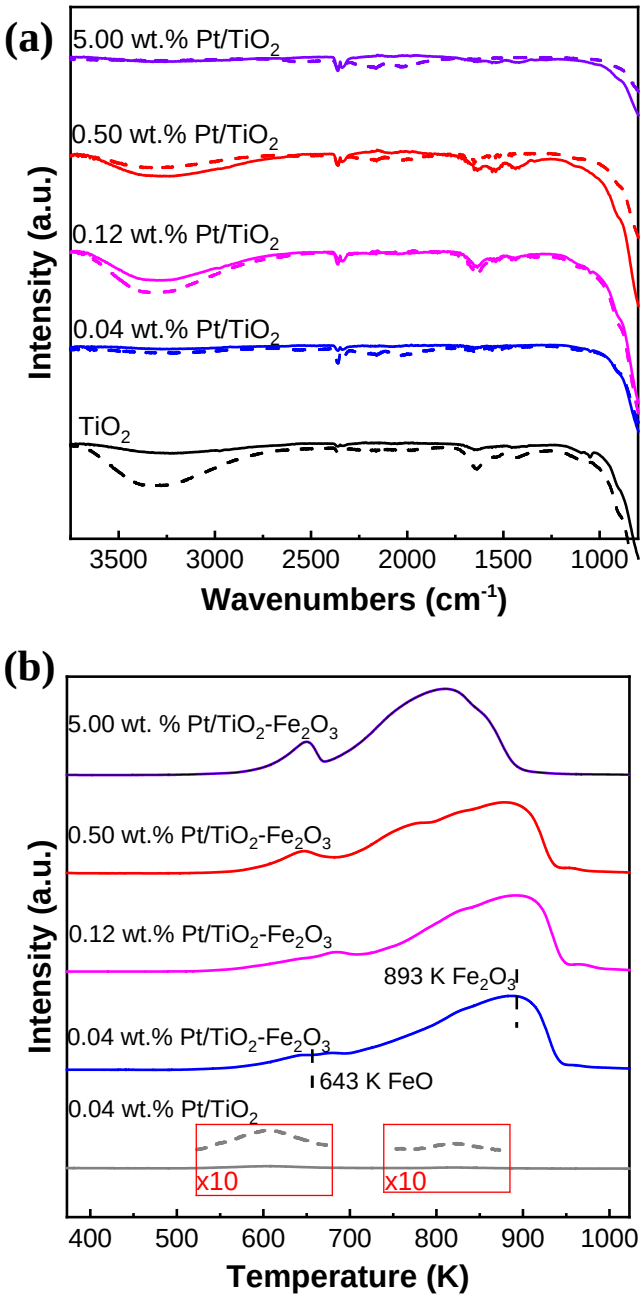

Figure 3.11 (a) FTIR of Pt/TiO_2 catalysts with various Pt concentrations (0.04 wt.%-1.00 wt.%) before (dotted line) and after (solid line) styrene chemisorption. (b) H_2-TPR of mixture of Fe_2O_3 and Pt/TiO_2 catalysts with various Pt concentrations (0.04 wt.%-5.00 wt.)

The electronic properties of Pt sites in each catalyst should also contribute to the observed reactivity differences. The electron-deficient cationic Pt single atoms do not favor electron donation to the ethynyl group in styrene to enable the reaction.[137] When the Pt size increases from single atoms to sub-nanometer and nanometer clusters as well as nanoparticles, the capability of hydrogenating C=C bond in styrene should be strengthened due to the increasing metallic property.

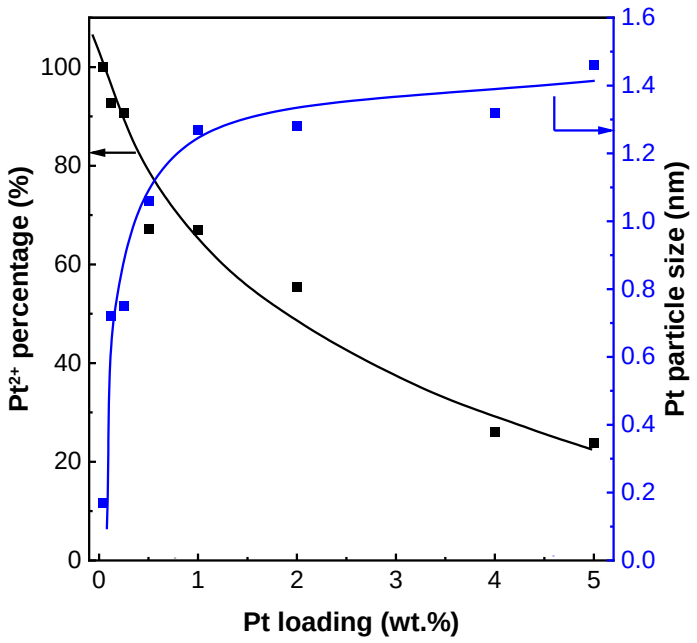

Figure 3.12 Geometric (indicated by particle size) and electronic (denoted by cationic Pt percentage) properties of Pt/TiO_2 catalysts versus Pt loadings.

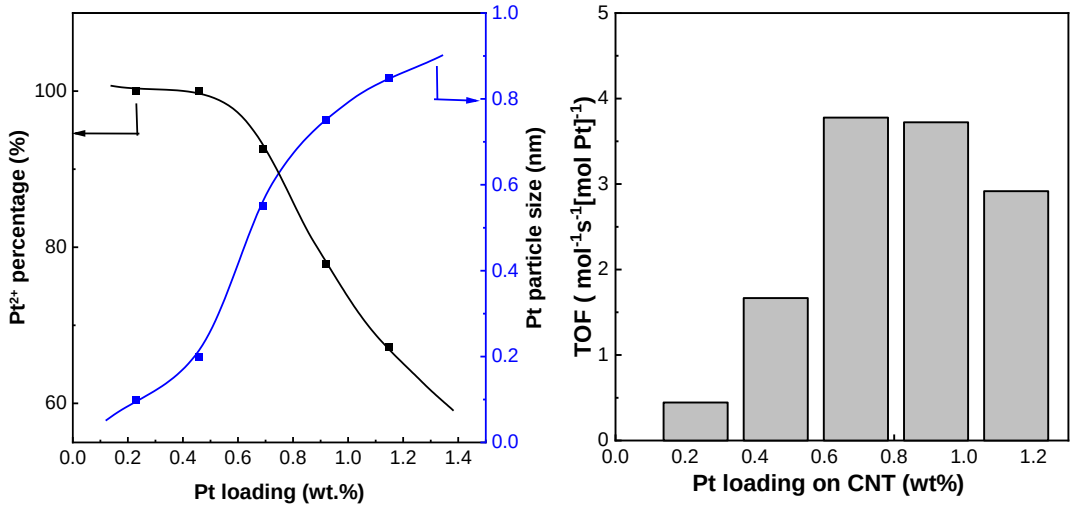

Figure 3.13 (a) Geometric (indicated by particle size) and electronic (denoted by cationic Pt percentage) properties and (b) TOFs of Pt/carbon nanotube catalysts versus Pt loading. The data used in these plots were extracted from reference[124].

To quantify the geometric properties of the Pt/TiO_2 catalysts, the average particle sizes obtained from the HAADF-STEM images were simply used as the descriptor. As shown in Figure 3.12, the particle size monotonically increases with increasing Pt loadings in the catalysts. The electronic properties of these catalysts were represented by the percentage of Pt cationic sites that was obtained from XPS measurements. Opposite to the trend of particle size versus Pt loading, the percentage of cationic Pt sites decreases with increasing Pt content. The intersection of these two plots seems to coincide with the Pt/TiO_2 catalysts (i.e., 0.50 wt.% Pt/TiO_2 and 1.00 wt.% Pt/TiO_2 samples) that have the maximum reactivity in the hydrogenation of styrene. This

indicates that a coupling between the electronic and geometric properties of the catalyst is required to enable effective styrene hydrogenation.

3.4 Conclusion of Chapter 3

In summary, the TiO_2 supported Pt catalysts with different Pt aggregate sizes, i.e., single atoms, sub-nanometer clusters, nanometer clusters and nanoparticles, were prepared by varying Pt loadings on the support using the SEA synthesis process. The geometric, electronic, and catalytic properties of these catalysts were studied by a combination of physicochemical property characterization and styrene hydrogenation reaction behavior. The reactivity of Pt active sites in the form of isolated single atoms is very low. The reactivity increases gently when Pt active sites exist in the sub-nanometer clusters. A significant reactivity increase is observed on the Pt sites in the nanometer clusters. The Pt sites in the nanoparticles showed a slightly decreasing reactivity with increasing Pt particle size in the nanometer scale. The significant variation in reactivity over the Pt sites in single atoms, sub-nanometer and nanometer clusters reflects the structure sensitivity of metastable fluxional catalysts. The maximum reactivity is observed in the Pt/TiO_2 catalyst, in which the predominant Pt cluster size is ~1.1 nm, about 0.3 nm larger than the Pt sizes in the Pt/carbon catalyst showing the maximum reactivity. This difference could be caused by the effect of catalyst support since TiO_2 is traditionally viewed as a material capable of providing stronger interaction with the supported metal. To develop a facile method to screen the

quality (i.e., Pt aggregate size) of synthesized supported Pt cluster catalysts, the reactivity was plotted against the Pt loadings. A volcano-shaped trend of the reactivity of these catalysts with different Pt loadings was found, which is correlated to the Pt particle size and percentage of cationic Pt sites. The correlation developed in this study is also applicable to Pt sites on carbon nanotube supports. It could potentially be used as a general tool to pre-screen supported metal catalysts developed by different synthesis approaches.

Chapter 4: Laser-Engraved Defects in TiO_2 Support: Enhancing Reducibility and Redox Capability of Pt/TiO_2 Catalyst for Reactive and Selective Hydrogenation

4.1 Introduction

Titanium dioxide (TiO_2) has been intensively studied as a catalyst or catalyst support in various photocatalytic[29], electrocatalytic[138] and thermal-catalytic[139] reactions. The efficiency of TiO_2 in these applications depends on its structural, optical and/or electronic properties that are controlled by the material preparation and modification approaches. For example, as a semiconductor material with the large bandgap (3.2 eV for anatase polymorph), TiO_2 absorbs Ultra-violet (UV) light to produce hydrogen[140] and to decontaminate water[141] in solar driven photocatalytic reactions. The modification of TiO_2 material by metal loading[142], metal ion doping[30], hydrogen treatment[143], etc. increases its response to the visible light and efficiency in photocatalysis under natural solar radiation. Due to poor electrical conductivity and unfavorable hydrogen intermediate adsorption/desorption capability,[144] TiO_2 has been an inactive electrocatalyst. The tuning of electronic configuration of TiO_2 by doping or alloying[145], creating defects/vacancies[146], or structural engineering[147], etc. has

successfully improved the activities of TiO_2 in H_2 evolution in electrochemical processes. As the catalyst support, TiO_2 not only carries and stabilizes the metal particles but also creates interface between metal and support to promote the catalyst activity. The metal-support interaction depends on the TiO_2 polymorphs, defective vacancy structures, and morphologies.[148, 149] A rational design and modification of TiO_2 materials is therefore crucial to obtain efficient catalysts with high activity, good selectivity, and low rate of deactivation.

Laser irradiation has proven to be a simple and versatile technique to create nanostructured metal oxide materials.[150] The technique is primarily based on the photothermal effect induced by a focused laser that remotely generates a confined temperature field at a desired position in the treated materials. The process has fast heating and cooling rates and localized thermal effects, allowing selectively annealing the films and nanostructures without thermal interference with the underlying substrates and adjacent structures. The laser processing of TiO_2 materials has been reported previously, mainly focused on the laser direct writing to create surface microstructures or patterns on substrate surfaces[151] and laser ablation in liquid phase to synthesize TiO_2 nanostructured particles[152]. The laser processing of a substrate surface has shown great potential in fabricating TiO_2 structures for micro-electro-mechanical systems, diffractive optical elements and bio-applications. For example, the laser processing of a titanium substrate induced selective and localized formation of TiO_2 layer with anatase, rutile or mixed polymorph phases, which wrought and optimized the titanium substrate for bioimplant application.[153] The laser irradiation on a rutile

TiO_2 crystal led to oxygen deficiencies and crystal structure distortion due to stacking faults caused by the large oxygen deficiency. The obtained oxygen-deficiency TiO_{2-x} layer, however, exhibited unconventional metallic behavior as the electrical resistivity exceeded 10^4 Ω cm below 42 K.[154]

Different form the surface fabrication induced by the laser direct writing, laser ablation in the liquid phase works with a solid target to produce nanoclusters that is released into the liquid environment to form a colloidal nanoparticle suspension. The synthesis of metal oxide particles using laser irradiation of metal targets in a liquid medium was started around 1990s.[155-157] The first synthesis of TiO_2 nanoparticles using this approach was reported in 1997 by Kawasaki group.[158] These TiO_2 materials made by laser irradiation method have led to important applications in the research fields of electrocatalysts[159], photocatalysts[160-161], and photoelectrochemical materials[162] for clean energy applications. It should be noted that the application of laser-processed TiO_2 materials for thermal catalytic applications has been rarely studied. Specially, as the catalyst support, the TiO_2 support and the carried-metal species often have metal-support interaction that influences catalytic performance significantly.[163] The property of the laser-treated TiO_2 structures and its influences on the supported metal species and the catalytic reaction under thermal catalytic reaction conditions still remain as an less explored subject.

In this work, we applied the laser engraving onto an anatase TiO_2 sample and studied the physiochemical property changes endured by the laser treatment. The process was done by direct laser writing followed a designed pattern on the TiO_2 pellet,

in which an infrared (IR) laser (i.e., carbon dioxide (CO_2) laser with wavelength of 10.6 μm) in the engraving mode was employed. We then used the laser-engraved TiO_2 as a support for the platinum (Pt) catalyst (i.e., Pt/TiO_2) to examine the metal-support interactions and catalytic performances. The laser engraving caused particle sintering and crystalline phase heterogeneity in the TiO_2 support. It also created structural defects such as oxygen vacancy and Ti^{3+} species and changed the optical and electronic properties. The defect stability, reducibility and redox ability of the laser-engraved TiO_2 were investigated. The Pt/TiO_2 catalyst has stronger interaction between the Pt clusters and laser-engraved TiO_2 support. The catalytic reaction tests (i.e., selective hydrogenation of 3-nitrostyrene and furfuryl alcohol) showed that the Pt/TiO_2 catalyst with laser-engraved defects is more active and selective compared to the catalyst containing pristine TiO_2 support.

4.2 Experiments

4.2.1 Materials

The TiO_2 nanoparticle with 5 nm diameter (anatase, 99.5% purity) was purchased from U.S. Research Nanomaterial. The Pt precursor, tetraammineplatinum(II) nitrite (TAPN, >99.99% metal basis), was obtained from Alfa Aesar. Styrene (>99.5% purity) stabilized with 10 to 20 ppm p-tert-butylcatechol and 3-Nitrostyrene (>97% purity) was purchased from Acros Organics. Furfuryl alcohol and anhydrous 2-propanol were purchased from Sigma-Aldrich. Ethanol (200 proof) was purchased from VWR.

4.2.2 Preparation of defective TiO_2 support by laser engraving

Prior to the laser engraving experiment, the as-purchased TiO_2 sample was pressed into a pellet (12.7 mm in diameter, 0.5 mm in thickness) using a pellet die set (MSE supplies) and 38.7 MPa pressing pressure. The as-prepared TiO_2 pellet was then placed on a glass slide and the glass slide together with supported TiO_2 pellet was brought to the X-Y sample stage in the laser engraving equipment (Epilog FusionPro model 16000 with CO_2 laser). The wavelength of the CO_2 laser from this equipment is 10.6 μm with a maximum power of 120 W. The laser beam with a diameter of 0.13 mm was concentrated on the sample by focus lens with a focal length of 50.6 mm. The engraving path of the laser beam was pre-designed (see Figure S1) and controlled by a computer during the engraving experiment. The writing power was 75% of maximum power and scan speed of 8.6 mm/s. The laser-engraved TiO_2 sample was named as TiO_2-LE1, where "1" stands for the number of laser treatment cycle.

To increase the degree of laser treatment on the TiO_2 sample, after one cycle of laser engraving, the pellet was grounded into fine powder, pelletized using the same procedure as described above, and then exposed to the laser-engraving treatment. The pellet pressing, laser treatment and grinding procedures were repeated for 4 times, and the resulted sample was denoted as TiO_2-LE4. For comparison purpose, we also prepared the reduced TiO_2 (denoted as TiO_2-RE) sample by exposing the as-purchased anatase TiO_2 to 5% H_2/N_2 gas flow (50 mL/min) at 873 K for 2 h (5 K/min ramp rate)

in a tubular furnace. The defects induced by chemical reduction in TiO_2 were compared to those of the laser-engraved TiO_2 to examine their property differences.

4.2.3 Preparation of Pt/TiO_2 catalyst

The Pt/TiO_2 catalysts with Pt concentration of 0.50wt% were prepared by the wetness impregnation method. In the experiment, 0.15 g TiO_2 powder sample (either as purchased or laser-engraved) was dispersed in 15 mL DI water by 10 min of sonication using an ultrasonic bath (Fisher Scientific FS60). In the meantime, 0.085 g of TAPN was dissolved in 5.00 mL of DI water in a glass vial to form the Pt stock solution. 0.18 g of the Pt stock solution was then diluted with DI water into 3.75 mL. The diluted TAPN solution was then added to the TiO_2 suspension dropwise. Vigorous stirring by a magnetic stirring bar on a stirring plate was applied in the mixing process. The resultant suspension was kept stirring condition for 30 min and then was transferred to a 343 K convection oven (VWR Sheldon Manufacturing Model, 1350GM Gravity Convection Oven) to evaporate the solvent. Afterwards, the dried TAPN/TiO_2 sample was calcined at 553 K (ramp rate of 5 K/min) for 4 h in a furnace (Thermo Scientific Lindberg/Blue M™ Multipurpose Box Furnaces). The air (Airgas, research grade) flow rate was kept at 50 mL/min in this calcination step. The calcined sample was transferred to a tubular furnace for reduction at 423 K for 2 h with diluted H_2 (5%H_2/N_2 mixture) at a flow rate 100 mL/min. The reduced samples were then stored in a desiccator prior to the characterization and catalytic reaction experiments.

4.2.4 Catalyst characterization

Diffuse reflectance (DR) Ultraviolet-Visible (UV-Vis) spectra of TiO_2 samples were measured using an Ocean Optics USB2000+ spectrometer, which was equipped with an IS200-4 integrating sphere detector, and the white high reflectance sphere material (manufactured from Polytetrafluoroethylene (PTFE) based bulk material) was used as reference. Powder X-Ray diffraction (XRD) patterns of samples were recorded using a Bruker D8 Advance Lynx Powder Diffractometer (LynxEye PSD detector, sealed tube, Cu Kα radiation with Ni β-filter). The Raman spectra was obtained using a Yvon Jobin LabRam ARAMIS spectrometer with a 532 nm laser as an excitation source. N_2 adsorption-desorption isotherms of the samples were measured using an Autosorb-iQ equipment (Quantachrome Instruments) at 77 K. The samples were outgassed at 573 K for 10 h at 1 mmHg pressure prior to the measurements. Brunauer, Emmett and Teller (BET) method was used to determine the specific surface areas of the samples. The coordination environment of Pt was characterized by X-ray photoelectron spectroscopy (XPS) using a Versaprobe III by Physical Electronics Inc. (PHI) X-ray photoelectron spectrometer. Powders were deposited on carbon tape for sample immobilization in the chamber. X-rays were generated with a monochromated Al Kα anode at 25 W and a beam size of 100 μm. The chamber pressure during analysis was 5×10^{-6} Pa or less. Surveys were performed with a pass energy of 224 eV for each sample, and higher resolution elemental scans were collected with pass energies of 55

eV, both had take-off angles of 45 degrees. Electron paramagnetic resonance (EPR) measurements were performed on a Bruker EMX EPR spectrometer. The microwave frequency was varied around 9.5 GHz. Microwave power of 5.0 mW, frequency modulation of 100 kHz, and modulation amplitude of 3.12 G were applied during the experiment. The scans were run at 3350 G center field and a sweep width of 1000 G. Four scans were added to improve signal-to-noise ratio. The morphology of TiO_2 samples were observed by transmission electron microscopy (TEM) using a JEM 2100 LaB6 electron microscope. The morphologies of Pt loaded TiO_2 samples were observed by scanning transmission electron microscopy (STEM) with Thermo Scientific (FEI) Titan Themis S/TEM operating in probe mode at 200 kV with HAADF detector using gun lens 7 and spot size 7.

4.2.5 H_2-TPR, O_2-TPO and CO chemisorption measurements

The temperature programed reduction by hydrogen (i.e., H_2-TPR) measurements of the TiO_2 samples were carried out in the Quantachrome Autosorb iQ instrument, which is equipped with a thermal conductivity detector (TCD) to record the H_2 consumption. Prior to the measurement, the TiO_2 sample was pretreated with 40 mL/min N_2 (Airgas, Research grade) at 553 K for 2 h. After cooled to 323 K, the H_2-TPR measurement was started by switching the N_2 gas to 5%H_2/N_2 (N_2 as balance gas in the gas mixture) at 50 mL/min flow rate. The sample was then heated to 1173 K at 10 K/min ramp rate and kept at the final temperature for 10 min. A liquid nitrogen cold

trap was used to remove water produced throughout measurement to avoid interference with the TCD signals. For the H_2-TPR measurements of Pt/TiO_2 catalysts, the as-prepared samples were firstly calcined at either 553 K (mild condition) or 873 K (harsh condition) (ramp rate of 5 K/min) for 4 h in a furnace (Thermo Scientific Lindberg/Blue M™ Multipurpose Box Furnaces). The air (Airgas, research grade) flow rate was kept at 50 mL/min. The calcined sample was then exposed to the same procedure as that of the H_2-TPR measurement of TiO_2 samples described above.

The temperature programed oxidation by oxygen (O_2-TPO) measurements of the TiO_2 samples were conducted using the same equipment and nearly the same procedure as those of H_2-TPR measurements. The only differences were that the $5\%O_2/N_2$ (N_2 as balance gas) gas was used and the catalyst sample was heated to 873 K. After the first TPO measurement, the TiO_2 sample was cooled down to room temperature. Then, we repeated the O_2-TPO measurement on the sample for three more times successively to examine the redox property of the corresponding TiO_2 material.

The chemisorption of carbon monoxide (CO) on the Pt/TiO_2 samples was measured by pulse titration in the same Quantachrome Autosorb iQ instrument. The catalyst was pretreated in an Ar flow (50 mL/min) at 553 K for 4 h and cooled down to 323 K. The sample was then reduced at 523 K in $5\%H_2/N_2$ (50 mL/min) for 1 h, followed by Ar gas purge for 2 h at the same temperature. Afterwards, the sample was cooled down to 303 K in the Ar flowing gas. A series of CO pulses (50 uL in each pulse) were injected with an interval of 5 min until the amount of exit CO pulses

reached a steady state value. The CO signal was recorded using a Prima BT Bench Top Process Mass Spectrometers (Thermo Fisher Scientific, winsford U.K. CW7 3GA).

4.2.6 Catalytic reaction test

The catalytic performance of Pt/TiO_2 catalysts were tested by hydrogenation of 3-nitrostyrene (3-NS) and hydrodeoxygenation of furfural alcohol (FA), respectively. In 3-NS hydrogenation, 0.020 g of Pt/TiO_2 catalyst, 9 mL of ethanol and a Teflon coated magnetic stirring bar (cylindrical shape, 30 mm length and 8mm diameter) were added into a Teflon liner (20 mL volume) of a stainless-steel autoclave reactor. After the catalyst/ethanol suspension was sonicated for 20 s, 0.076 g of 3-NS was dissolved in 1 mL of ethanol. The 3-NS/ethanol solution was transferred into the Teflon liner. The liner was then placed into the stainless-steel jar and sealed by the cap of the autoclave. We charged 5.0 bar of H_2 (Airgas Ultra High Purity 99.9%) into the reactor to purge the air inside. The step was repeated for 3 times. After purging, the reactor was charged again to 3.0 bar of H_2 and transferred to a water bath that was preheated to 313 K. The water bath was placed on a stirring hot plate with a stirring speed of 900 rpm. The moment of placing reactor into the water bath was recorded as the reaction start time. When desired reaction time was reached, the reactor was taken out of the water bath. The pressure in the reactor was then slowly released, and the reaction mixture was sampled by a syringe, filtered by syringe filter and placed into a glass vial. A gas chromatography (Agilent 7890A) equipped with a methylsiloxane capillary

column (HP-1, 50.0 m × 320 μm × 0.52 μm) and a flame ionization detector (FID) for the sample composition analysis.

Hydrogenation of FA over the Pt/TiO_2 catalysts was evaluated using method reported by Fu et al.[111] In the experiment, 0.10 g of furfuryl alcohol and 0.05 g of catalyst were added to 10 mL of anhydrous 2-propanol, and the mixture was transferred into the Teflon liner of the Parr reactor (50 mL volume). The reaction mixture was firstly flushed three times with N_2 (Airgas, Research grade). The reactor was then pressurized to 11.0 bar of hydrogen and an additional 6.9 bar of nitrogen was added. The reaction temperature was set 443 K. After reaction, 2 mL of liquid products were purified with a syringe filter. Liquid samples were analyzed with an Agilent 7890B GC system equipped with an HP-INNOWAX-19091N-133l column and a FID. Products were identified using a SHIMADZU gas chromatography mass spectrometry (GCMS) QP2010 Plus system. Initial rates were calculated by regressing the total concentration of relevant products vs. time at short times (differential conditions; conversion <15%) after the reaction temperature was reached.

4.2.7 DFT calculation methods

The Vienna Ab-initio Simulation Package (VASP) code was used for all calculations.[164, 165] The Perdew-Burke-Eruzerhof (PBE) functional in the generalized gradient approximation (GGA) framework was used for the exchange and correlation functional.[166] The projector-augmented wave (PAW) pseudopotentials were used to

model the interaction between ions and electrons.[167] The electron wave function was expanded in plane waves up to a cut-off energy of 400 eV. The convergence accuracy of the force is set to 0.02 e V/Å at structural relaxation. The Gamma meshes of only Gamma point sampling in the Brillouin zone were applied to all relaxation calculations, which has been proven to be effective in dealing with large supercell systems.[168] The 4 × 4 × 1 Gamma meshes were used for the density of states (DOS) calculations. The standard DFT using the GGA method underestimates the band gap of TiO_2 because the GGA method is unable to accurately model the strongly correlated localized 3d electrons of Ti atoms.[169] However, as an effective approximation method, the relative values calculated by GGA method are accurate and have no effect on the DOS and charge density analysis.

The substrate systems we employed in this study are all based on a typical (3 × 1) supercell of anatase TiO_2 (101) surface, shown in figure 1. The supercell contains five TiO_2 monolayers with a total of 180 atoms. Each slab contains a 15 Å of vacuum layer to separate the surrounding identical slab. The surface Ti atoms contain 5-coordinated Ti (Ti_{5c}) and 6-coordinated Ti (Ti_{6c}), and the surface O atoms contain 2-coordinated O (O_{2c}) and 3-coordinated O (O_{3c}). During structural relaxation, the bottom two layers were fixed to simulate the bulk phase structure, while the top three layers were allowed to fully relax with the Pt clusters on the surface. The construction of the surface oxygen vacancy is obtained by deleting an O_{2c} atom on the anatase TiO_2 (101) surface. The Pt_4 cluster was selected as a representative of Pt clusters because Pt_4 is a typical unit of large Pt clusters.[170] The Pt_4 cluster was put into a 10 × 10 ×10 $Å^3$ cubic

box and the Gamma meshes of 6 × 6 × 6 k-point sampling were used to calculate the total energy of the Pt_4 cluster. The adsorption energy of the Pt_4 cluster on the anatase TiO_2 (101) surface was defined as the difference between the total energy of the adsorption system of the anatase TiO_2 (101) surface with Pt_4 cluster adsorbed and the sum of the energies of the free Pt_4 cluster and clean anatase TiO_2 (101) surface. The larger the absolute value of the adsorption energy, the more likely that the corresponding adsorption system is to be stable.

4.3 Results and discussion

4.3.1 Morphology, crystalline phase and optical properties of laser-engraved TiO_2 sample

The appearance of TiO_2 samples, prior to and after the laser engraving treatment, has distinct colors. The digital photographs (inset in Figure 4.1) show that the as-purchased TiO_2 has a white color. After the laser treatment, the sample changed into grey. The increase in the treatment cycle darkened the greyish color. The changes in sample color occurred in the laser engraving treatment are consistent with those observed from the laser direct writing[171] or laser ablation in liquid environment[152]. The origination of the color change is the response of laser-engraved sample to the visible light in the natural solar radiation. The DR UV-vis spectra in Figure 4.1a confirmed the increase in the absorption of visible light (e.g., wavelength of 400-800 nm) of the laser-

engraved TiO_2 samples. In contrast, the pristine TiO_2 only absorbs in the UV region (i.e., < 400 nm). The presence of structural defects such as Ti^{3+} or oxygen vacancy species could attribute to the changes of the optical properties such absorption onset wavelength (λ_{onset}, nm) and bandgap (E_g, eV), as reported for the black TiO_2 prepared by hydrogen treatment[172] or laser ablation in liquid solution[152]. The onset wavelength of the light absorption can be directly obtained from extrapolating the straight-line portion of the absorption curves to zero absorption (Figure 4.1a).[173] The onset of light absorption (Figure 4.1a) for the laser-engraved TiO_2 particles was extended to the visible region (e.g., TiO_2-LE1, 406 nm; TiO_2-LE4, 420 nm), compared to 387 nm of the pristine anatase TiO_2.

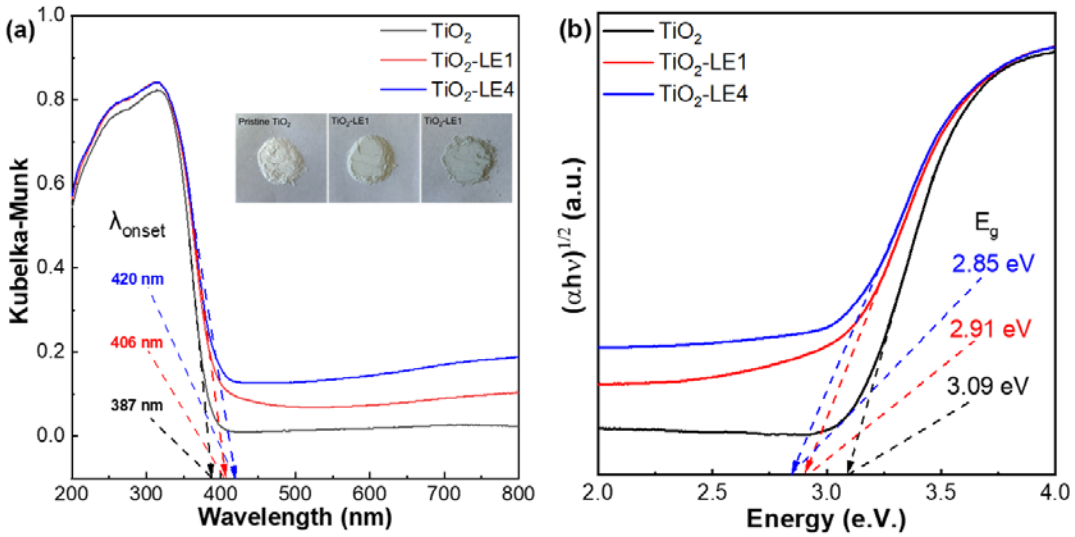

Figure 4.1 (a) DR UV-vis spectra and (b) Tauc plots of TiO_2, TiO_2-LE1 and TiO_2-LE4 samples. (Inset digital images in (a) show color appearances of these three samples.)

The band gap can also be obtained from the Tauc Plot (Figure 4.1b) by plotting $(\alpha h\nu)^2$ versus $h\nu$ curve and extrapolating the data to the photon energy axis where $(\alpha h\nu)^2 = 0$, in which α is the energy-dependent absorption coefficient, h is Planck constant and ν is the photon's frequency (refer to Section S1 in the Supporting Information). The band gap reduced from 3.09 eV of pristine TiO_2 to 2.91 eV of TiO_2-LE1 and then to 2.85 eV of TiO_2-LE4. The decrease in the band gap could result from formation of the rutile phase with a band gap (~3.0 eV) smaller than that (3.2 eV) of anatase TiO_2. The close contact between anatase and rutile phase can induce band gap narrowing as a result of the characteristic band alignment at the anatase/rutile interface.[174] The formation of defects in TiO_2 could be another reason for the band gap narrowing.[175] The light absorption and band gap values suggest that defects were created in the TiO_2 sample by the laser engraving treatment.

TiO_2 exists multiple polymorphs such as anatase, brookite, rutile.[176] The laser treatment could cause phase transformation across these polymorphs. The XRD data in Figure 4.2a shows that the anatase phase exists in the pristine TiO_2 sample (JCPDS #75-1537). After the laser treatment, the rutile phase (JCPDS #21-1276) appeared and become more obvious with the number of laser treatment cycles. According to reference intensity ratio (RIR) analysis in Table 4.1, the percentage of rutile phase increased from 26.4% of TiO_2-LE1 to 39.6% of TiO_2-LE4. To further study crystalline phase change caused by the laser irradiation, Raman spectra of TiO_2 and TiO_2-LE4 samples were measured (Figure 4.2b). The pristine TiO_2 showed well resolved characteristic bands related to the anatase phase[177] at 148 cm^{-1} (E_g), 394 cm^{-1} (B_{1g}), 513

cm^{-1} (A_{1g}), and 640 cm^{-1} (Eg) regions, respectively. The TiO_2-LE4 showed mixed phases of anatase and rutile, in which 237 cm^{-1} (multi photon absorption), 438 cm^{-1}(E_g) and 608 cm^{-1} (A_{1g}) peaks are attributed to the rutile phase[178].

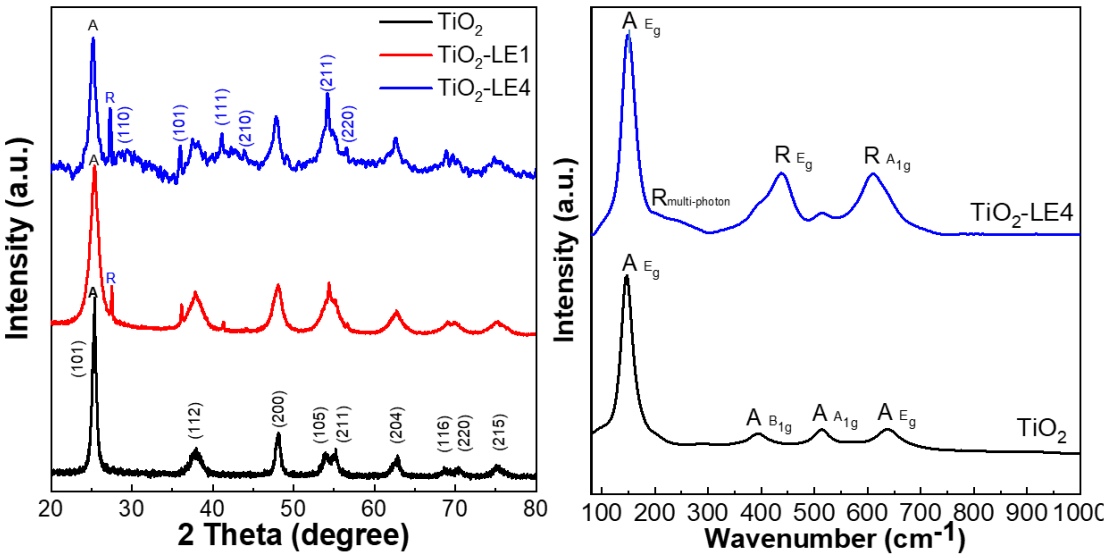

Figure 4.2 (a) XRD patterns of TiO2, TiO_2-LE1 and TiO_2-LE4 samples (A: anatase phase; R: Rutile phase). (b) Raman spectra of TiO_2 and TiO_2-LE4 samples.

Table 4.1. ratio of anatase/rutile phase from XRD

	I_a/I_b	X_a/X_b	**Anatase%**	**Rutile%**
LEx1	3.96032	2.78165	73.5565	26.4435
LEx4	2.17568	1.52815	60.4454	39.5546
LEx8	0.64219	0.45106	31.0849	68.9151

The morphology changes in TiO_2 samples caused by the laser irradiation were revealed by the electron microscopy examination. The SEM image in Figure 4a shows that the anatase TiO_2 contains uniform nanoparticle aggregates. After the laser treatment, the particle aggregate sizes increased (Figure 4.3b-c). Some large aggregates in TiO_2-LE1 and TiO_2-LE4 samples were highlighted by the white circles. The increase in particle size should result from the thermal sintering effects occurred during the laser engraving. As shown in Figure 4.3d, the as-prepared TiO_2 pellet has a rough and uneven surface, in which the loosely attached nanoparticles are clearly visible. In contrast, the pellet surface of the TiO_2-LE1 sample in Figure 4.3e is smoother and contains large grains and grain boundaries. The CO_2 laser with a wavelength of 10.6 μm in the laser irradiation primarily endured the thermal heating effects, similar to the high temperature sintering process occurred in the conventional furnace. A cross-section view of the laser-engraved TiO2-LE1 sample (Figure 3f) showed ~5 μm thickness of the top surface of the pellet was sintered. The sample pellet thickness was ~500 μm. If we assume the entire pellet has uniform density. It is estimated that 1% of TiO_2 in the pellet was impacted by the laser irradiation. Nevertheless, according to the RIR analysis of the XRD pattern in Figure 4.2, 26.4% of the anatase TiO_2 sample has transformed into the rutile phase in TiO_2-LE1, which is equivalent to ~132 μm penetration thickness into the sample pellet. Either by direct heating or conductive heating or thermal shocking, the influences of laser engraving on the temperature field in TiO_2 sample is far more remote than visualized by morphology changes in Figure 3e-f. The increase in the TiO_2 particle size leads to the surface area reduction. As shown in Figure 4.4**,** the

N_2 uptake decreases with the number of laser treatment cycles on the TiO_2 sample. The BET surface area of TiO_2 decreased from 185 m^2/g to 142 m^2/g of TiO_2-LE1 and to 81 m^2/g of TiO_2-LE4, respectively.

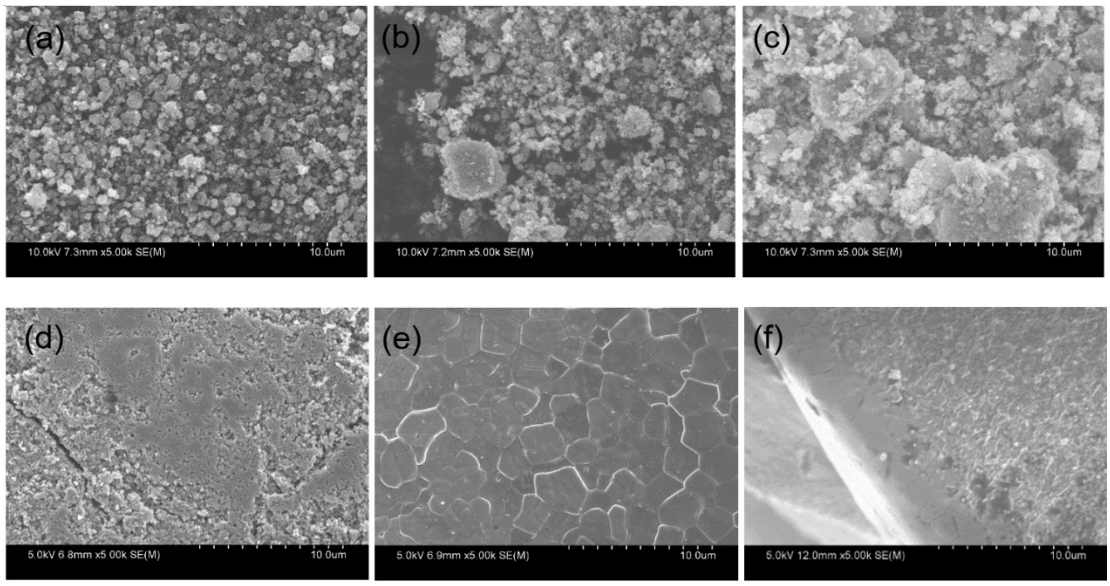

Figure 4.3 SEM images showing morphologies of (a) TiO_2, (b) TiO_2-LE1 and (c) TiO_2-LE4 powder samples. (d) and (e) show top-view morphologies of TiO_2 sample pellet before and after 1 cycle of laser engraving treatment, respectively. (f) shows cross-sectional view of the sample pellet in (e).

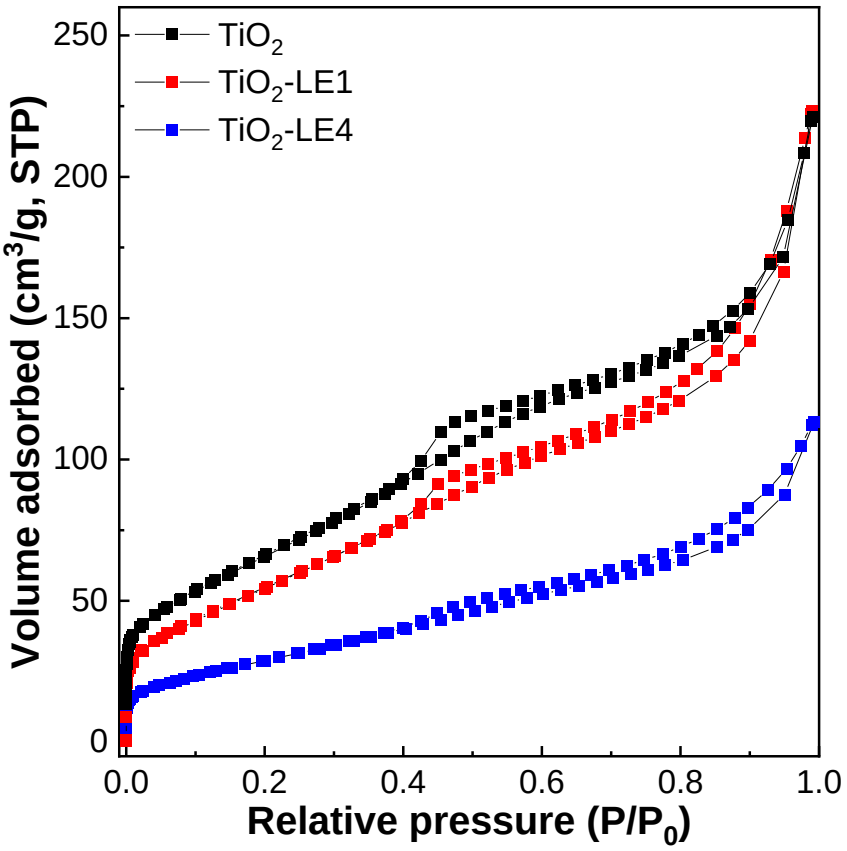

Figure 4.4 N_2 adsorption-desorption isotherms of TiO_2, TiO_2-LE1 and TiO_2-LE4 samples.

Transmission electron microscopy (TEM) and high-resolution transmission electron microscopy (HR-TEM) were used to study the lattice structures in the pristine and laser-engraved TiO_2 samples. The as-purchased TiO_2 contains aggregations of uniform nanoparticles (Figure 4.5a). After the laser treatment, bigger TiO_2 particles were found in the low magnification images as shown in Figure 4.5b-c. After one cycle of laser engraving, the TiO_2-LE1 (Figure 4b) has showed small density of large TiO_2 nanoparticles. The continual laser treatment leads to growth in density and size of large

TiO_2 nanoparticles, as seen in Figure 4c. The Fast Fourier Transform (FFT) of HR-TEM was used for phase determination as shown in the Figure 4d-f. The d spacing was calculated by the formula d = 2/L, where L is the distance between the two bright spots from the FFT pattern. Before the laser treatment, the TiO_2 nanocrystals (Figure 4.5d) showed clear well-defined lattice fringes with an average particle size ~6.72 nm. The indexed d spacing showed characteristic lattice spacing of anatase (101) plane. The big particles that were larger than the pristine anatase TiO_2 nanoparticle were found to be rutile phase. The indexed d spacing in Figure 4.5e-f showed rutile (110) and (101) plane respectively. Besides the crystalline phase change, the defects created by laser engraving treatment were visualized by HR-TEM as shown in Figure 4.6. As the inset image of magnified region showed, the lattice fringes became discontinuous in laser-engraved TiO_2, and the lattice fringes became distorted throughout the nanocrystal. The increased particle size with laser-treatment cycles were in good agreement with the surface area tested by N_2 adsorption-desorption isotherms. The distorted lattice fringes on the TiO_2 were indication of defect formation on the nanocrystal, which further proved the disordered structure after the laser-engraving treatment.[172]

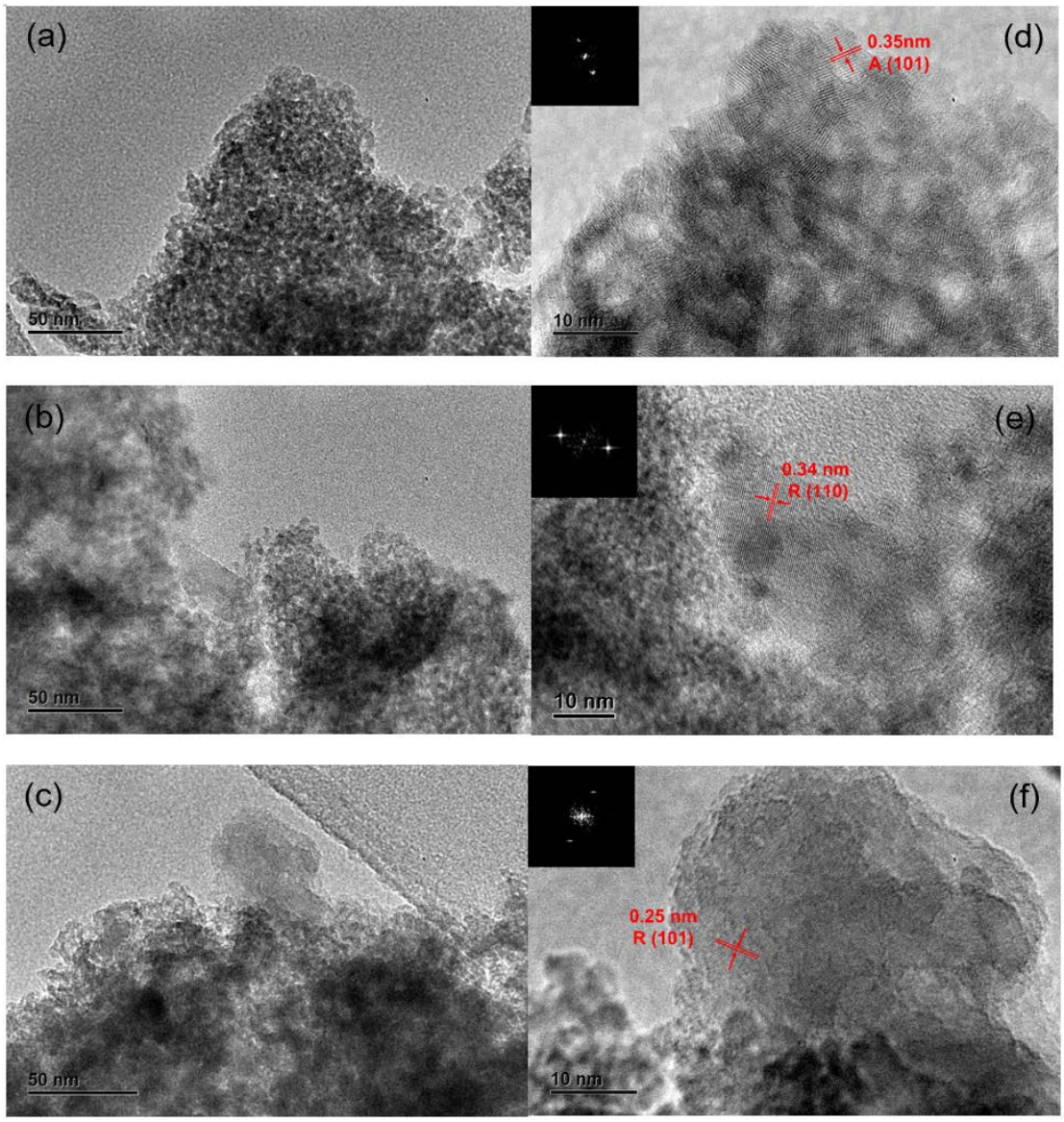

Figure 4.5 TEM images of TiO_2 (a, d), TiO_2-LE1 (b, e) and TiO_2-LE4 (c, f) samples. Highlighted regions in (b) and (c) are large particles in the corresponding samples. (e) and (f) are the high magnified images of circled regions in (b) and (c), respectively.

Inset images in (d)-(f) show FFT of the area where the d-spacing was measured. (A: anatase phase; R: Rutile phase).

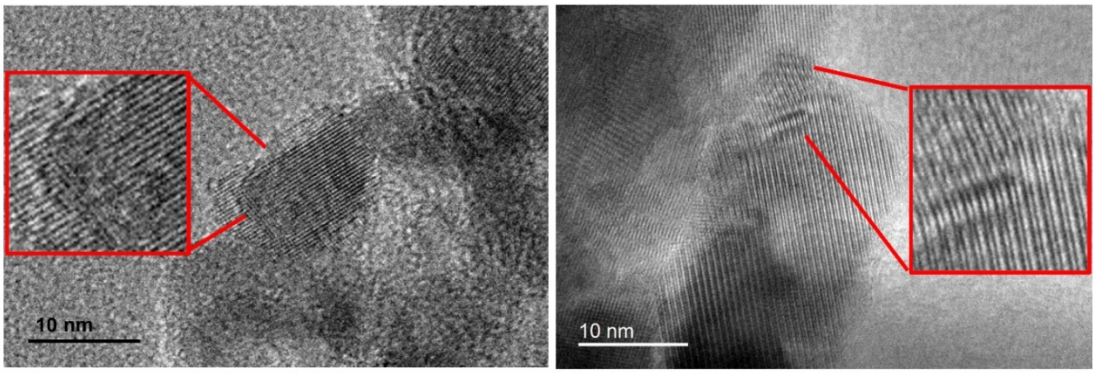

Figure 4.6 HR-TEM images of TiO_2-LE4 showing the defects on TiO_2 nanocrystal

4.3.2 Defects in laser-treated TiO_2 sample

The change in color appearances (inset in Figure 4.1a) and DR UV-vis absorption spectra (Figure 1a) from the pristine TiO_2 to laser-engraved TiO_2 samples has indicated the laser treatment induced defects formation in the laser-treated TiO_2 material. To further study the generated defects, we measured EPR spectra of the laser-treated TiO_2 samples as well as the spectrum of the as-purchased TiO_2 sample. The perfect TiO_2 structure is silent for EPR, due to the close-shell electron structures for both Ti^{4+} and O^{2-} sites. The introduction of defects in TiO_2 could generate oxygen vacancy (O_v) or Ti^{3+} centers, which can trap a single electron to produce active EPR responses.

Figure 4.7 shows that the pristine TiO_2 had one weak signal at g factor of 2.004. After one cycle of laser treatment, this signal increased obviously in the TiO_2-LE1 sample, accompanied with a small shoulder signal at g factor of 1.999. The increase in

the laser treatment cycles apparently enhanced the intensity of the signal at g = 2.004 and the shoulder signal at g = 1.999, as visualized in the TiO_2-LE4 sample. From literature reports, the lattice Ti^{3+} centers give a g value in a range of 1.94-1.99,[179-181] and O_v centers gives a g value of 2.001-2.005,[182] and the surface Ti^{3+} center tend to adsorb atmospheric O_2 to produce O^{2-}, which shows EPR signals at g~2.02.[146] The EPR signal at g factor of ~2.004 is attributed to electron trapped in oxygen vacancies (O_v) of TiO_2 [183, 184], although it is not sufficient to confirm the O_v sites are from anatase phase, rutile phase, or a combination of both phases. The EPR spectra in Figure 6 suggest that the laser engraving treatment created both oxygen vacancy and Ti^{3+} defects in TiO_2, but the dominant defects are the oxygen vacancies. This structural feature is quite different from that of defective TiO_2 created by reductive annealing processes. The previous studies show that reduced TiO_2 at high temperature (e.g., > 600ºC) in either hydrogen atmosphere or vacuum condition predominantly contains Ti^{3+} sites.[185]

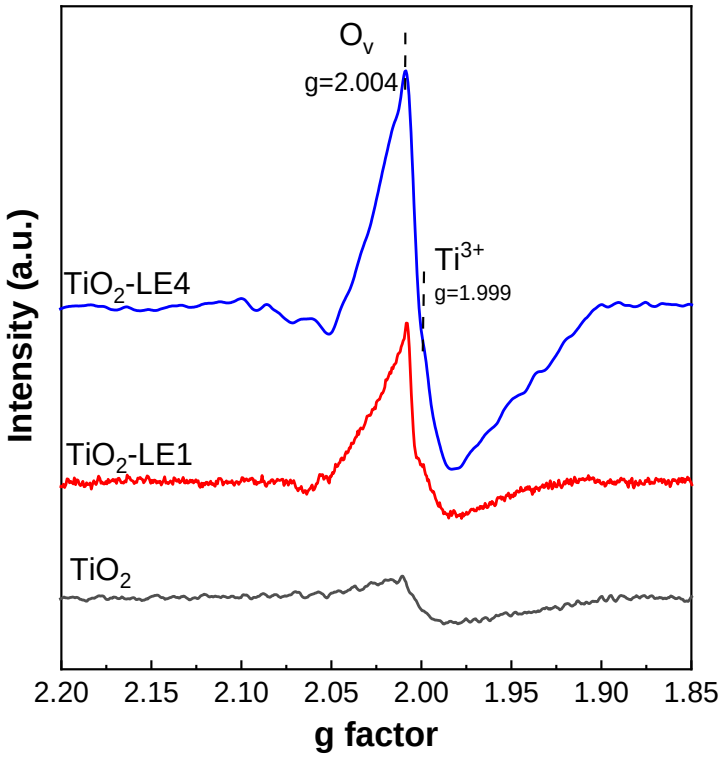

Figure 4.7 EPR spectra of TiO_2, TiO_2-LE1 and TiO_2-LE4 samples.

4.3.3 Reducibility and redox property of laser-treated TiO_2 sample

To study the reducibility and redox property of laser-engraved TiO_2, H_2-TPR, O_2-TPO and successive O_2-TPO experiments were carried out on both TiO_2 and TiO_2-LE samples. For comparison purpose, the H_2-TPR profiles of commercial Degussa P25 and TiO_2 annealed in reducible hydrogen were measured at the same conditions. As shown in Figure 4.8a, the pristine TiO_2 sample has three reduction regions, located at ~570 K, ~870 K and 953 K, respectively. The peak around 570 K is quite weak, which is attributed to the reduction of oxygen species associated with defects in the as-

purchased TiO_2. On the contrary, the peak at ~870 K was quite strong, which can be ascribed to the reduction of the surface oxygen, leading to the creation of oxygen vacancies on the TiO_2 surface in the hydrogen gas atmosphere.[120] The high temperature peak at 953 K was associated with the reduction of bulk oxygen of TiO_2 particles.[121] After the laser treatment, the low temperature peak became stronger while the medium and high temperature peaks became weaker. In addition, the medium-temperature peak at ~870 K moved to lower temperatures, i.e., ~850 K in TiO_2-LE1 and ~820 K in TiO_2-LE4, respectively. The increase in the number of laser treatment cycles strengthened these changes. The increase in the intensity of peak at 573 K was caused by the increase in defects in the structure. The decrease in the peak position and change in the medium-temperature peak shape might be related to the rutile phase formation, as it is a more reducible than the anatase phase.[186, 187]

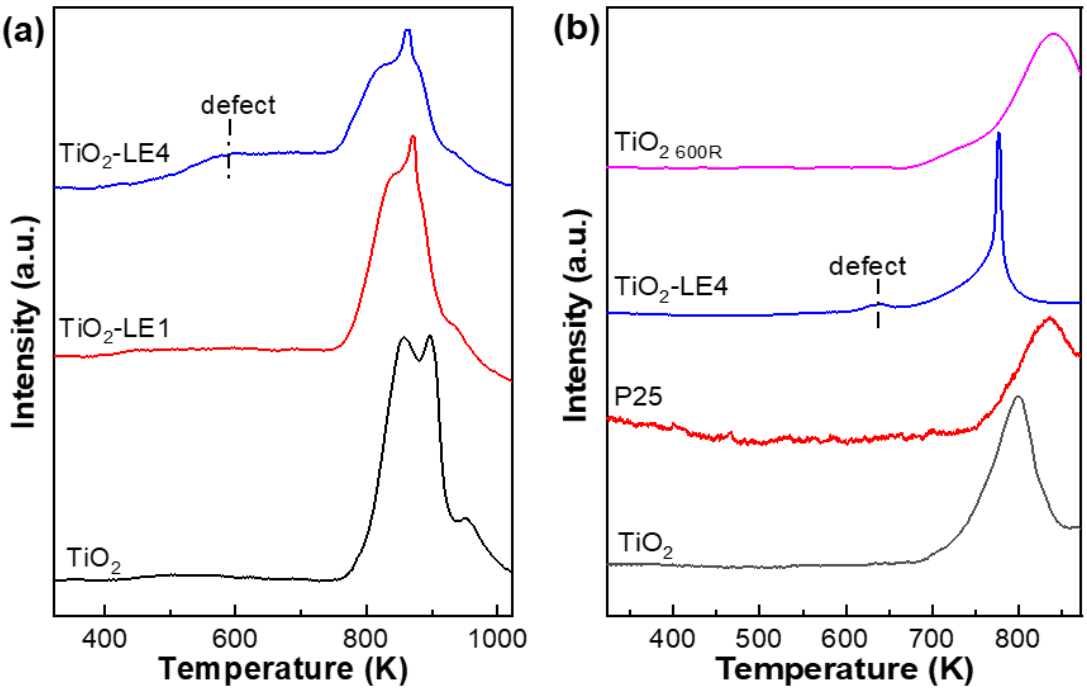

Figure 4.8 H_2-TPR profiles of TiO_2, TiO_2-LE1 and TiO_2-LE4 samples measured after pretreatment at (a) mild (553 K, 10 K/min ramp rate, 20% O_2/N_2 flow of 50 mL/min) and (b) harsh (873 K, 10 K/min ramp rate, 5% O_2/N_2 flow of 50 mL/min) conditions, respectively.

To examine stability of the laser-engraved defects in the TiO_2-LE samples, we selected TiO_2 and TiO_2-LE4 samples and exposed them to the calcination temperature of 873 K for 1 h in 5%O_2/N_2 gas flow prior to the H_2-TPR measurement. The H_2-TPR profiles obtained on samples treated under this condition are shown in Figure 4.8b. The low-temperature reduction peak (~570 K) associated with defects was absent from the pristine TiO_2 sample. The high temperature peak relevant to the surface oxygen species narrows the peak width and absence of fine feature. In comparison, the TiO_2-LE4 sample still keeps the low temperature peak, indicting the preservation of the defects created by the laser treatment. The high temperature reduction peak had a very narrow shape, locating at 20 K lower temperature position than that of the TiO_2 sample. In comparison, the greyish TiO_2 sample prepared in the reducible environment showed a peak at 842 K with a shoulder peak at 734 K. The commercial P25 had a poor reduction with H_2 due to the presence of a large amount of anatase. The reducibility of TiO_2 samples depended on the surface area, exposed crystal planes and crystalline phase. But still the presence of the low temperature reduction peak in TiO_2-LE4 suggests

oxygen vacancies created by laser treatment is quite robust which resists the oxidative treatment at higher temperature conditions.

We further tested the reversibility of oxygen update and release (i.e., redox property) via the oxygen vacancy sties created by the lates treatment in TiO_2. The experiment was done by running successive O_2-TPO measurements. In the first O_2-TPO cycle, both TiO_2 and TiO_2-LE4 showed a bulk oxidation peak at 673 K, which could be assigned to the oxidation of surface Ti^{3+} sites to the Ti^{4+} state (Figure 4.9). The ramp of temperature to 873K in the oxidative environment healed a fraction of these sites. As shown in the second O_2-TPO cycle, the oxidation peak was reduced significantly and the peak position shifted to 578 K, 95 K lower than the one in the first O_2-TPO cycle. The consecutive O_2-TPO cycles in the third and fourth times continued to heal the defect sites in the TiO_2 sample, but not in the TiO_2-LE4 sample since the peak kept similar intensity after the second O_2-TPO measurement. The peak shift towards lower temperature during the repeated TPO test could be caused by the phase change from anatase to rutile at ~873 K due to lower Gibbs free energy of rutile phase.[188] The laser engraving created defective TiO_2 showed the ability to adsorb and desorb oxygen without permanently transforming to defect-free crystal during multiple cycles of oxidation treatment.

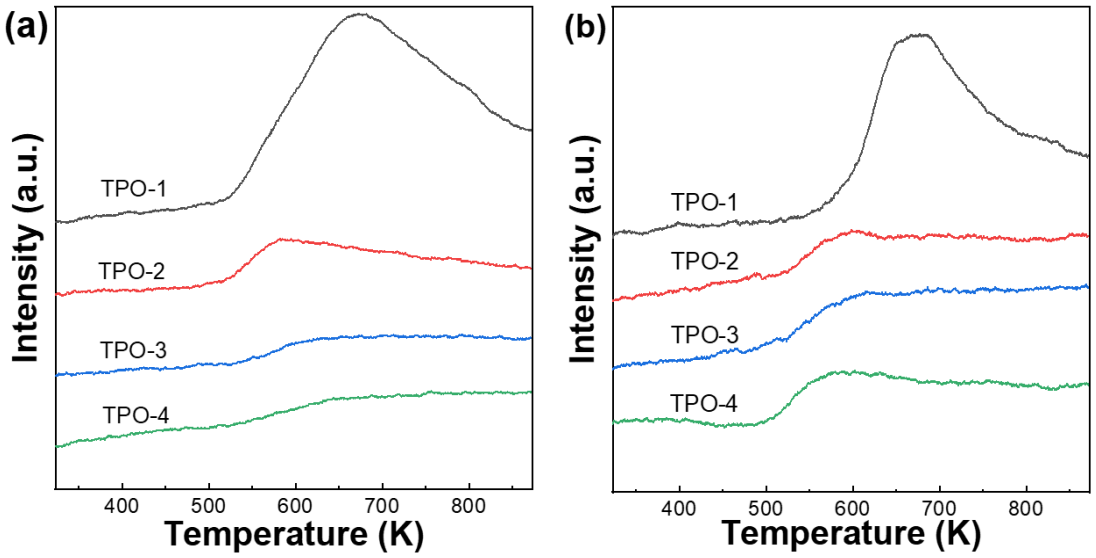

Figure 4.9 Successive O_2-TPO profiles of (a) TiO_2 and (b) TiO_2-LE4 samples. (Before and between the TPO measurement, sample was pretreated at 553 K in N_2 flow (50 mL/min) for 4 h.)

4.3.4 Metal-support interaction in laser-treated TiO_2 supported Pt catalysts

The characterizations for laser-engraved TiO_2 samples show that defective TiO_2 has great reducibility and redox capability. How do these properties affect the supported metal catalysts since TiO_2 is often used as the catalyst support in thermal catalysis? To answer this question, we loaded Pt species onto the TiO_2 supports and studied the properties of Pt/TiO_2 catalysts. Figure 4.10a-c showed the representative HAADF-STEM images of Pt/TiO_2 and Pt/TiO_2-LE samples, in which the Pt concentration was controlled at 0.50wt%. The Pt species were evenly dispersed on the TiO_2 supports before and after laser engraving treatment. No obvious particle

aggregates or large particles were observed from these images. The Pt particle size distribution histograms of the Pt/TiO_2 samples were analyzed from the STEM images. Figures 4.10d-f show the particle sizes range from 1.175 nm for Pt/TiO_2 sample, to 0.955 nm for Pt/TiO_2-LE1, and to 1.201 nm for Pt/TiO_2-LE4. Due to the resolution cutoff (~0.40 nm) of the STEM instrument, the single atoms and dimers were not included in the size distribution analysis. It should be noted that the surface areas of these samples were very different due to the laser treatment. With the same Pt loading, the sample with a smaller surface area is supposed to have a lower Pt dispersion and larger particle sizes. The comparable Pt particles sizes on these three TiO_2 support samples in Figure 9 suggest that the metal-support interaction in the TiO_2-LE supports should be stronger than the pristine TiO_2 support. The defects created by the laser engraving could act as trapping sites to promote Pt dispersion against clustering or aggregation, even the surface areas of the TiO_2-LE supports are lower. Previous studies have shown that metal species prefer to nucleate on the oxygen vacancies sites in the reducible metal oxide support that yields stronger metal-support interanction.[71, 189]

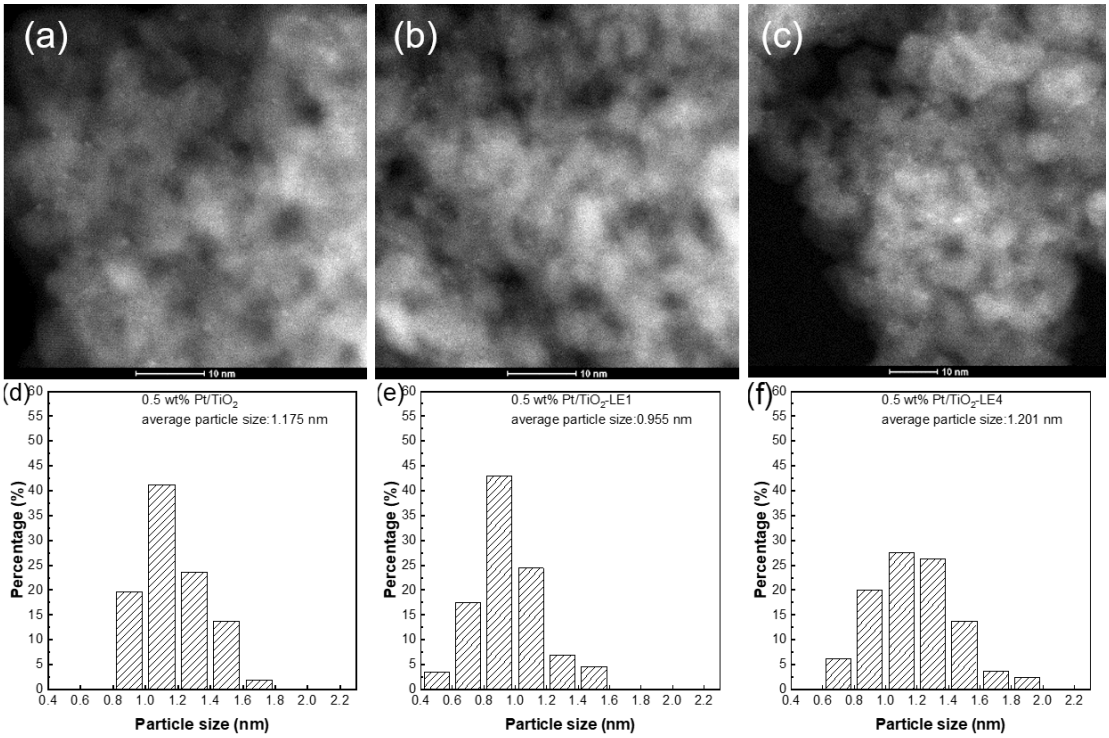

Figure 4.10 HAADF-STEM images of 0.50wt% Pt/TiO_2 catalysts with (a) TiO_2, (b) TiO_2-LE1 and (c) TiO_2-LE4 support, respectively. (d)-(f) show the corresponding Pt particle size distribution histograms accordingly.

The bonding environment of Pt species in 0.5wt% /TiO_2 and 0.5wt% Pt/TiO_2-LE samples were examined by the XPS spectra. Figure 4.11 shows that the Pt 4f spectra in both samples in the 77 - 70 eV binding energy range. The spectra were calibrated to C 1s peak at 284.8 eV. It should be noted that the Ti 3s line has a satellite peak presents in the 70-80 eV binding energy range that overlaps with the Pt 4f XPS spectra, which should be subtracted to obtain precise Pt 4f peaks.[116] For this purpose, the XPS

spectrum of pure TiO_2 support was recorded under the same measurement conditions. After the intensity of the background line is normalized by the Ti 3s line recorded for the Pt/TiO_2 catalysts and pure TiO_2 support, we subtracted the contribution of the lines from the TiO_2 support within the Pt4f XPS peak region in our analysis. The Pt $4f_{7/2}$ peak shifts from 71.3 eV of 0.5 wt.% Pt/TiO_2 sample to 71.8 eV for the 0.5 wt.% Pt/TiO_2-LE4 sample. The blue-shift of the peak indicates Pt species is more electron deficient on the TiO_2-LE4 support. Due to the charge transfer to the support, isolated Pt single atoms on metal oxide have been reported to be cationic.[20] Similarly, small Pt clusters appear to be electron deficient because of the intimate interaction between their two-dimensional flat structure and the support.[113, 114] The defective structure and improved redox ability of the laser-engraved TiO_2 support likely induce more cationic Pt species than that of the pristine Pt/TiO_2 catalyst. With creating defects in the TiO_2 support, this apparently strengthened the metal-support interaction and thus created more cationic Pt species.

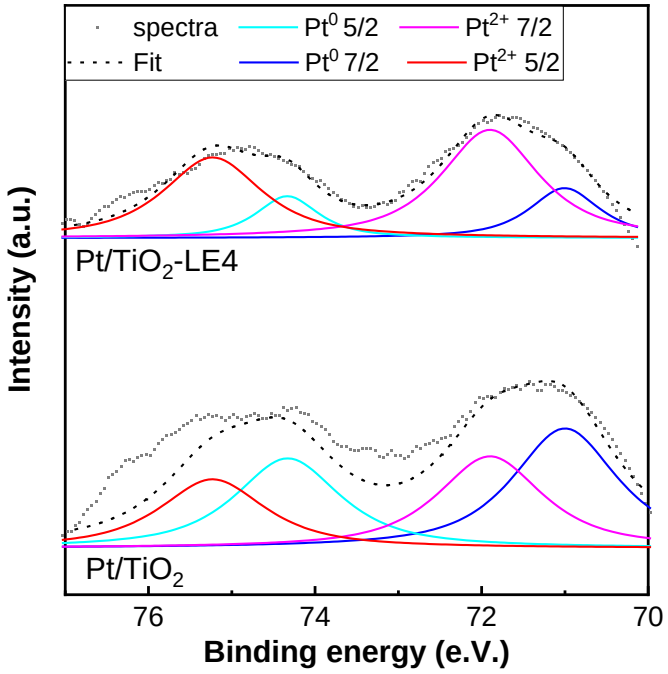

Figure 4.11 XPS spectra of Pt 4f of 0.50wt% Pt/TiO_2 and Pt/TiO_2-LE4 samples. The spectra were calibrated with C1s of adventurous carbon species at 284.8 eV. (80% Lorentzian-Gaussian peak deconvolution was done using XPSPEAK41.)

We deconvoluted Pt $4f_{7/2}$ region into Pt^{2+} (72.2 eV) and Pt^0 (71.1 eV) peaks to quantitively understand the electronic state changes of Pt on the TiO_2 supports. The cationic Pt component has increased from 43.4% in the Pt/TiO_2 catalyst to 75.1% in the Pt/TiO_2-LE4 sample. The increase of cationic Pt would be correlated with the Pt of higher dispersion or strong metal-support interaction. Since both samples have the similar particle sizes, it could be inferred that the stronger metal support interaction is the dominant cause for the increased oxidation state of supported Pt species.[86] The interfacial charge transfer was also studied by computational modeling of the wave

function of Pt cluster on TiO_2 support. As shown in Figure 4.12**,** the charge transfer from Pt to TiO_2 support with oxygen vacancy was more significant than that of Pt and pristane TiO_2. This enhanced charge transfer supported the cationic Pt property concluded from XPS experiment, and further suggested a stronger electronic metal support interaction in the Pt/TiO_2-LE catalysts.

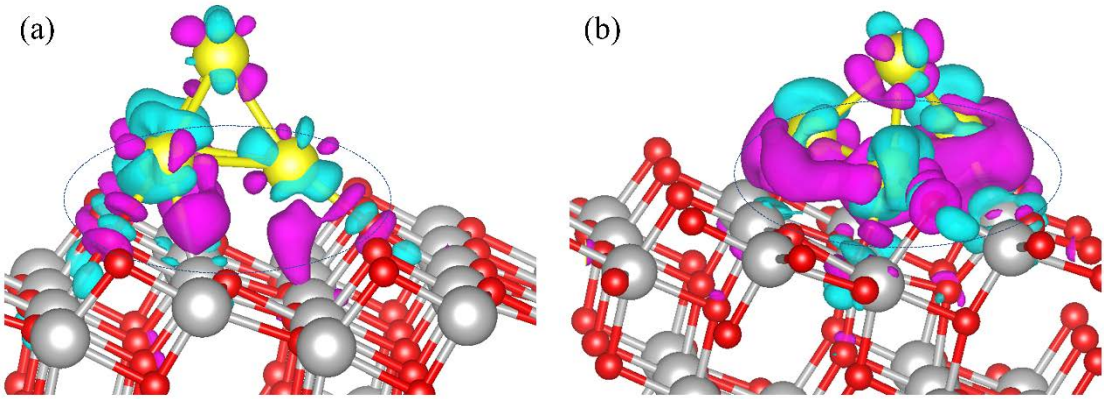

Figure 4.12. The differential charge densities of (a) Pt_4 cluster on clean anatase TiO_2 (101) surface and (b) Pt_4 cluster on anatase TiO_2 (101) surface with an O vacancy. (Ti in grey, O in red, and Pt in yellow; positive charge density in magenta, negative charge density in cyan, isosurface level: 0.005 e/Bohr3).

H_2-TPR profiles were recorded to investigate the reducibility of supported Pt species, which reflects the interaction between metal and TiO_2 support. Figure 4.13 shows that the Pt/TiO_2 sample has four reduction peaks centered at 424 K, 460 K, 664 K and 975 K. The first three peaks were assigned to the reduction of surface species: the reduction of amorphous PtO_x species, reduction of Pt–TiO_x interface sites and reduction of the surface oxygen on the TiO_2 support by spillover hydrogen from Pt site,

in sequence.[190] The last peak at ~973 K was related to the reduction of bulk oxygen of TiO_2. The H_2-TPR profiles of Pt/TiO_2-LE1 and Pt/TiO_2-LE4 also have three surface reduction peaks, but these three peaks shifted to slight lower temperatures. For example, the peak assigned to the reduction of PtO_x species was shifted to 400 K, 24 K lower than that of PtO_x on the TiO_2 support. The STEM imaging analysis (Figure 4.10) shows that the Pt particle size did not change on TiO_2-LE support. The easy reduction of PtO_x species could be caused by the easy reduction and redox capability of the laser-treated TiO_2 support. Similarly, the intermediate temperature peak assigned to the Pt–TiO_x interface sites shifted from 460 K to 453 K. This second surface reduction peaks in the laser-engraved samples have also become broader. Since the second reduction peak was caused by the strong interaction of Pt with reduced Ti^{3+} sites, the broadening of this peak indicated stronger interactions with the laser-engraved support.[191, 192] The last reduction peak of the laser-engraved samples showed decreased intensity and a shift towards lower temperature. The reduction of rutile was easier than anatase which caused the bulk reduction peak to move to lower temperature and gradually joined the shoulder peak of anatase phase surface reduction at 785 K.

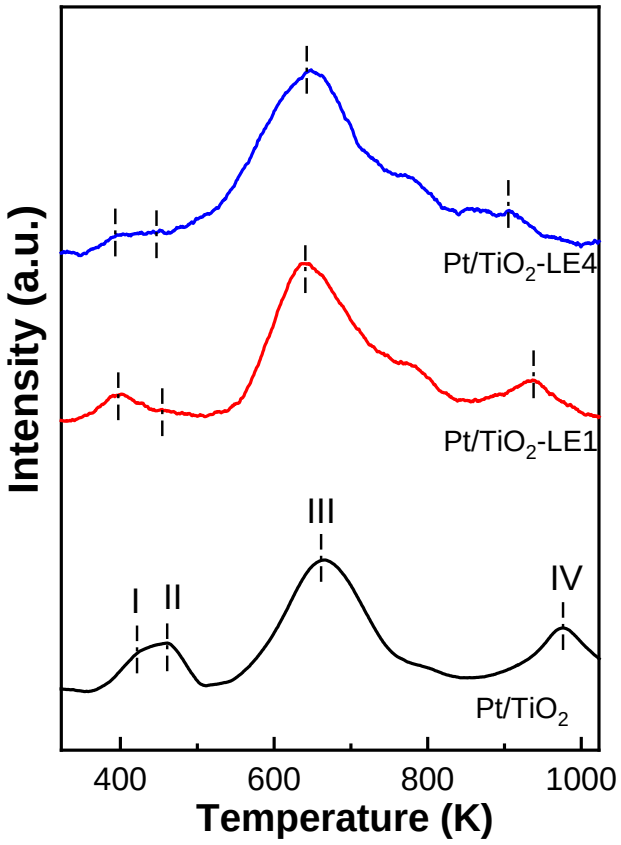

Figure 4.13. H_2-TPR profiles of 0.50wt% Pt/TiO_2, 0.50wt% Pt/TiO_2-LE1 and 0.50wt% Pt/TiO_2-LE4 samples, respectively.

4.3.5 Catalytic performance of Pt/TiO_2 catalysts in hydrogenation

The catalytic performance of Pt/TiO_2 and Pt/TiO_2-LE catalysts was tested by probe reaction of hydrogenation of 3-nitrostyrene (3-NS) to 3-vinylanilline (3-VA). The reaction can take place either through hydrogenation of the nitro ($-NO_2$) group to form 3-vinylaniline (3-VA) or via the hydrogenation of the vinyl group ($-CH=CH_2$) towards 3-ethylnitrobenzene (3-ENB). The over-hydrogenation, i.e., hydrogenation of

both -NO_2 and -$CH=CH_2$ groups, leads to formation of the final 3-ethylaniline (3-EA) product. Due to the high sensitivity of hydrogenation of C=C double bond in the -$CH=CH_2$ group to the particle sizes of supported metal catalysts, the chemoselective hydrogenation of the -NO_2 group in 3-NS has been explored by employing supported metal catalysts with reducing metal particle sizes (e.g., down to small metal clusters or single atoms)[193] and/or tuning the metal-support interactions by employing different metal-support pairs[194]. It has been reported that the absence of Pt-Pt metallic bonding and presence of positively charged isolated Pt single atoms or nanoclusters favor the preferential adsorption of -NO_2 groups, and thus enhance the chemoselectivity.[86]

Figure 4.14a shows the conversion and product formation rates in hydrogenation of 3-NS over Pt/TiO_2, Pt/TiO_2-LE1 and Pt/TiO_2-LE4 catalysts. In comparison to the pristine Pt/TiO_2, the Pt/TiO_2-LE1 catalyst showed comparable conversion but higher 3-VA production rate. The Pt/TiO_2-LE4 catalyst has much significant high activity, showing 19% conversion enhancement and ~4 times higher 3-VA production rate. Since all these three Pt/TiO_2 catalysts have comparable Pt sizes, the higher activity and better selectivity towards 3-VA over the Pt/TiO2-LE catalysts are not likely caused by the Pt particle size effects. Instead, the metal-support interaction that favors the charge transfer from Pt to TiO_2 support might be the dominating factor. The great redox capability of the TiO_2-LE support and the resulted more cationic Pt species could be responsible for the enhancement in the observed catalytic performances. The polar nitro (-NO_2) group of 3-NS preferentially adsorbs on the cationic Pt site compared to nonpolar vinyl (-C=C) group.[195-197] Previous studies

have shown that inducing SMSI in Pt/TiO_2 catalysts by high temperature reduction treatment could yield higher conversion and 3-vinylanillin (3-VA) selectivity.[86, 198]

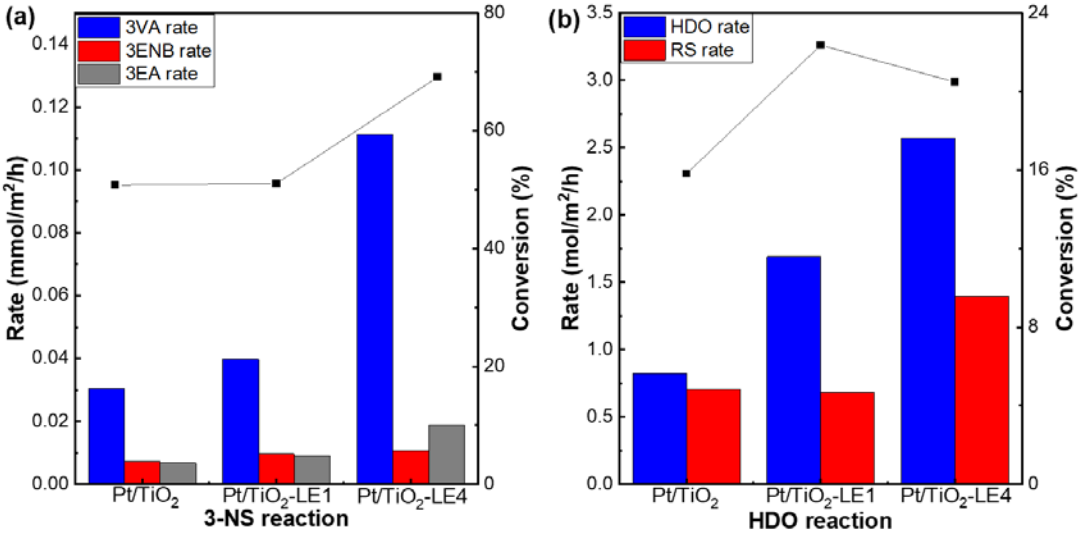

Figure 4.14. Conversion and reaction rate of hydrogenation of 3-NS (a) and FA (b) over Pt/TiO_2, Pt/TiO_2-LE1 and Pt/TiO_2-LE4 catalysts. (0.50wt%Pt in each catalyst; 3-NS reaction: 313 K, 3 bar H_2, 10 mL ethanol, 0.02 g catalyst, 0.076 g 3-NS, 1.5 h; FA reaction: 443 K, 11 bar H_2 + 7 bar N_2, 10 mL 2-propanol, 0.05 g catalyst, 0.10 g furfuryl alcohol, 8 h)

Hydrogenation of furfural alcohol (FA) was used as the second probe reaction to test the catalytic performance of the laser-engraved TiO_2 supported Pt catalysts. The reaction involves multiple reaction pathways, among which the desired one is the hydrodeoxygenation (HDO) where the C-OH bond of FA is selectively cleaved to form 2-methylfuran product; and the ring saturation (RS) of C=C in furan ring to generate

2-methyltetrahydrofuran etc. As reported by Vlachos group[111], the HDO reaction was favored on the ultra-low loading Pt/TiO_2 catalysts that contain isolated Pt single atoms or small clusters. It was proposed that the Pt atoms in direct contact with the oxide support was the most active centers of HDO reaction, followed by the metallic Pt from nanoparticle centers which however catalyzes ring saturation reaction simultaneously. Mechanism studies for FA hydrogenation have shown that surface oxygen vacancies generated by hydrogen are the active centers in the course of the reaction.[199]

Figure 4.14b shows the reaction rate of HDO increased from 0.822 $mol/m^2/h$ of Pt/TiO_2 to 1.690 $mol/m^2/h$ of Pt/TiO_2-LE1 catalyst, while the undesired RS reaction rate decreased from 0.703 $mol/m^2/h$ to 0.683 $mol/m^2/h$. The suppression of RS could be due to the stronger metal support interaction in Pt/TiO_2-LE catalyst. As the laser treatment cycle increased, the HDO reaction rate continued to increase. The Pt/TiO_2-LE4 catalyst showed nearly 4 times enhancement of the HDO rate compared to Pt/TiO_2 catalyst without laser treatment on the support. Similar to the hydrogenation of 3-NS, the reactivity and HDO selectivity enhancements in hydrogenation of FA could also be caused by the laser-engraved defects in TiO_2 support which result in high reducibility and redox capability of the Pt/TiO_2 catalysts.

5.4 Conclusion of Chapter 4

In summary, we employed a laser engraving method to create defects in an anatase TiO_2 sample and studied the physicochemical properties of the resultant

defective TiO_2 substrates. The combinational characterizations show that the laser-engraving treatment increased the particle sizes and introduced rutile phase into the anatase TiO_2. It also created defects such as oxygen vacancy and Ti^{3+} state that reduced the band gap and enhanced the light absorption in the visible region of the DR UV-vis spectrum. The defects in the laser-engraved TiO_2 substrate are stable, enabling the defective TiO_2 with great reducibility and redox capability. The influence of laser engraved TiO_2 on the supported metal catalysts was studied by Pt/TiO_2-LE catalysts. In composition to the pristine Pt/TiO_2 catalyst, the Pt/TiO_2-LE catalysts have comparable Pt sizes although the latter TiO_2 supports have lower surface areas. This suggests a higher Pt dispersion and stronger metal-support interaction exist in the defective TiO_2 support that could favor charge transfer from Pt clusters to the defective support. The catalytic performance of Pt/TiO2-LE catalysts was probed by the hydrogenation of 3-nitrostyrene and furfural alcohol. In 3-nirostyrene hydrogenation reaction, the Pt/TiO_2-LE catalysts with strong metal-support interaction yielded higher activity in chemoselective hydrogenation of the -NO_2 group in 3-NS. Similarly, the laser engraved TiO2 supported Pt catalyst showed a higher activity in HDO of FA towards C-O bond scission of furfuryl alcohol to yield 2-methylfuran product. reaction, the enhanced reducibility of support by laser treatment accelerated the. The undesired side reaction pathways were suppressed by the strong metal support interaction between supported Pt and laser-engraved support. The laser engraving method is simple and flexible to operate, which can be generally applied to other metal oxides or

metal oxide supported metal catalysts to engineer their defects to develop advanced catalyst materials.

Chapter 5: Conclusions and future work

5.1 Conclusions

To achieve high specific activity and product selectivity in heterogeneous catalysis, supported metal catalysts with uniformly small metal sites are desired. However, with the continue downsizing of metal particle to metal clusters or even single atoms, the highly dispersed metal species show significant changes in catalytic properties from the bulk metal crystal. The effective anchoring of these ultra-small metal particles on the support surface is also a challenge due to the high aggregation tendency caused by elevated surface free energy. The synthesis and characterization of high dispersion catalysts have become the major focus in the development of novel catalyst with high atomic efficiency. As the metal dispersion increases, more metal-support interfacial sites would be formed, which causes the catalytic properties of high dispersion catalyst more subject to the metal-support interaction. Therefore, deeper understanding of metal-support interactions will also benefit the study of high dispersion catalyst. This dissertation was focused on the synthesis and characterization of high dispersion catalyst and how the synthesis parameters/support properties affect the interaction between metal and support. The effect of the interaction were studied by the hydrogenation reaction of different molecules.

Supported metal catalysts often consist of a mixture of metal sites ranging from nanoparticles to subnanometer clusters and single atoms. It remains a necessity to uniquely differentiate these sites and their activities to guide the design of optimal

catalysts. However, the characterization of these highly dispersed metal species is extremely demanding due to the ultra-small size of these metal particles. Chapter 2 introduced a simple method to assess the distribution of metal active site structures in heterogeneous sample which utilized the structure sensitivity of styrene hydrogenation over titania supported platinum (Pt) catalysts. The results showed that nanometer-sized Pt clusters have significantly higher activity than Pt nanoparticles, sub-nanometer clusters or isolated Pt single atoms. The relationship between activity and geometric/electronic properties of Pt sites influenced by particle sizes was developed. Similar volcano-shaped trend has been observed in catalysts with other support material, which suggests that this correlation has the potential be used to pre-screen supported Pt catalysts with other type of support materials.

Strong metal-support interaction (SMSI) has been found to have significant impact on the geometric and electronic properties of supported catalysts. Numerous studies have been dedicated to studying how to tune the strong metal support interaction to enhance the catalytic activity, selectivity, and stability of heterogeneous catalysts. Chapter 3 discussed a new method to introduce strong metal-support interaction during the wetness impregnation process by solution pH control. Compared to the traditional approach to induce SMSI by reduction-oxidation cycle, this wet chemistry method is less demanding with respect to both energy and environment requirement. The SMSI between Pt nanoparticles and TiO_2 support caused significant catalytic performance change in styrene hydrogenation and 3-nitrostyrene selective hydrogenation. This

method could be used to induce and tune the SMSI effect in supported catalysts to achieve excellent catalytic activity and selectivity.

Defect engineering has been extensively employed to control the structural, optical, and electronic properties of catalysts via synthesis or post-synthesis modification approach. Chapter 4 described laser engraving method for creating high dispersion catalyst Pt/TiO_2 catalyst and studied how the defect created by laser treatment affect the metal support interaction of the synthesized catalyst. The laser engraving treatment on anatase TiO_2 material caused changes in its structure and physicochemical property as well as the properties of TiO_2 supported platinum catalyst. The laser engraving enlarged the particle size, formed rutile phase and created defects in TiO_2, which induced band gap change and visible light absorption enhancement. The defects created by laser engraving are stable than those existed in the pristine TiO_2 or created by high temperature annealing in reducible hydrogen atmosphere. The resultant defective TiO_2 material by this laser treatment method has stable and superior redox property. The strength of metal-support interaction in the defective TiO_2 supported Pt catalyst was modified from that of the pristine Pt/TiO_2 catalyst, which enabled higher reactivity and selectivity in hydrogenation of 3-nitrostyrene and furfuryl alcohol. This work provides understanding of material property and catalysis performance of laser treated catalysts in thermal catalysis.

5.2 Future work

5.2.1 Expansion to metal oxide supports with various reducibility

The interaction between metal and support strongly depends on the reducibility of the support material.[200] We believe that harsh treatment on support including using corrosive solution during wetness impregnation and laser engraving have the potential to become a general method to tune the metal-support interaction. These methods could be used to explore beyond our current Pt/TiO_2 system. For the metal species on highly dispersed catalysts, precious metals (Pd, Rh, Au, Ir, Ag, etc.) and low-cost metals (Fe, Co, Ni, etc.) could be employed. Besides mildly reducible TiO_2, metal oxide with various reducibility from highly reducible CeO_2 and Fe_2O_3, reducible SnO_2 and Eu_2O_3, and irreducible Y_2O_3 and Al_2O_3 could be used as supports.[201]

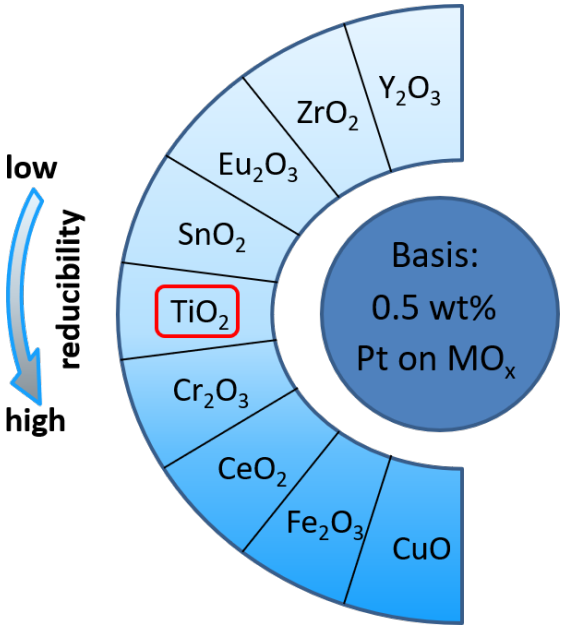

Figure 5.1. Metal oxide (MOX) spectrum with increasing reducibility.

Although SMSI has been reported mostly between group VIII metal and reducible metal oxide support, with the change on support surface properties and the introduction of defect, SMSI could also occur on support that were irreducible. Pt on different metal oxide could be to study the effect of SMSI on the metal aggregation since the stability of single atom and ultrasmall cluster strongly depends on the bond strength between metal and support. Besides the effect on metal dispersion, the charge redistribution between metal and different support could result in electronic property change that would alter the metal-adsorbate bond and affect the catalytic activity and selectivity in reaction. By introducing SMSI into different catalyst systems and adjusting the interaction strength, the most effective catalyst for desired reactions could

be constructed and the mechanistic understanding of the catalyst functionality could be achieved.

5.2.2 Extend the styrene hydrogenation probe reaction by decoupling the electronic and geometric effect of Pt catalyst

With the relationship established between the Pt aggregation state and styrene hydrogenation activity, the fast screening of metal aggregation state in supported catalyst has become possible. However, it would be even better if the relationship could be further extended to other supported catalyst systems. The electronic and geometric properties of metal active species are generally coupled together due to the charge redistribution at the metal support interface. The decoupling of the electronic and geometric properties is the key challenge of applying this relationship to other systems. Recently Wang et al. reported a method to decouple these effects by a novel orthogonal decomposition method.[202] Their study on supported Pt catalysts synthesized by particle size and shape control indicated that the degree of electron transfer between Pt nanoparticles of similar size and shape and supports was positively correlated with the work function (W_f) of support, and were independent with the particle size of Pt. The distinctions of Fermi levels of support and supported Pt nanoparticles had significant impacts on the reaction activity and selectivity. By acquiring the work function of support materials by either experimental or computational approach, we could apply this correction on the electronic properties of Pt species supported on other materials

while retaining their geometric properties. Similar volcano-shaped trend of hydrogenation activity would be expected for catalysts with different Pt size on other support materials, however the deviation on the absolute activity value of Pt/TiO_2 system could be determined by the work function of the support material.

5.2.3 High dispersion catalyst synthesis by laser powder bed fusion (L-PBF)

Due to the low thermal conductivity of metal oxide materials, the laser engraving and laser thermal shock method discussed in chapter 4 were limited by the uneven temperature distribution across the thickness of the sample pellet. The main challenge of laser treatment of the metal oxide support is how to allow laser power to penetrate the entire treatment region. Addictive manufacturing technique has drowned great attention and widely used in the manufacturing of industrial metallic components.

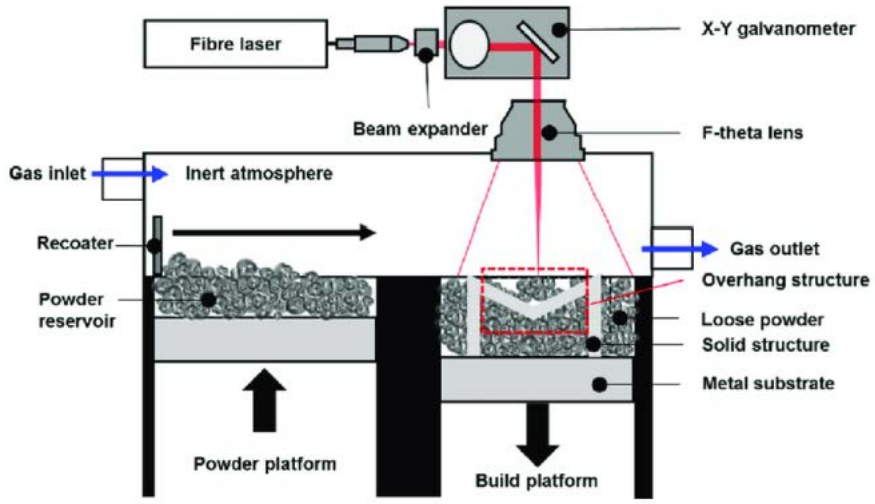

Figure 5.2. Scheme of laser powder bed fusion process.

Among the addictive manufacturing techniques, laser powder bed fusion (L-PBF) processes utilize laser to precisely sinter the metal powder and are currently able to produce metal parts with complex features.[203] During the laser powder bed fusion process, thin layers of atomized sample powder are evenly distributed using a re-coating mechanism onto a substrate plate that is fastened to an indexing platform that can move in the vertical direction (Z direction). The laser beam is directed in the X and Y directions with scanning mirrors with intense laser energy to permit full melting or fusion of the particles to form a solid structure, which is similar to the laser engraving method discussed in previous chapter. These processes are repeated layer after layer until the part is complete. This L-PBF could be adapted in the synthesis of defect stabilized high dispersion catalysts because with it has the ability to treat powder layer by layer which overcomes the thermal conductivity issue along the Z direction. With the laser selective sintering, the nucleation process of metal atoms could be controlled by the ultra-fast kinetics of laser heating and cooling, defects could be created simultaneously to stabilize the highly dispersed metal species. Since L-PBF technique can continuously treat powder materials with high speed (up to 50mL per hour), this method has great potential to the mass production of high dispersion catalyst for industry.

Bibliography

1. Sherrington, D. C.; Kybett, A. P., *Supported catalysts and their applications*. Royal Society of Chemistry: 2007.
2. Endo, K.; Nakamura, K.; Katayama, Y.; Miura, T., Pt–Me (Me= Ir, Ru, Ni) binary alloys as an ammonia oxidation anode. *Electrochimica Acta* **2004,** *49* (15), 2503-2509.
3. Boggs, B. K.; Botte, G. G., Optimization of Pt–Ir on carbon fiber paper for the electro-oxidation of ammonia in alkaline media. *Electrochimica Acta* **2010,** *55* (19), 5287-5293.
4. Wang, X.; Kong, Q.; Han, Y.; Tang, Y.; Wang, X.; Huang, X.; Lu, T., Construction of Ir-Co/C nanocomposites and their application in ammonia oxidation reaction. *Journal of Electroanalytical Chemistry* **2019,** *838*, 101-106.
5. Li, L.; Zhang, N.; Wu, R.; Song, L.; Zhang, G.; He, H., Comparative study of moisture-treated Pd@ CeO2/Al2O3 and Pd/CeO2/Al2O3 catalysts for automobile exhaust emission reactions: effect of core–shell interface. *ACS Applied Materials & Interfaces* **2020,** *12* (9), 10350-10358.
6. Lu, Y.; Zhang, Z.; Lin, F.; Wang, H.; Wang, Y., Single‐atom automobile exhaust catalysts. *ChemNanoMat* **2020,** *6* (12), 1659-1682.
7. Tejeda-Serrano, M.; Mon, M.; Ross, B.; Gonell, F.; Ferrando-Soria, J. s.; Corma, A.; Leyva-Pérez, A.; Armentano, D.; Pardo, E., Isolated Fe (III)–O sites catalyze the hydrogenation of acetylene in ethylene flows under front-end industrial conditions. *Journal of the American Chemical Society* **2018,** *140* (28), 8827-8832.
8. Nakaya, Y.; Hirayama, J.; Yamazoe, S.; Shimizu, K.-i.; Furukawa, S., Single-atom Pt in intermetallics as an ultrastable and selective catalyst for propane dehydrogenation. *Nature communications* **2020,** *11* (1), 1-7.
9. Sun, Q.; Wang, N.; Fan, Q.; Zeng, L.; Mayoral, A.; Miao, S.; Yang, R.; Jiang, Z.; Zhou, W.; Zhang, J., Subnanometer bimetallic platinum–zinc clusters in zeolites for propane dehydrogenation. *Angewandte Chemie* **2020,** *132* (44), 19618-19627.
10. Hellinger, M.; Carvalho, H. W.; Baier, S.; Wang, D.; Kleist, W.; Grunwaldt, J.-D., Catalytic hydrodeoxygenation of guaiacol over platinum supported on metal oxides and zeolites. *Applied Catalysis A: General* **2015,** *490*, 181-192.
11. Liu, X.; Jia, W.; Xu, G.; Zhang, Y.; Fu, Y., Selective hydrodeoxygenation of lignin-derived phenols to cyclohexanols over Co-based catalysts. *ACS Sustainable Chemistry & Engineering* **2017,** *5* (10), 8594-8601.
12. Ogo, S.; Okuno, Y.; Sekine, H.; Manabe, S.; Yabe, T.; Onda, A.; Sekine, Y., Low‐Temperature Direct Catalytic Hydrothermal Conversion of Biomass Cellulose to Light Hydrocarbons over Pt/Zeolite Catalysts. *ChemistrySelect* **2017,** *2* (22), 6201-6205.

13. Bus, E.; Prins, R.; van Bokhoven, J. A., Origin of the cluster-size effect in the hydrogenation of cinnamaldehyde over supported Au catalysts. *Catalysis Communications* **2007,** *8* (9), 1397-1402.
14. Neri, G.; Musolino, M. G.; Milone, C.; Pietropaolo, D.; Galvagno, S., Particle size effect in the catalytic hydrogenation of 2, 4-dinitrotoluene over Pd/C catalysts. *Applied Catalysis A: General* **2001,** *208* (1-2), 307-316.
15. Markov, P. V.; Mashkovsky, I. S.; Bragina, G. O.; Wärnå, J.; Gerasimov, E. Y.; Bukhtiyarov, V. I.; Stakheev, A. Y.; Murzin, D. Y., Particle size effect in liquid-phase hydrogenation of phenylacetylene over Pd catalysts: Experimental data and theoretical analysis. *Chemical Engineering Journal* **2019,** *358*, 520-530.
16. Hansen, T. W.; DeLaRiva, A. T.; Challa, S. R.; Datye, A. K., Sintering of catalytic nanoparticles: particle migration or Ostwald ripening? *Accounts of chemical research* **2013,** *46* (8), 1720-1730.
17. Kwak, J. H.; Hu, J.; Mei, D.; Yi, C.-W.; Kim, D. H.; Peden, C. H. F.; Allard, L. F.; Szanyi, J., Coordinatively Unsaturated Al³⁺ Centers as Binding Sites for Active Catalyst Phases of Platinum on γ-Al₂O₃. *Science* **2009,** *325* (5948), 1670-1673.
18. Yang, M.; Li, S.; Wang, Y.; Herron, J. A.; Xu, Y.; Allard, L. F.; Lee, S.; Huang, J.; Mavrikakis, M.; Flytzani-Stephanopoulos, M., Catalytically active Au-O(OH)_x- species stabilized by alkali ions on zeolites and mesoporous oxides. *Science* **2014,** *346* (6216), 1498-1501.
19. Yang, X.-F.; Wang, A.; Qiao, B.; Li, J.; Liu, J.; Zhang, T., Single-atom catalysts: a new frontier in heterogeneous catalysis. *Accounts of chemical research* **2013,** *46* (8), 1740-1748.
20. Qiao, B.; Wang, A.; Yang, X.; Allard, L. F.; Jiang, Z.; Cui, Y.; Liu, J.; Li, J.; Zhang, T., Single-atom catalysis of CO oxidation using Pt 1/FeO x. *Nature chemistry* **2011,** *3* (8), 634-641.
21. DeRita, L.; Dai, S.; Lopez-Zepeda, K.; Pham, N.; Graham, G. W.; Pan, X.; Christopher, P., Catalyst architecture for stable single atom dispersion enables site-specific spectroscopic and reactivity measurements of CO adsorbed to Pt atoms, oxidized Pt clusters, and metallic Pt clusters on TiO2. *Journal of the American Chemical Society* **2017,** *139* (40), 14150-14165.
22. Zhai, Y.; Pierre, D.; Si, R.; Deng, W.; Ferrin, P.; Nilekar, A. U.; Peng, G.; Herron, J. A.; Bell, D. C.; Saltsburg, H., Alkali-stabilized Pt-OH x species catalyze low-temperature water-gas shift reactions. *Science* **2010,** *329* (5999), 1633-1636.
23. Liu, P.; Zhao, Y.; Qin, R.; Mo, S.; Chen, G.; Gu, L.; Chevrier, D. M.; Zhang, P.; Guo, Q.; Zang, D., Photochemical route for synthesizing atomically dispersed palladium catalysts. *Science* **2016,** *352* (6287), 797-800.
24. Zhou, X.; Hwang, I.; Tomanec, O.; Fehn, D.; Mazare, A.; Zboril, R.; Meyer, K.; Schmuki, P., Advanced Photocatalysts: Pinning Single Atom Co‐Catalysts on Titania Nanotubes. *Advanced Functional Materials* **2021,** *31* (30), 2102843.
25. Hejazi, S.; Mohajernia, S.; Osuagwu, B.; Zoppellaro, G.; Andryskova, P.; Tomanec, O.; Kment, S.; Zbořil, R.; Schmuki, P., On the controlled loading of single

platinum atoms as a Co ‐ catalyst on TiO2 anatase for optimized photocatalytic H2 generation. *Advanced Materials* **2020,** *32* (16), 1908505.
26. Liu, L.; Diaz, U.; Arenal, R.; Agostini, G.; Concepcion, P.; Corma, A., Generation of subnanometric platinum with high stability during transformation of a 2D zeolite into 3D. *Nature materials* **2017,** *16* (1), 132-138.
27. Chen, Y.; Ji, S.; Wang, Y.; Dong, J.; Chen, W.; Li, Z.; Shen, R.; Zheng, L.; Zhuang, Z.; Wang, D., Isolated single iron atoms anchored on N ‐ doped porous carbon as an efficient electrocatalyst for the oxygen reduction reaction. *Angewandte Chemie* **2017,** *129* (24), 7041-7045.
28. McCluskey, M. D.; Janotti, A., Defects in Semiconductors. AIP Publishing LLC: 2020; Vol. 127, p 190401.
29. Ohno, T.; Mitsui, T.; Matsumura, M., Photocatalytic activity of S-doped TiO2 photocatalyst under visible light. *Chemistry letters* **2003,** *32* (4), 364-365.
30. Dvoranova, D.; Brezova, V.; Mazúr, M.; Malati, M. A., Investigations of metal-doped titanium dioxide photocatalysts. *Applied Catalysis B: Environmental* **2002,** *37* (2), 91-105.
31. Yan, J.; Wang, T.; Wu, G.; Dai, W.; Guan, N.; Li, L.; Gong, J., Tungsten oxide single crystal nanosheets for enhanced multichannel solar light harvesting. *Advanced Materials* **2015,** *27* (9), 1580-1586.
32. Zimbone, M.; Buccheri, M.; Cacciato, G.; Sanz, R.; Rappazzo, G.; Boninelli, S.; Reitano, R.; Romano, L.; Privitera, V.; Grimaldi, M., Photocatalytical and antibacterial activity of TiO2 nanoparticles obtained by laser ablation in water. *Applied Catalysis B: Environmental* **2015,** *165*, 487-494.
33. He, J.; Li, N.; Li, Z. G.; Zhong, M.; Fu, Z. X.; Liu, M.; Yin, J. C.; Shen, Z.; Li, W.; Zhang, J., Strategic Defect Engineering of Metal ‐ Organic Frameworks for Optimizing the Fabrication of Single ‐ Atom Catalysts. *Advanced Functional Materials* **2021,** *31* (41), 2103597.
34. Zhang, J.; Wu, X.; Cheong, W.-C.; Chen, W.; Lin, R.; Li, J.; Zheng, L.; Yan, W.; Gu, L.; Chen, C., Cation vacancy stabilization of single-atomic-site Pt1/Ni (OH) x catalyst for diboration of alkynes and alkenes. *Nature communications* **2018,** *9* (1), 1-8.
35. Chang, T.-Y.; Tanaka, Y.; Ishikawa, R.; Toyoura, K.; Matsunaga, K.; Ikuhara, Y.; Shibata, N., Direct imaging of Pt single atoms adsorbed on TiO2 (110) surfaces. *Nano letters* **2014,** *14* (1), 134-138.
36. Marcinkowski, M. D.; Darby, M. T.; Liu, J.; Wimble, J. M.; Lucci, F. R.; Lee, S.; Michaelides, A.; Flytzani-Stephanopoulos, M.; Stamatakis, M.; Sykes, E. C. H., Pt/Cu single-atom alloys as coke-resistant catalysts for efficient C–H activation. *Nature chemistry* **2018,** *10* (3), 325-332.
37. Nie, L.; Mei, D.; Xiong, H.; Peng, B.; Ren, Z.; Hernandez, X. I. P.; DeLaRiva, A.; Wang, M.; Engelhard, M. H.; Kovarik, L., Activation of surface lattice oxygen in single-atom Pt/CeO2 for low-temperature CO oxidation. *Science* **2017,** *358* (6369), 1419-1423.

38. Ren, Y.; Tang, Y.; Zhang, L.; Liu, X.; Li, L.; Miao, S.; Sheng Su, D.; Wang, A.; Li, J.; Zhang, T., Unraveling the coordination structure-performance relationship in Pt1/Fe2O3 single-atom catalyst. *Nature communications* **2019,** *10* (1), 1-9.
39. Liu, J.; Jiao, M.; Lu, L.; Barkholtz, H. M.; Li, Y.; Wang, Y.; Jiang, L.; Wu, Z.; Liu, D.-j.; Zhuang, L., High performance platinum single atom electrocatalyst for oxygen reduction reaction. *Nature communications* **2017,** *8* (1), 1-10.
40. Liu, J.; Lucci, F. R.; Yang, M.; Lee, S.; Marcinkowski, M. D.; Therrien, A. J.; Williams, C. T.; Sykes, E. C. H.; Flytzani-Stephanopoulos, M., Tackling CO poisoning with single-atom alloy catalysts. *Journal of the American Chemical Society* **2016,** *138* (20), 6396-6399.
41. Gracia, F.; Bollmann, L.; Wolf, E.; Miller, J.; Kropf, A., In situ FTIR, EXAFS, and activity studies of the effect of crystallite size on silica-supported Pt oxidation catalysts. *Journal of Catalysis* **2003,** *220* (2), 382-391.
42. Liu, G.; Robertson, A. W.; Li, M. M.-J.; Kuo, W. C.; Darby, M. T.; Muhieddine, M. H.; Lin, Y.-C.; Suenaga, K.; Stamatakis, M.; Warner, J. H., MoS2 monolayer catalyst doped with isolated Co atoms for the hydrodeoxygenation reaction. *Nature chemistry* **2017,** *9* (8), 810-816.
43. Resasco, J.; DeRita, L.; Dai, S.; Chada, J. P.; Xu, M.; Yan, X.; Finzel, J.; Hanukovich, S.; Hoffman, A. S.; Graham, G. W., Uniformity is key in defining structure–function relationships for atomically dispersed metal catalysts: The case of Pt/CeO2. *Journal of the American Chemical Society* **2019,** *142* (1), 169-184.
44. Kuo, C.-T.; Lu, Y.; Kovarik, L.; Engelhard, M.; Karim, A. M., Structure sensitivity of acetylene semi-hydrogenation on Pt single atoms and subnanometer clusters. *ACS Catalysis* **2019,** *9* (12), 11030-11041.
45. Tauster, S.; Fung, S.; Garten, R. L., Strong metal-support interactions. Group 8 noble metals supported on titanium dioxide. *Journal of the American Chemical Society* **1978,** *100* (1), 170-175.
46. Zhang, S.; Plessow, P. N.; Willis, J. J.; Dai, S.; Xu, M.; Graham, G. W.; Cargnello, M.; Abild-Pedersen, F.; Pan, X., Dynamical observation and detailed description of catalysts under strong metal–support interaction. *Nano Letters* **2016,** *16* (7), 4528-4534.
47. Tauster, S., Strong metal-support interactions. *Accounts of Chemical Research* **1987,** *20* (11), 389-394.
48. Sakellson, S.; McMillan, M.; Haller, G. L., EXAFS evidence for direct metal-metal bonding in reduced rhodium/titania catalysts. *The Journal of Physical Chemistry* **1986,** *90* (9), 1733-1736.
49. Liu, X.; Liu, M.-H.; Luo, Y.-C.; Mou, C.-Y.; Lin, S. D.; Cheng, H.; Chen, J.-M.; Lee, J.-F.; Lin, T.-S., Strong metal–support interactions between gold nanoparticles and ZnO nanorods in CO oxidation. *Journal of the American Chemical Society* **2012,** *134* (24), 10251-10258.
50. Deng, L.; Miura, H.; Shishido, T.; Hosokawa, S.; Teramura, K.; Tanaka, T., Strong metal-support interaction between Pt and SiO 2 following high-temperature

reduction: a catalytic interface for propane dehydrogenation. *Chemical Communications* **2017,** *53* (51), 6937-6940.
51. Tang, H.; Wei, J.; Liu, F.; Qiao, B.; Pan, X.; Li, L.; Liu, J.; Wang, J.; Zhang, T., Strong metal–support interactions between gold nanoparticles and nonoxides. *Journal of the American Chemical Society* **2016,** *138* (1), 56-59.
52. Dong, J.; Fu, Q.; Li, H.; Xiao, J.; Yang, B.; Zhang, B.; Bai, Y.; Song, T.; Zhang, R.; Gao, L., Reaction-induced strong metal–support interactions between metals and inert boron nitride nanosheets. *Journal of the American Chemical Society* **2020,** *142* (40), 17167-17174.
53. Lin, L.; Yao, S.; Gao, R.; Liang, X.; Yu, Q.; Deng, Y.; Liu, J.; Peng, M.; Jiang, Z.; Li, S., A highly CO-tolerant atomically dispersed Pt catalyst for chemoselective hydrogenation. *Nature nanotechnology* **2019,** *14* (4), 354-361.
54. Fu, Q.; Wagner, T., Interaction of nanostructured metal overlayers with oxide surfaces. *Surface science reports* **2007,** *62* (11), 431-498.
55. Gao, Y.; Liang, Y.; Chambers, S. A., Thermal stability and the role of oxygen vacancy defects in strong metal support interaction—Pt on Nb-doped TiO2 (100). *Surface science* **1996,** *365* (3), 638-648.
56. Fu, Q.; Wagner, T.; Olliges, S.; Carstanjen, H.-D., Metal− Oxide interfacial reactions: encapsulation of Pd on TiO2 (110). *The Journal of Physical Chemistry B* **2005,** *109* (2), 944-951.
57. Gonzalez-DelaCruz, V. M.; Holgado, J. P.; Pereñíguez, R.; Caballero, A., Morphology changes induced by strong metal–support interaction on a Ni–ceria catalytic system. *Journal of Catalysis* **2008,** *257* (2), 307-314.
58. Bruix, A.; Rodriguez, J. A.; Ramírez, P. J.; Senanayake, S. D.; Evans, J.; Park, J. B.; Stacchiola, D.; Liu, P.; Hrbek, J.; Illas, F., A new type of strong metal–support interaction and the production of H2 through the transformation of water on Pt/CeO2 (111) and Pt/CeO x/TiO2 (110) catalysts. *Journal of the American Chemical Society* **2012,** *134* (21), 8968-8974.
59. Tung, R. T., Recent advances in Schottky barrier concepts. *Materials Science and Engineering: R: Reports* **2001,** *35* (1-3), 1-138.
60. Lang, R.; Xi, W.; Liu, J.-C.; Cui, Y.-T.; Li, T.; Lee, A. F.; Chen, F.; Chen, Y.; Li, L.; Li, L.; Lin, J.; Miao, S.; Liu, X.; Wang, A.-Q.; Wang, X.; Luo, J.; Qiao, B.; Li, J.; Zhang, T., Non defect-stabilized thermally stable single-atom catalyst. *Nature Communications* **2019,** *10* (1), 234.
61. Dong, J.; Fu, Q.; Jiang, Z.; Mei, B.; Bao, X., Carbide-supported Au catalysts for water–gas shift reactions: a new territory for the strong metal–support interaction effect. *Journal of the American Chemical Society* **2018,** *140* (42), 13808-13816.
62. Kalamaras, C. M.; Panagiotopoulou, P.; Kondarides, D. I.; Efstathiou, A. M., Kinetic and mechanistic studies of the water–gas shift reaction on Pt/TiO2 catalyst. *Journal of Catalysis* **2009,** *264* (2), 117-129.
63. Zhang, Y.; Zhang, Z.; Yang, X.; Wang, R.; Duan, H.; Shen, Z.; Li, L.; Su, Y.; Yang, R.; Zhang, Y., Tuning selectivity of CO 2 hydrogenation by modulating the

strong metal–support interaction over Ir/TiO 2 catalysts. *Green Chemistry* **2020,** *22* (20), 6855-6861.
64. Xu, M.; He, S.; Chen, H.; Cui, G.; Zheng, L.; Wang, B.; Wei, M., TiO2–x-modified Ni nanocatalyst with tunable metal–support interaction for water–gas shift reaction. *ACS Catalysis* **2017,** *7* (11), 7600-7609.
65. Jing, K.-Q.; Fu, Y.-Q.; Chen, Z.-N.; Zhang, T.; Sun, J.; Xu, Z.-N.; Guo, G.-C., Boosting Interfacial Electron Transfer between Pd and ZnTi-LDH via Defect Induction for Enhanced Metal–Support Interaction in CO Direct Esterification Reaction. *ACS Applied Materials & Interfaces* **2021,** *13* (21), 24856-24864.
66. Tan, H.; Xu, Y.-P.; Rong, S.; Zhao, R.; Cui, H.; Chen, Z.-N.; Xu, Z.-N.; Zhang, N.-N.; Guo, G.-C., Enhanced metal–support interaction between Pd and hierarchical Nb 2 O 5 via oxygen defect induction to promote CO oxidative coupling to dimethyl oxalate. *Nanoscale* **2021,** *13* (44), 18773-18779.
67. Horsley, J., A molecular orbital study of strong metal-support interaction between platinum and titanium dioxide. *Journal of the American Chemical Society* **1979,** *101* (11), 2870-2874.
68. Han, Y.; Liu, C.-j.; Ge, Q., Effect of surface oxygen vacancy on pt cluster adsorption and growth on the defective anatase TiO2 (101) surface. *The Journal of Physical Chemistry C* **2007,** *111* (44), 16397-16404.
69. Dong, S.; Zhang, Y.; Zhang, X.; Mao, J.; Yang, Z., High Stability and Reactivity of Single-Metal Atom Catalysts Supported on Yttria-Stabilized Zirconia: The Role of the Surface Oxygen Vacancy. *The Journal of Physical Chemistry C* **2018,** *122* (3), 1622-1630.
70. Li, S.; Xu, Y.; Chen, Y.; Li, W.; Lin, L.; Li, M.; Deng, Y.; Wang, X.; Ge, B.; Yang, C., Tuning the selectivity of catalytic carbon dioxide hydrogenation over iridium/cerium oxide catalysts with a strong metal–support interaction. *Angewandte Chemie* **2017,** *129* (36), 10901-10905.
71. Wan, J.; Chen, W.; Jia, C.; Zheng, L.; Dong, J.; Zheng, X.; Wang, Y.; Yan, W.; Chen, C.; Peng, Q., Defect effects on TiO2 nanosheets: stabilizing single atomic site Au and promoting catalytic properties. *Advanced Materials* **2018,** *30* (11), 1705369.
72. Hernández Mejía, C.; van Deelen, T. W.; de Jong, K. P., Activity enhancement of cobalt catalysts by tuning metal-support interactions. *Nature communications* **2018,** *9* (1), 1-8.
73. Ning, X.; Li, Y.; Dong, B.; Wang, H.; Yu, H.; Peng, F.; Yang, Y., Electron transfer dependent catalysis of Pt on N-doped carbon nanotubes: Effects of synthesis method on metal-support interaction. *Journal of Catalysis* **2017,** *348*, 100-109.
74. Rui, Z.; Chen, L.; Chen, H.; Ji, H., Strong metal-support interaction in Pt/TiO2 induced by mild HCHO and NaBH4 solution reduction and its effect on catalytic toluene combustion. *Industrial & Engineering Chemistry Research* **2014,** *53* (41), 15879-15888.

75. Moon, S. Y.; Naik, B.; Jung, C.-H.; Qadir, K.; Park, J. Y., Tailoring metal–oxide interfaces of oxide-encapsulated Pt/silica hybrid nanocatalysts with enhanced thermal stability. *Catalysis Today* **2016,** *265*, 245-253.
76. Ro, I.; Liu, Y.; Ball, M. R.; Jackson, D. H.; Chada, J. P.; Sener, C.; Kuech, T. F.; Madon, R. J.; Huber, G. W.; Dumesic, J. A., Role of the Cu-ZrO2 interfacial sites for conversion of ethanol to ethyl acetate and synthesis of methanol from CO2 and H2. *ACS Catalysis* **2016,** *6* (10), 7040-7050.
77. Matsubu, J. C.; Zhang, S.; DeRita, L.; Marinkovic, N. S.; Chen, J. G.; Graham, G. W.; Pan, X.; Christopher, P., Adsorbate-mediated strong metal–support interactions in oxide-supported Rh catalysts. *Nature chemistry* **2017,** *9* (2), 120-127.
78. Zhang, J.; Wang, H.; Wang, L.; Ali, S.; Wang, C.; Wang, L.; Meng, X.; Li, B.; Su, D. S.; Xiao, F.-S., Wet-chemistry strong metal–support interactions in titania-supported Au catalysts. *Journal of the American Chemical Society* **2019,** *141* (7), 2975-2983.
79. Mehrabadi, B. A.; Eskandari, S.; Khan, U.; White, R. D.; Regalbuto, J. R., A review of preparation methods for supported metal catalysts. *Advances in catalysis* **2017,** *61*, 1-35.
80. Schweitzer, N.; Xin, H.; Nikolla, E.; Miller, J. T.; Linic, S., Establishing relationships between the geometric structure and chemical reactivity of alloy catalysts based on their measured electronic structure. *Topics in Catalysis* **2010,** *53* (5), 348-356.
81. Xu, F.; Le, Y.; Cheng, B.; Jiang, C., Effect of calcination temperature on formaldehyde oxidation performance of Pt/TiO2 nanofiber composite at room temperature. *Applied Surface Science* **2017,** *426*, 333-341.
82. Epling, W. S.; Cheekatamarla, P. K.; Lane, A. M., Reaction and surface characterization studies of titania-supported Co, Pt and Co/Pt catalysts for the selective oxidation of CO in H2-containing streams. *Chemical Engineering Journal* **2003,** *93* (1), 61-68.
83. Panagiotopoulou, P.; Christodoulakis, A.; Kondarides, D.; Boghosian, S., Particle size effects on the reducibility of titanium dioxide and its relation to the water–gas shift activity of Pt/TiO2 catalysts. *Journal of Catalysis* **2006,** *240* (2), 114-125.
84. Vannice, M. A.; Twu, C.; Moon, S., SMSI effects on CO adsorption and hydrogenation on Pt catalysts: I. Infrared spectra of adsorbed CO prior to and during reaction conditions. *Journal of Catalysis* **1983,** *79* (1), 70-80.
85. Alexeev, O. S.; Chin, S. Y.; Engelhard, M. H.; Ortiz-Soto, L.; Amiridis, M. D., Effects of reduction temperature and metal− support interactions on the catalytic activity of Pt/γ-Al2O3 and Pt/TiO2 for the oxidation of CO in the presence and absence of H2. *The Journal of Physical Chemistry B* **2005,** *109* (49), 23430-23443.
86. Han, B.; Guo, Y.; Huang, Y.; Xi, W.; Xu, J.; Luo, J.; Qi, H.; Ren, Y.; Liu, X.; Qiao, B., Strong metal–support interactions between Pt single atoms and TiO2. *Angewandte Chemie* **2020,** *132* (29), 11922-11927.
87. Zhang, L.; Zhou, M.; Wang, A.; Zhang, T., Selective hydrogenation over supported metal catalysts: from nanoparticles to single atoms. *Chemical reviews* **2019,** *120* (2), 683-733.

88. Mougenot, M.; Caillard, A.; Brault, P.; Baranton, S.; Coutanceau, C., High Performance plasma sputtered PdPt fuel cell electrodes with ultra low loading. *International Journal of Hydrogen Energy* **2011,** *36* (14), 8429-8434.
89. King, J. S.; Wittstock, A.; Biener, J.; Kucheyev, S. O.; Wang, Y. M.; Baumann, T. F.; Giri, S. K.; Hamza, A. V.; Baeumer, M.; Bent, S. F., Ultralow loading Pt nanocatalysts prepared by atomic layer deposition on carbon aerogels. *Nano letters* **2008,** *8* (8), 2405-2409.
90. Ayers, K. E.; Renner, J. N.; Danilovic, N.; Wang, J. X.; Zhang, Y.; Maric, R.; Yu, H., Pathways to ultra-low platinum group metal catalyst loading in proton exchange membrane electrolyzers. *Catalysis Today* **2016,** *262*, 121-132.
91. Chen, F.; Jiang, X.; Zhang, L.; Lang, R.; Qiao, B., Single-atom catalysis: Bridging the homo-and heterogeneous catalysis. *Chinese Journal of Catalysis* **2018,** *39* (5), 893-898.
92. Liu, J., Catalysis by supported single metal atoms. *Acs Catalysis* **2017,** *7* (1), 34-59.
93. Liu, L.; Corma, A., Metal catalysts for heterogeneous catalysis: from single atoms to nanoclusters and nanoparticles. *Chemical reviews* **2018,** *118* (10), 4981-5079.
94. Thomas, J. M.; Raja, R.; Gai, P. L.; Grönbeck, H.; Hernández‐Garrido, J. C., Exceptionally Active Single‐Site Nanocluster Multifunctional Catalysts for Cascade Reactions. *ChemCatChem* **2010,** *2* (4), 402-406.
95. Vajda, S.; Pellin, M. J.; Greeley, J. P.; Marshall, C. L.; Curtiss, L. A.; Ballentine, G. A.; Elam, J. W.; Catillon-Mucherie, S.; Redfern, P. C.; Mehmood, F., Subnanometre platinum clusters as highly active and selective catalysts for the oxidative dehydrogenation of propane. *Nature materials* **2009,** *8* (3), 213-216.
96. Liu, J.; Jiao, M.; Mei, B.; Tong, Y.; Li, Y.; Ruan, M.; Song, P.; Sun, G.; Jiang, L.; Wang, Y., Carbon‐supported divacancy‐anchored platinum single‐atom electrocatalysts with superhigh Pt utilization for the oxygen reduction reaction. *Angewandte Chemie* **2019,** *131* (4), 1175-1179.
97. He, X.; He, Q.; Deng, Y.; Peng, M.; Chen, H.; Zhang, Y.; Yao, S.; Zhang, M.; Xiao, D.; Ma, D., A versatile route to fabricate single atom catalysts with high chemoselectivity and regioselectivity in hydrogenation. *Nature communications* **2019,** *10* (1), 1-9.
98. Schwartz, V.; Mullins, D. R.; Yan, W.; Chen, B.; Dai, S.; Overbury, S. H., XAS study of Au supported on TiO2: Influence of oxidation state and particle size on catalytic activity. *The Journal of Physical Chemistry B* **2004,** *108* (40), 15782-15790.
99. Hilbrig, F.; Michel, C.; Haller, G. L., A XANES-TPR study of platinum-rhenium/alumina catalysts. *The Journal of Physical Chemistry* **1992,** *96* (24), 9893-9899.
100. Zhang, Z.; Zhu, Y.; Asakura, H.; Zhang, B.; Zhang, J.; Zhou, M.; Han, Y.; Tanaka, T.; Wang, A.; Zhang, T., Thermally stable single atom Pt/m-Al 2 O 3 for selective hydrogenation and CO oxidation. *Nature communications* **2017,** *8* (1), 1-10.

101. Ding, K.; Gulec, A.; Johnson, A. M.; Schweitzer, N. M.; Stucky, G. D.; Marks, L. D.; Stair, P. C., Identification of active sites in CO oxidation and water-gas shift over supported Pt catalysts. *Science* **2015,** *350* (6257), 189-192.
102. Matsubu, J. C.; Yang, V. N.; Christopher, P., Isolated metal active site concentration and stability control catalytic CO2 reduction selectivity. *Journal of the American Chemical Society* **2015,** *137* (8), 3076-3084.
103. Resasco, J.; Yang, F.; Mou, T.; Wang, B.; Christopher, P.; Resasco, D. E., Relationship between atomic scale structure and reactivity of Pt catalysts: hydrodeoxygenation of m-cresol over isolated Pt cations and clusters. *ACS Catalysis* **2019,** *10* (1), 595-603.
104. Lu, Y.; Kuo, C.-T.; Kovarik, L.; Hoffman, A. S.; Boubnov, A.; Driscoll, D. M.; Morris, J. R.; Bare, S. R.; Karim, A. M., A versatile approach for quantification of surface site fractions using reaction kinetics: The case of CO oxidation on supported Ir single atoms and nanoparticles. *Journal of Catalysis* **2019,** *378*, 121-130.
105. Moses-DeBusk, M.; Yoon, M.; Allard, L. F.; Mullins, D. R.; Wu, Z.; Yang, X.; Veith, G.; Stocks, G. M.; Narula, C. K., CO oxidation on supported single Pt atoms: experimental and ab initio density functional studies of CO interaction with Pt atom on θ-Al2O3 (010) surface. *Journal of the American Chemical Society* **2013,** *135* (34), 12634-12645.
106. Kunwar, D.; Zhou, S.; DeLaRiva, A.; Peterson, E. J.; Xiong, H.; Pereira-Hernández, X. I.; Purdy, S. C.; ter Veen, R.; Brongersma, H. H.; Miller, J. T., Stabilizing high metal loadings of thermally stable platinum single atoms on an industrial catalyst support. *ACS Catalysis* **2019,** *9* (5), 3978-3990.
107. Pei, G. X.; Liu, X. Y.; Wang, A.; Lee, A. F.; Isaacs, M. A.; Li, L.; Pan, X.; Yang, X.; Wang, X.; Tai, Z., Ag alloyed Pd single-atom catalysts for efficient selective hydrogenation of acetylene to ethylene in excess ethylene. *Acs Catalysis* **2015,** *5* (6), 3717-3725.
108. Huang, X.; Xia, Y.; Cao, Y.; Zheng, X.; Pan, H.; Zhu, J.; Ma, C.; Wang, H.; Li, J.; You, R., Enhancing both selectivity and coking-resistance of a single-atom Pd 1/C 3 N 4 catalyst for acetylene hydrogenation. *Nano Research* **2017,** *10* (4), 1302-1312.
109. Crampton, A. S.; Rötzer, M. D.; Ridge, C. J.; Schweinberger, F. F.; Heiz, U.; Yoon, B.; Landman, U., Structure sensitivity in the nonscalable regime explored via catalysed ethylene hydrogenation on supported platinum nanoclusters. *Nature communications* **2016,** *7* (1), 1-12.
110. Kuai, L.; Chen, Z.; Liu, S.; Kan, E.; Yu, N.; Ren, Y.; Fang, C.; Li, X.; Li, Y.; Geng, B., Titania supported synergistic palladium single atoms and nanoparticles for room temperature ketone and aldehydes hydrogenation. *Nature communications* **2020,** *11* (1), 1-9.
111. Fu, J.; Lym, J.; Zheng, W.; Alexopoulos, K.; Mironenko, A. V.; Li, N.; Boscoboinik, J. A.; Su, D.; Weber, R. T.; Vlachos, D. G., C–O bond activation using ultralow loading of noble metal catalysts on moderately reducible oxides. *Nature Catalysis* **2020,** *3* (5), 446-453.

112. Liu, L.; Meira, D. M.; Arenal, R.; Concepcion, P.; Puga, A. V.; Corma, A., Determination of the evolution of heterogeneous single metal atoms and nanoclusters under reaction conditions: which are the working catalytic sites? *ACS catalysis* **2019,** *9* (12), 10626-10639.
113. Han, Y.; Liu, C.-j.; Ge, Q., Interaction of Pt clusters with the anatase TiO2 (101) surface: A first principles study. *The Journal of Physical Chemistry B* **2006,** *110* (14), 7463-7472.
114. Zhou, Y.; Muhich, C. L.; Neltner, B. T.; Weimer, A. W.; Musgrave, C. B., Growth of Pt particles on the anatase TiO2 (101) surface. *The Journal of Physical Chemistry C* **2012,** *116* (22), 12114-12123.
115. Teo, B. K.; Sloane, N., Magic numbers in polygonal and polyhedral clusters. *Inorganic Chemistry* **1985,** *24* (26), 4545-4558.
116. Stadnichenko, A.; Svintsitskiy, D.; Kibis, L.; Fedorova, E.; Stonkus, O.; Slavinskaya, E.; Lapin, I.; Fakhrutdinova, E.; Svetlichnyi, V.; Romanenko, A., Influence of titania synthesized by pulsed laser ablation on the state of platinum during ammonia oxidation. *Applied Sciences* **2020,** *10* (14), 4699.
117. Ignatov, S. K.; Razuvaev, A. G.; Loginova, A. S.; Masunov, A. m. E., Global structure optimization of Pt clusters based on the modified empirical potentials, calibrated using density functional theory. *The Journal of Physical Chemistry C* **2019,** *123* (47), 29024-29036.
118. Yoshida, H.; Nonoyama, S.; Yazawa, Y.; Hattori, T., Quantitative determination of platinum oxidation state by XANES analysis. *Physica Scripta* **2005,** *2005* (T115), 813.
119. Zhang, C.; He, H.; Tanaka, K.-i., Catalytic performance and mechanism of a Pt/TiO2 catalyst for the oxidation of formaldehyde at room temperature. *Applied Catalysis B: Environmental* **2006,** *65* (1-2), 37-43.
120. Czupryn, K.; Kocemba, I.; Rynkowski, J., Photocatalytic CO oxidation with water over Pt/TiO 2 catalysts. *Reaction Kinetics, Mechanisms and Catalysis* **2018,** *124* (1), 187-201.
121. de Resende, N. S.; Eon, J.-G.; Schmal, M., Pt–TiO2–γ Al2O3Catalyst: I. Dispersion of Platinum on Alumina-Grafted Titanium Oxide. *Journal of Catalysis* **1999,** *183* (1), 6-13.
122. Pisduangdaw, S.; Mekasuwandumrong, O.; Yoshida, H.; Fujita, S.-I.; Arai, M.; Panpranot, J., Flame-made Pt/TiO2 catalysts for the liquid-phase selective hydrogenation of 3-nitrostyrene. *Applied Catalysis A: General* **2015,** *490*, 193-200.
123. Imaoka, T.; Akanuma, Y.; Haruta, N.; Tsuchiya, S.; Ishihara, K.; Okayasu, T.; Chun, W.-J.; Takahashi, M.; Yamamoto, K., Platinum clusters with precise numbers of atoms for preparative-scale catalysis. *Nature communications* **2017,** *8* (1), 1-8.
124. Li, J.; Zhang, B.; Chen, Y.; Zhang, J.; Yang, H.; Zhang, J.; Lu, X.; Li, G.; Qin, Y., Styrene hydrogenation performance of Pt nanoparticles with controlled size prepared by atomic layer deposition. *Catalysis Science & Technology* **2015,** *5* (8), 4218-4223.

125. Wu, Z.; Li, Y.; Huang, W., Size-Dependent Pt-TiO2 Strong Metal–Support Interaction. *The Journal of Physical Chemistry Letters* **2020,** *11* (12), 4603-4607.
126. Bond, G. C., Supported metal catalysts: some unsolved problems. *Chemical Society Reviews* **1991,** *20* (4), 441-475.
127. Zaera, F., Key unanswered questions about the mechanism of olefin hydrogenation catalysis by transition-metal surfaces: a surface-science perspective. *Physical Chemistry Chemical Physics* **2013,** *15* (29), 11988-12003.
128. Zaera, F., The surface chemistry of metal-based hydrogenation catalysis. *ACS Catalysis* **2017,** *7* (8), 4947-4967.
129. Wang, S. Y.; Moon, S.; Vannice, M. A., The effect of SMSI (strong metal-support interaction) behavior on CO adsorption and hydrogenation on Pd catalysts: II. Kinetic behavior in the methanation reaction. *Journal of Catalysis* **1981,** *71* (1), 167-174.
130. Li, H.; Li, L.; Li, Y., The electronic structure and geometric structure of nanoclusters as catalytic active sites. *Nanotechnology Reviews* **2013,** *2* (5), 515-528.
131. Sápi, A.; Rajkumar, T.; Kiss, J.; Kukovecz, Á.; Kónya, Z.; Somorjai, G. A., Metallic Nanoparticles in Heterogeneous Catalysis. *Catalysis Letters* **2021,** *151* (8), 2153-2175.
132. Wang, H.; Gu, X.-K.; Zheng, X.; Pan, H.; Zhu, J.; Chen, S.; Cao, L.; Li, W.-X.; Lu, J., Disentangling the size-dependent geometric and electronic effects of palladium nanocatalysts beyond selectivity. *Science advances* **2019,** *5* (1), eaat6413.
133. Stamatiou, I.; Brennan, C.; Muller, F. L., Determination of styrene hydrogenation surface kinetics through detailed simulation of the hydrogen uptake curve. *Reaction Chemistry & Engineering* **2019,** *4* (8), 1477-1485.
134. Zhang, S.; Xia, Z.; Zhang, M.; Zou, Y.; Shen, H.; Li, J.; Chen, X.; Qu, Y., Boosting selective hydrogenation through hydrogen spillover on supported-metal catalysts at room temperature. *Applied Catalysis B: Environmental* **2021**, 120418.
135. Zieliński, J.; Zglinicka, I.; Znak, L.; Kaszkur, Z., Reduction of Fe2O3 with hydrogen. *Applied Catalysis A: General* **2010,** *381* (1-2), 191-196.
136. Shen, Q.; Jin, H.; Li, P.; Yu, X.; Zheng, L.; Song, W.; Cao, C., Breaking the activity limitation of iridium single-atom catalyst in hydrogenation of quinoline with synergistic nanoparticles catalysis. *Nano Research* **2022**, 1-8.
137. Zhang, B.; Asakura, H.; Zhang, J.; Zhang, J.; De, S.; Yan, N., Stabilizing a platinum1 single‐atom catalyst on supported phosphomolybdic acid without compromising hydrogenation activity. *Angewandte Chemie* **2016,** *128* (29), 8459-8463.
138. Chen, J.; Zhang, W.; Li, H.; Li, W.; Zhao, D., Recent advances in TiO2‐based catalysts for N2 reduction reaction. *SusMat* **2021,** *1* (2), 174-193.
139. Menard, L. D.; Xu, F.; Nuzzo, R. G.; Yang, J. C., Preparation of TiO2-supported Au nanoparticle catalysts from a Au13 cluster precursor: Ligand removal using ozone exposure versus a rapid thermal treatment. *Journal of Catalysis* **2006,** *243* (1), 64-73.

140. Chiarello, G. L.; Dozzi, M. V.; Selli, E., TiO2-based materials for photocatalytic hydrogen production. *Journal of energy Chemistry* **2017,** *26* (2), 250-258.
141. Park, H.; Park, Y.; Kim, W.; Choi, W., Surface modification of TiO2 photocatalyst for environmental applications. *Journal of Photochemistry and Photobiology C: Photochemistry Reviews* **2013,** *15*, 1-20.
142. Kamat, P. V., Photophysical, photochemical and photocatalytic aspects of metal nanoparticles. ACS Publications: 2002; Vol. 106, pp 7729-7744.
143. Chen, X.; Liu, L.; Peter, Y. Y.; Mao, S. S., Increasing solar absorption for photocatalysis with black hydrogenated titanium dioxide nanocrystals. *Science* **2011,** *331* (6018), 746-750.
144. Nowotny, M.; Bak, T.; Nowotny, J., Electrical properties and defect chemistry of TiO2 single crystal. I. Electrical conductivity. *The Journal of Physical Chemistry B* **2006,** *110* (33), 16270-16282.
145. Nong, S.; Dong, W.; Yin, J.; Dong, B.; Lu, Y.; Yuan, X.; Wang, X.; Bu, K.; Chen, M.; Jiang, S., Well-dispersed ruthenium in mesoporous crystal TiO2 as an advanced electrocatalyst for hydrogen evolution reaction. *Journal of the American Chemical Society* **2018,** *140* (17), 5719-5727.
146. Zuo, F.; Wang, L.; Wu, T.; Zhang, Z.; Borchardt, D.; Feng, P., Self-doped Ti3+ enhanced photocatalyst for hydrogen production under visible light. *Journal of the American Chemical Society* **2010,** *132* (34), 11856-11857.
147. Yang, G.; Wang, L.; Peng, S.; Wang, J.; Ji, D.; Yan, W.; Ramakrishna, S., In situ fabrication of hierarchically branched TiO2 nanostructures: enhanced performance in photocatalytic h2 evolution and li–ion batteries. *Small* **2017,** *13* (47), 1702357.
148. Zhang, Y.; Liu, J. X.; Qian, K.; Jia, A.; Li, D.; Shi, L.; Hu, J.; Zhu, J.; Huang, W., Structure Sensitivity of Au‐TiO2 Strong Metal‐Support Interactions. *Angewandte Chemie International Edition* **2021,** *60* (21), 12074-12081.
149. Bertella, F.; Concepción, P.; Martínez, A., TiO2 polymorph dependent SMSI effect in Co-Ru/TiO2 catalysts and its relevance to Fischer-Tropsch synthesis. *Catalysis Today* **2017,** *289*, 181-191.
150. Zhang, D.; Gokce, B.; Barcikowski, S., Laser synthesis and processing of colloids: fundamentals and applications. *Chemical reviews* **2017,** *117* (5), 3990-4103.
151. Yang, H.; Liu, W.; Xu, C.; Fan, D.; Cao, Y.; Xue, W., Laser sintering of TiO2 films for flexible dye-sensitized solar cells. *Applied Sciences* **2019,** *9* (5), 823.
152. Zuñiga-Ibarra, V.; Shaji, S.; Krishnan, B.; Johny, J.; Kanakkillam, S. S.; Avellaneda, D.; Martinez, J. A.; Roy, T. D.; Ramos-Delgado, N., Synthesis and characterization of black TiO2 nanoparticles by pulsed laser irradiation in liquid. *Applied Surface Science* **2019,** *483*, 156-164.
153. Fathi-Hafshejani, P.; Johnson, H.; Ahmadi, Z.; Roach, M.; Shamsaei, N.; Mahjouri-Samani, M., Phase-selective and localized TiO2 coating on additive and wrought titanium by a direct laser surface modification approach. *ACS omega* **2020,** *5* (27), 16744-16751.

154. Lau, M.; Reichenberger, S.; Haxhiaj, I.; Barcikowski, S.; Müller, A. M., Mechanism of laser-induced bulk and surface defect generation in ZnO and TiO2 nanoparticles: effect on photoelectrochemical performance. *ACS Applied Energy Materials* **2018,** *1* (10), 5366-5385.
155. Patil, P.; Phase, D.; Kulkarni, S.; Ghaisas, S.; Kulkarni, S.; Kanetkar, S.; Ogale, S.; Bhide, V., Pulsed-laser–induced reactive quenching at liquid-solid interface: Aqueous oxidation of iron. *Physical review letters* **1987,** *58* (3), 238.
156. Fojtik, A.; Henglein, A., Laser ablation of films and suspended particles in a solvent: formation of cluster and colloid solutions. *BERICHTE-BUNSENGESELLSCHAFT FUR PHYSIKALISCHE CHEMIE* **1993,** *97*, 252-252.
157. Henglein, A., Physicochemical properties of small metal particles in solution:" microelectrode" reactions, chemisorption, composite metal particles, and the atom-to-metal transition. *The Journal of Physical Chemistry* **1993,** *97* (21), 5457-5471.
158. Kawasaki, K.; Despres, J.; Kamei, S.; Ishikawa, M.; Odawara, O., Fabrication of nanometer-sized anatase particles by a pulsed laser ablation method. *Journal of Materials Chemistry* **1997,** *7* (10), 2117-2120.
159. Lv, J.; Tian, Z.; Dai, K.; Ye, Y.; Liang, C., Interface and defect engineer of titanium dioxide supported palladium or platinum for tuning the activity and selectivity of electrocatalytic nitrogen reduction reaction. *Journal of colloid and interface science* **2019,** *553*, 126-135.
160. Gondal, M.; Ilyas, A.; Baig, U., Pulsed laser ablation in liquid synthesis of ZnO/TiO2 nanocomposite catalyst with enhanced photovoltaic and photocatalytic performance. *Ceramics International* **2016,** *42* (11), 13151-13160.
161. Balati, A.; Tek, S.; Nash, K.; Shipley, H., Nanoarchitecture of TiO2 microspheres with expanded lattice interlayers and its heterojunction to the laser modified black TiO2 using pulsed laser ablation in liquid with improved photocatalytic performance under visible light irradiation. *Journal of colloid and interface science* **2019,** *541*, 234-248.
162. Sasaki, T.; Koshizaki, N.; Yoon, J.-W.; Beck, K. M., Preparation of Pt/TiO2 nanocomposite thin films by pulsed laser deposition and their photoelectrochemical behaviors. *Journal of Photochemistry and Photobiology A: Chemistry* **2001,** *145* (1-2), 11-16.
163. Ruppert, A.; Paryjczak, T., Pt/ZrO2/TiO2 catalysts for selective hydrogenation of crotonaldehyde: Tuning the SMSI effect for optimum performance. *Applied Catalysis A: General* **2007,** *320*, 80-90.
164. Kresse, G.; Furthmüller, J., Efficiency of ab-initio total energy calculations for metals and semiconductors using a plane-wave basis set. *Computational materials science* **1996,** *6* (1), 15-50.
165. Kresse, G.; Furthmüller, J., Efficient iterative schemes for ab initio total-energy calculations using a plane-wave basis set. *Physical review B* **1996,** *54* (16), 11169.
166. Hohenberg, P.; Kohn, W., Inhomogeneous Electron Gas. *Physical Review* **1964,** *136* (3B), B864-B871.

167. Blöchl, P. E., Projector augmented-wave method. *Physical Review B* **1994,** *50* (24), 17953-17979.
168. Muhich, C. L.; Zhou, Y.; Holder, A. M.; Weimer, A. W.; Musgrave, C. B., Effect of Surface Deposited Pt on the Photoactivity of TiO2. *The Journal of Physical Chemistry C* **2012,** *116* (18), 10138-10149.
169. Anisimov, V. I.; Zaanen, J.; Andersen, O. K., Band theory and Mott insulators: Hubbard U instead of Stoner I. *Physical Review B* **1991,** *44* (3), 943-954.
170. Yang, C.-T.; Balakrishnan, N.; Bhethanabotla, V. R.; Joseph, B., Interplay between Subnanometer Ag and Pt Clusters and Anatase TiO2 (101) Surface: Implications for Catalysis and Photocatalysis. *The Journal of Physical Chemistry C* **2014,** *118* (9), 4702-4714.
171. Song, L.; Ma, J.; Zhang, Q.; Shen, Z., Laser melted oxide ceramics: Multiscale structural evolution with non-equilibrium features. *Journal of Materiomics* **2019,** *5* (3), 436-445.
172. Xia, T.; Chen, X., Revealing the structural properties of hydrogenated black TiO 2 nanocrystals. *Journal of Materials Chemistry A* **2013,** *1* (9), 2983-2989.
173. Ren, R.; Wen, Z.; Cui, S.; Hou, Y.; Guo, X.; Chen, J., Controllable synthesis and tunable photocatalytic properties of Ti 3+-doped TiO 2. *Scientific reports* **2015,** *5* (1), 1-11.
174. Naldoni, A.; Allieta, M.; Santangelo, S.; Marelli, M.; Fabbri, F.; Cappelli, S.; Bianchi, C. L.; Psaro, R.; Dal Santo, V., Effect of nature and location of defects on bandgap narrowing in black TiO2 nanoparticles. *Journal of the American Chemical Society* **2012,** *134* (18), 7600-7603.
175. Mao, X.; Lang, X.; Wang, Z.; Hao, Q.; Wen, B.; Ren, Z.; Dai, D.; Zhou, C.; Liu, L.-M.; Yang, X., Band-gap states of TiO2 (110): major contribution from surface defects. *The Journal of Physical Chemistry Letters* **2013,** *4* (22), 3839-3844.
176. Reyes-Coronado, D.; Rodríguez-Gattorno, G.; Espinosa-Pesqueira, M.; Cab, C.; De Coss, R.; Oskam, G., Phase-pure TiO2 nanoparticles: anatase, brookite and rutile. *Nanotechnology* **2008,** *19* (14), 145605.
177. Zhang, W.; He, Y.; Zhang, M.; Yin, Z.; Chen, Q., Raman scattering study on anatase TiO2 nanocrystals. *Journal of Physics D: Applied Physics* **2000,** *33* (8), 912.
178. Challagulla, S.; Tarafder, K.; Ganesan, R.; Roy, S., Structure sensitive photocatalytic reduction of nitroarenes over TiO 2. *Scientific reports* **2017,** *7* (1), 1-11.
179. Sekiya, T.; Takeda, H.; Kamiya, N.; Kurita, S.; Kodaira, T., EPR of anatase titanium dioxide under uv light irradiation. *physica status solidi c* **2006,** *3* (10), 3603-3606.
180. Kumar, C. P.; Gopal, N. O.; Wang, T. C.; Wong, M.-S.; Ke, S. C., EPR investigation of TiO2 nanoparticles with temperature-dependent properties. *The Journal of Physical Chemistry B* **2006,** *110* (11), 5223-5229.
181. Strunk, J.; Vining, W. C.; Bell, A. T., A study of oxygen vacancy formation and annihilation in submonolayer coverages of TiO2 dispersed on MCM-48. *The Journal of Physical Chemistry C* **2010,** *114* (40), 16937-16945.

182. Komaguchi, K.; Nakano, H.; Araki, A.; Harima, Y., Photoinduced electron transfer from anatase to rutile in partially reduced TiO2 (P-25) nanoparticles: An ESR study. *Chemical physics letters* **2006,** *428* (4-6), 338-342.
183. Liu, H.; Ma, H.; Li, X.; Li, W.; Wu, M.; Bao, X., The enhancement of TiO2 photocatalytic activity by hydrogen thermal treatment. *Chemosphere* **2003,** *50* (1), 39-46.
184. Yu, X.; Kim, B.; Kim, Y. K., Highly enhanced photoactivity of anatase TiO2 nanocrystals by controlled hydrogenation-induced surface defects. *ACS Catalysis* **2013,** *3* (11), 2479-2486.
185. Xin, X.; Xu, T.; Yin, J.; Wang, L.; Wang, C., Management on the location and concentration of Ti3+ in anatase TiO2 for defects-induced visible-light photocatalysis. *Applied Catalysis B: Environmental* **2015,** *176*, 354-362.
186. Bouzoubaa, A.; Markovits, A.; Calatayud, M.; Minot, C., Comparison of the reduction of metal oxide surfaces: TiO2-anatase, TiO2-rutile and SnO2-rutile. *Surface Science* **2005,** *583* (1), 107-117.
187. Ivoning, J.; Van Santen, R., Electrostatic potential calculations on crystalline TiO2: The surface reducibility of rutile and anatase. *Chemical physics letters* **1983,** *101* (6), 541-547.
188. Hanaor, D. A.; Sorrell, C. C., Review of the anatase to rutile phase transformation. *Journal of Materials science* **2011,** *46* (4), 855-874.
189. Hu, X.; Song, J.; Luo, J.; Zhang, H.; Sun, Z.; Li, C.; Zheng, S.; Liu, Q., Single-atomic Pt sites anchored on defective TiO2 nanosheets as a superior photocatalyst for hydrogen evolution. *Journal of Energy Chemistry* **2021,** *62*, 1-10.
190. Kim, S. S.; Lee, H. H.; Hong, S. C., The effect of the morphological characteristics of TiO2 supports on the reverse water–gas shift reaction over Pt/TiO2 catalysts. *Applied Catalysis B: Environmental* **2012,** *119*, 100-108.
191. Jabłońska, M., TPR study and catalytic performance of noble metals modified Al2O3, TiO2 and ZrO2 for low-temperature NH3-SCO. *Catalysis Communications* **2015,** *70*, 66-71.
192. Carvalho, L. S.; Pieck, C.; Rangel, M.; Fıgoli, N.; Grau, J.; Reyes, P.; Parera, J. M., Trimetallic naphtha reforming catalysts. I. Properties of the metal function and influence of the order of addition of the metal precursors on Pt–Re–Sn/γ-Al2O3–Cl. *Applied Catalysis A: General* **2004,** *269* (1-2), 91-103.
193. Wei, H.; Liu, X.; Wang, A.; Zhang, L.; Qiao, B.; Yang, X.; Huang, Y.; Miao, S.; Liu, J.; Zhang, T., FeO x-supported platinum single-atom and pseudo-single-atom catalysts for chemoselective hydrogenation of functionalized nitroarenes. *Nature communications* **2014,** *5* (1), 1-8.
194. Corma, A.; Serna, P., Chemoselective hydrogenation of nitro compounds with supported gold catalysts. *Science* **2006,** *313* (5785), 332-334.
195. Ito, M.; Ikariya, T., Catalytic hydrogenation of polar organic functionalities based on Ru-mediated heterolytic dihydrogen cleavage. *Chemical communications* **2007,** (48), 5134-5142.

196. Comas-Vives, A.; Ujaque, G.; Lledós, A., Inner-and outer-sphere hydrogenation mechanisms: A computational perspective. In *Advances in Inorganic Chemistry*, Elsevier: 2010; Vol. 62, pp 231-260.
197. Ma, D.; Zhai, S.; Wang, Y.; Liu, A.; Chen, C., TiO2 photocatalysis for transfer hydrogenation. *Molecules* **2019,** *24* (2), 330.
198. Corma, A.; Serna, P.; Concepción, P.; Calvino, J. J., Transforming nonselective into chemoselective metal catalysts for the hydrogenation of substituted nitroaromatics. *Journal of the American chemical society* **2008,** *130* (27), 8748-8753.
199. Mironenko, A. V.; Vlachos, D. G., Conjugation-driven "reverse Mars–van Krevelen"-type radical mechanism for low-temperature C–O bond activation. *Journal of the American Chemical Society* **2016,** *138* (26), 8104-8113.
200. Tauster, S.; Fung, S., Strong metal-support interactions: occurrence among the binary oxides of groups IIA–VB. *Journal of Catalysis* **1978,** *55* (1), 29-35.
201. Reed, T. B.; Klerer, J., Free Energy of Formation of Binaray Compounds: An Atlas of Charts for High ‐ Temperature Chemical Calculations. *Journal of The Electrochemical Society* **1972,** *119* (12), 329Ca.
202. Wang, Z.; Wang, C.; Mao, S.; Lu, B.; Chen, Y.; Zhang, X.; Chen, Z.; Wang, Y., Decoupling the electronic and geometric effects of Pt catalysts in selective hydrogenation reaction. *Nature communications* **2022,** *13* (1), 1-10.
203. Priarone, P. C.; Lunetto, V.; Atzeni, E.; Salmi, A., Laser powder bed fusion (L-PBF) additive manufacturing: On the correlation between design choices and process sustainability. *Procedia Cirp* **2018,** *78*, 85-90.